Low-power Power Management Circuit Design for Small Scale Energy Harvesting Using Piezoelectric Cantilevers

Na Kong

Dissertation submitted to the faculty of the
Virginia Polytechnic Institute and State University
in partial fulfillment of the requirements for the degree of

Doctor of Philosophy
in
Computer Engineering

Dong S. Ha, Chairman
Daniel J. Inman
Fred C. Lee
Patrick R. Schaumont
Joseph G. Tront

May 3, 2011
Blacksburg, VA

Keywords: Energy Harvesting, Piezoelectric Cantilevers, Power Management, DC-DC Converter, Impedance Matching

Low-power Power Management Circuit Design for Small Scale Energy Harvesting Using Piezoelectric Cantilevers

Na Kong

Bradley Department of Electrical and Computer Engineering

(ABSTRACT)

The batteries used to power wireless sensor nodes have become a major roadblock for the wide deployment. Harvesting energy from mechanical vibrations using piezoelectric cantilevers provides possible means to recharge the batteries or eliminate them. Raw power harvested from ambient sources should be conditioned and regulated to a desired voltage level before its application to electronic devices. The efficiency and self-powered operation of a power conditioning and management circuit is a key design issue.

In this research, we investigate the characteristics of piezoelectric cantilevers and requirements of power conditioning and management circuits. A two-stage conditioning circuit with a rectifier and a DC-DC converter is proposed to match the source impedance dynamically. Several low-power design methods are proposed to reduce power consumption of the circuit including: (i) use of a discontinuous conduction mode (DCM) flyback converter, (ii) constant on-time modulation, and (iii) control of the clock frequency of a microcontroller unit (MCU). The DCM flyback converter behaves as a lossless resistor to match the source impedance for maximum power point tracking (MPPT). The constant on-time modulation lowers the clock frequency of the MCU by more than an order of magnitude, which reduces dynamic power dissipation of the MCU.

MPPT is executed by the MCU at intermittent time interval to save power. Experimental results indicate that the proposed system harvests up to 8.4 mW of power under 0.5-g base acceleration using four parallel piezoelectric cantilevers and achieves 72 percent power efficiency. Sources of power losses in the system are analyzed. The diode and the controller (specifically the MCU) are the two major sources for the power loss.

In order to further improve the power efficiency, the power conditioning circuit is implemented in a monolithic IC using 0.18-μm CMOS process. Synchronous rectifiers instead of diodes are used to reduce the conduction loss. A mixed-signal control circuit is adopted to replace the MCU to realize the MPPT function. Simulation and experimental results verify the DCM operation of the power stage and function of the MPPT circuit. The power consumption of the mixed-signal control circuit is reduced to 16 percent of that of the MCU.

Acknowledgements

I would like to express my sincere appreciation to my advisor, Dr. Dong S. Ha, for all of his guidance, encouragement, and support throughout my graduate studies. I have learned not only the methodologies for research from him, but the principles for living a happy life. One of the most important lessons is “rest, if you must, but don't you quit,” which will benefit me for the rest of my life.

I am grateful to Dr. Daniel J. Inman with Center for Intelligent Material Systems and Structures (CIMSS) in Mechanical Engineering Department of Virginia Tech. He provided valuable technical advice and tremendous help on testing of our prototypes and publications. I would also like to thank Dr. Fred C. Lee with the Center for Power Electronics Systems (CPES) for his support and advice. It was my precious experience to learn power electronics from him. His rigorous attitude toward research is what I would like to pursue in my future career. I would also like to extend my appreciation to Dr. Joseph G. Tront and Dr. Patrick Schaumont for serving on my advisory committee.

I gratefully acknowledge the support of the U.S. Department of Commerce, National Institute of Standards and Technology, Technology Innovation Program, Cooperative Agreement Number 70NANB9H9007, USA.

I would like to express my special thanks to Dr. Ming Xu. Being his student is my great honor. I deeply respect him not only for his broad knowledge, but the spirits of helping others. I would also like to thank Dr. Michael Hsiao for his advice and suggestions for my research.

I am thankful for the support and help of my fellow members of Virginia Tech VLSI for Telecommunications (VTVT) laboratory. It has been a great pleasure working with them – Shen Wang, Rajesh Thirugnanam, Jina Kim, Vipul Chawla, Jeongki Kim, Jihoon Jeong, Jinsik Yun, Yumi Lim, Hung-Chih Lin, Jeannette D. Djigbenou, Dao Zhou, Qian Wang, Justin Cartwright, Travis Cochran, T. Shaver Deyerle, John Turner, and Jebreel M. Salem.

I also appreciate the colleagues of CIMSS – Alper Erturk, Steve Anton, Justin Farmer, Amin Karami, Scott Bressers, Bryan Joyce, Ya Wang and Yu Zhao. I enjoyed working with them very much.

I would also like to thank the members of CPES, with whom I studied and worked together – Zheng Zhao, Ying Lu, Jian Li, Yi Sun, Bin Huang, Fang Luo, Xiaoyong Ren, Qiaoliang Chen, Shu Ji, Chuanyun Wang, Zheng Luo, Dianbo Fu, Ya Liu, Yan Dong, Michele Lim, Julu Sun, Jing Xu, Yan Jiang, Pengju Kong, Feng Zheng, Brian Cheng, Rixin Lai, Qiang Li, Yucheng Ying, Di Zhang, Puqi Ning, Pengjie Lai, Zijiang Wang, Qian Li, Daocheng Huang, Ruxi Wang, Dong Dong, Xiao Cao, Dong Jiang, Zhiyu Shen, Feng Yu, Weiyi Feng, Mingkai Mu, Haoran Wu, Wei Zhang, Shuilin Tian and Li Jiang.

In addition, I am grateful to people who helped me on my research. Thanks to Jin-Biao Huang for giving me the lecture of ESD devices and IC design. Thanks to Mark Hagen for giving me a new perspective on digital control. Thanks to Ali Davoudi for the tremendous help on my publications.

Finally, special thanks to Yipeng Su for being the best boyfriend in the world. I would also like to thank my parents, Fansen Kong and Yuchun Liu, for their continuous support and encouragement for all my endeavors.

Table of Contents

List of Figures

List of Tables

Chapter 1: Introduction

Wireless sensor nodes (WSNs) have been pervasive in the past decade and used in various applications such as industrial process monitoring, healthcare, home automation, and structural health monitoring (SHM). However, the batteries used to power WSNs have become a major roadblock for wide deployment of those systems, especially the SHM systems for infrastructures [1]-[3]. Due to the limited access to civil and military infrastructures, a substantial cost is imposed for repeated maintenances of the batteries such as replacement and recharging. The power required for WSNs may range from a few microwatts to hundreds of milliwatts. Extensive research has been conducted to reduce the power dissipation of WSNs through various means, including exploitation of low duty cycles [2] and low-power design of sensors, circuits, and systems [4]. Another avenue taken to address the problem is energy harvesting from ambient sources such as solar, wind, vibration, heat and radio frequency radiation [5]-[16], which provides possible means to recharge the batteries or eliminate them.

Among existing energy harvesting sources, vibration energy harvesting has attracted immense research interest owing to its relatively low cost and high power density. Extensive discussions about vibration energy harvesting can be found in existing review articles [17]-[20]. Ambient vibrations are present in various environments, such as automotive vehicles, buildings, structures (e.g. bridges and railways), industrial machines, and household appliances. For some applications such as SHM, which is the target application for this research, energy harvesting for mechanical vibrations is suitable. Mechanical vibration energy can be extracted using a suitable mechanical-to-electrical energy converter (or generator) such as electromagnetic, electrostatic, or piezoelectric transduction devices as first mentioned in [21]. Here we focus on harvesting ambient harmonic vibration using the piezoelectric effect, which has received great attentions and been reviewed in the most recent literatures [22]-[23].

Raw power harvested from ambient sources should be conditioned and regulated to a desired voltage level before its application to electronic devices. A vibration-based power generator converts the mechanical vibration energy into AC electrical power. Since microelectronic devices and rechargeable batteries usually require a DC power supply, a power conditioning and management circuitry is necessary to rectify the AC power to stable DC power in an efficient manner.

The efficiency of a power conditioning and management circuit is a key design issue. It is affected by several factors including the impedance mismatch between the energy transducer and the conditioning circuit, power losses associated with underlying components, and the power management strategy employed. Design of power management (PM) circuits to harvest maximal energy from piezoelectric patches has been investigated rather intensively in recent years [24]-[35]. A rectifier circuit followed by a DC-DC converter is the common practice for power conditioning of piezoelectric energy harvesting. A DC-DC converter servers two purposes. The first one is to generate a stable DC output voltage; the other one is to provide a matched impedance for the harvester to deliver the maximum power. Buck, boost, buck-boost converters shown in Figure 1.1 are commonly used for this stage. Such a DC-DC converter consists of a switch, an inductor, a diode, and an output capacitor. The DC input voltage is converted into a DC output voltage and the ratio is set by the duty cycle, which is defined as the fraction of time when the switch is turned on.

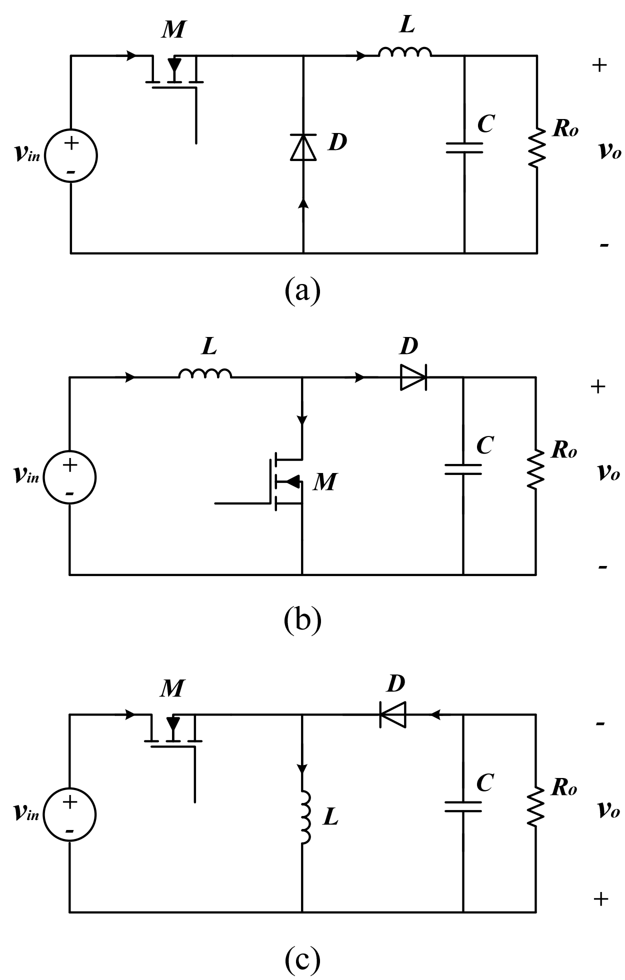

Figure 1.1 Three basic DC-DC converters: (a) buck, (b) boost, (c) buck-boost.

The PM circuit in [31] utilizes a rectifier and a buck converter for power conditioning. By tuning the rectified voltage through adjustment of the duty cycle, the circuit can operate at the optimal operating condition to harvest the maximum power. The circuit employs a DSP-based controller powered by an external power source, and the controller consumes more power than it can harvest from a typical size piezoelectric cantilever. Later, in order to reduce power dissipation, the processor is replaced with discrete components and the converter runs at a fixed duty cycle, while giving up dynamic tracking of the maximum power point [32]. The controller dissipates around 5.74 mW power, which is far less than a DSP based controller, but still excessive for the intended application. The self-powered management circuits in [33] and [35] give up dynamic tracking in favor of power reduction of the driving circuit to several microwatts. However, absence of dynamic tracking of the maximum power point results in low efficiency due to changing environmental conditions.

Another important requirement of a PM circuit for energy harvesting is the stand-alone operation, especially the ability to cold start. A rudimentary solution for start-up problem is to include a precharged battery, as adopted by most existing self-powered energy harvesting systems [27]-[30], [36]-[38]. However, if the battery of a such system is discharged completely, the system fails to self-start. To our knowledge, existing PM circuits capable of dynamic tracking of the maximum power point have not addressed the start-up problem.

Motivated by aforementioned problems, the characteristics of piezoelectric cantilevers are studied; efficient and self-powered power management circuits to harvest the maximum energy from piezoelectric generators are designed and implemented in this thesis.

First, characteristics of wireless sensor nodes, a model of piezoelectric harvesters and the previous approaches for power conditioning circuits are reviewed. Then, the interface circuit design is considered from the impedance matching perspective. The power extraction efficiency achieved through a complex conjugate matching load and a resistive impedance matching load are compared through circuit simulation for a typical bimorph piezoelectric cantilever. We concluded that a resistive impedance matching is an acceptable comprise. An open-loop two-stage conditioning circuit with a rectifier and a buck-boost converter is proposed to achieve the resistive impedance matching and handle a wide input voltage range. Experimental results are presented to validate effectiveness of the proposed resistive impedance matching circuit.

In order to achieve dynamic impedance matching, a low-power closed-loop power management circuit for piezoelectric energy harvesting is presented in this thesis. Several low-power design schemes to reduce power dissipation of the proposed system are described. A discontinuous conduction mode (DCM) flyback converter with the constant on-time modulation is adopted for resistive impedance matching. The DCM operation of a flyback converter is chosen for maximum power point tracking (MPPT) to be implemented with a single current sensor. The constant on-time modulation lowers the clock frequency of the controller by more than an order of magnitude, which reduces the dynamic power dissipation of the controller. MPPT implemented in a microcontroller unit (MCU) is executed at intermittent time intervals to exploit a relatively slow change of the operating condition. When MPPT is inactive, the MCU operates at a lower clock frequency to save power. The MCU usually already exists in a WSN. Therefore the use of MCU does not require extra hardware. The proposed circuit is able to cold start without relying on a backup battery. The low-power design features presented in this thesis can be readily applied to other types of energy harvesting systems such as small scale wind turbines and solar panels in a straightforward manner. In order to increase the power conversion efficiency, the sources of the power loss are analyzed, and a breakdown of the measured power loss is presented. The diode in the flyback converter and the controller (specifically the MCU) are the two major sources for the power loss and account for 63 percent of the total power loss. Motivated by the results, a full custom integrated circuit (IC), which was developed in a 0.18-μm CMOS process, is presented in this thesis. It adopts a single stage buck-boost converter with a closed-loop control to accommodate a wide input voltage range under varying environmental conditions. Synchronous rectifiers, instead of the diode, are used to reduce the conduction loss. A mixed-signal control circuit is designed to replace the power consuming MCU.

In summary, the contributions of the thesis are as follows.

(i) The power conditioning circuit design is considered from the impedance matching perspective. Resistive impedance matching is an acceptable comprise for typical piezoelectric cantilevers for energy harvesting.

(ii) A closed-loop self-powered resistive impedance matching circuit with a MCU based MPPT is proposed and implemented.

(iii) A full custom power management IC is implemented to reduce the losses of the MCU and discrete components.

Chapter 2:
Background

To design a highly efficient power management circuit for piezoelectric energy harvesting in wireless sensor nodes, the characteristics of wireless sensor nodes, the modeling of piezoelectric cantilevers and the previous approaches for the power conditioning circuit are studied in Chapter 2.

2.1 Wireless Sensor Nodes (WSNs)

WSNs are used to sense environmental phenomena and transmit data. The history of WSNs dates back to 1998 for the DARPA-funded Smart Dust project [39]. Now WSNs are used in many industrial and civilian application areas, including industrial process monitoring and control, machine health monitoring, environment monitoring, healthcare applications, home automation, and traffic control. Figure 2.1 shows the architecture of a WSN. A typical WSN consists of a number of functional blocks which include sensors, microcontroller, transceiver, external memory and power source.

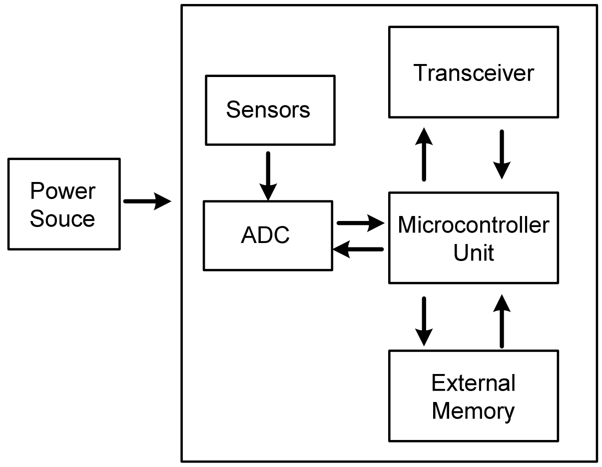

Figure 2.1 Architecture of a wireless sensor node [40].

Sensors measure physical or environmental conditions, such as temperature, sound, vibration, pressure, motion or pollutants. The continuous analog signal measured by the sensors is digitized by an analog-to-digital converter (ADC) and sent to a microcontroller unit (MCU). The MCU performs data processing and controls the functionality of other components in the sensor node. In some cases, where local signal processing is required, a digital signal processing (DSP) chip or field programmable gate array (FPGA) may also be used [2]. The use of external memories depends on applications. From an energy perspective, on-chip memory of a microcontroller and flash memory are the most relevant kinds of memory. Radio frequency (RF) communication is the wireless transmission media that fits most of the WSN applications. WSNs use the communication frequencies between about 433 MHz and 2.4 GHz [40]. Both transmitter and receiver are combined into a single device known as transceivers. The power source consists of standard primary batteries or rechargeable batteries. Power consumption in the sensor node is for the sensing, data processing and communication. The lifetime of each node will depend on the duty cycle and the amount of data being sensed and transmitted.

WSNs are characterized to have small size, operate in high volumetric densities, be autonomous and operate unattended [1]. Batteries have become the roadblock for the wide deployment of WSNs due to the bulky size and limited life time. For example, one objective of Smart Dust project is to create autonomous sensing and communication system with dimensions not bigger than a cubic millimeter. The most recent version of a Smart Dust sensor node had a volume of 63 mm^3[41]. The sensor node was made of a microelectromechanical system (MEMS), optics chip for communication, a complementary metal-oxide-semiconductor (CMOS) IC, and a Li–Mn button-cell battery. The IC chip had a size of only 0.078 mm^3, but the battery occupied the majority of the node volume. Moreover, due to the high volumetric densities and limited access to the nodes, the repeated maintenance of the batteries has imposed substantial excess cost for the deployment of WSNs.

Ultra low power sensors and electronics are developed to minimize the power consumption of WSNs. Duty cycling based on long sleep times is adopted to prolong the life time of batteries [2]. The wireless system remains in a low power sleep mode for most of the time, the sensor node components will be active only for the time required to perform the operations of sensor sampling, data processing and wireless data transmission or communication. Figure 2.2 shows the measured current of a wireless sensor node using Texas Instruments eZ430-RF2500 [4] for SHM.

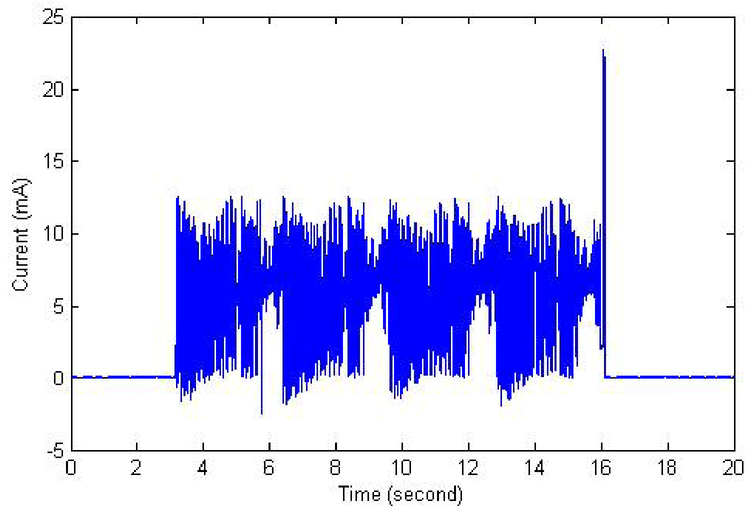

Figure 2.2 Measured current of a wireless sensor node [42].

Two AAA batteries are used as the power source with a voltage of 3V. The measured current under the inactive mode is about 50 μA resulting in a power consumption of 0.15 mW. The current increases to 6 mA during the active mode with the transceiver off, which results in 18 mW of power consumption. The active mode lasts for about 13 seconds to consume 234 mJ of energy. When the transceiver is turned on at the end of the active mode, the current jumps abruptly to 23 mA to cause 70 mW power consumption. The period lasts for about 0.03 second resulting in 2.1 mJ of energy consumption. Assuming the capacity of an AAA battery is 1200 mAh and the SHM routine operates once in every four hours. The batteries can only run for about 2.5 years. Under the low duty cycling operation, the average power consumption is 0.16 mW. The average power consumption has dropped to sub-miliwatt and makes the power harvesting a possible solution to replace traditional power sources. The concept of power harvesting works towards developing self-powered devices that do not require maintenance of batteries.

2.2 Piezoelectric Energy Harvesting

The energy sources in the environment include but are not limited to solar energy, heat, vibrations and radiofrequency (RF) radiation. The available power density of the energy harvesters is tabulated in Table 2.1 according to recent publications [2].

Table 2.1 Typical data for various energy harvesting techniques [2].

Energy Source	Conditions	Power density
Solar	Outdoor	7.5 mW/cm^2
Solar	Indoor	100 $\mu W/cm^2$
Thermal	$\Delta T=5^\circ C$	100 $\mu W/cm^2$
Vibration	1 m/s^2	60 $\mu W/cm^3$
RF	Unless near a transmitter	<1 $\mu W/cm^2$

Ambient vibrations are present in various environments, such as automotive vehicles, buildings, structures (e.g. bridges and railways), industrial machines, and household appliances. For some applications such as SHM, which is the target application for this research, mechanical vibration is suitable energy source for powering WSNs.

Fundamental vibration frequencies ranged from 13 Hz (automobile instrument panel) to 385 Hz (wooden deck with pedestrians). The fundamental frequency of the majority of surfaces tested was around 60-100 Hz. The acceleration magnitude ranged from 0.1 m/s^2 (refrigerator) to 12 m/s^2 (car engine compartment) [17]. Vibration-based power generators convert the mechanical energy of vibrating surfaces into electrical energy using a suitable mechanical-to-electrical energy converter (or generator) such as electromagnetic, electrostatic or piezoelectric transduction devices. Vibration power generators for energy harvesting must be designed to operate within these ranges of source frequency and acceleration. Here we focus on harvesting ambient harmonic vibration using the piezoelectric effect because of the relatively high power density [19].

Piezoelectric generators make use of the piezoelectric properties of some materials which develop a voltage when stressed. The vibration is used to stress the piezoelectric element, thus developing a voltage which can be extracted as electrical energy. Typically, a piezoelectric energy harvester is a cantilevered beam with one or two piezoceramic layers (a unimorph or a bimorph). Figure 2.3 shows a typical bimorph cantilever configuration [11]. *S* is strain, *V* is voltage, *M* is mass, and *z* is vertical displacement. A mass is placed on the free end to tune the resonant frequency of the system. By convention, the 3-axis is the direction of the material poled along and electrodes are placed on the surfaces perpendicular to the 3-axis. Driving vibrations are assumed to exist only along the 3-axis. Given these assumptions, the piezoelectric material experiences a one-dimensional state of stress along the 1-axis.

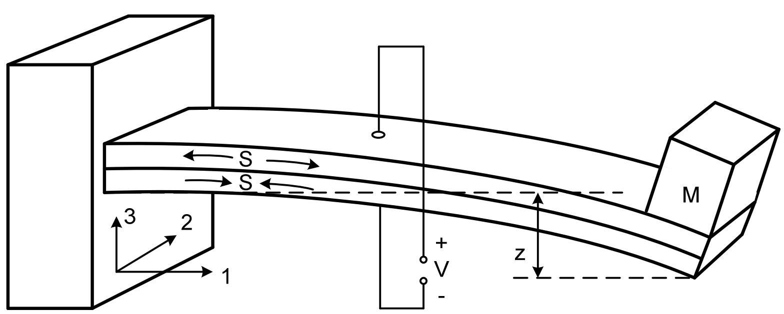

Figure 2.3 A two-layer bender mounted as a cantilever [11].

2.2.1 Model of Piezoelectric Generators

A generic model for the conversion of the kinetic energy of a vibrating mass to electrical power based on the schematic in Figure 2.4 has been proposed by Williams and Yates [21]. The mass-spring-damper system has been widely used for analysis for piezoelectric energy harvester. The model is composed of a dynamic rigid mass M, a spring K_S modeling the host structure stiffness, a viscous damper D modeling the mechanical losses, and an equivalent piezoelectric disk with capacitance C_P modeling the piezoelectric elements bonded on the structure. F corresponds to the external force applied to the structure. The model is given by (2.1) in which K is the sum of the host structure stiffness K_S plus the piezoelectric element stiffness K_{PE}; u is the displacement of the piezoelectric cantilever; V is the voltage across the disk electrodes, I is the outgoing current and α is the force factor, reflecting the effective piezoelectric coupling coefficient.

$$\begin{cases} M\ddot{u} + D\dot{u} + Ku + \alpha V = F \\ -\alpha\dot{u} + C_P\dot{V} = -I \end{cases} \tag{2.1}$$

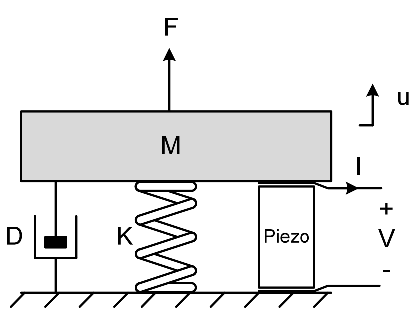

Figure 2.4 Schematic representation of the electromechanical model [26].

The electromechanical system in (2.1) can be represented using equivalent circuit elements [11],[43]. In [11], the single-degree-of-freedom (SDOF) (i.e., lumped parameter modeling) solution is developed. Although SDOF modeling gives initial insight into the problem by allowing simple closed-form expressions, it is limited to a single vibration mode and it lacks important aspects of the physical system, such as the dynamic mode shape and accurate strain distribution along the bender [44]. Ref [44] and [45] address this problem and give an analytical closed-form solution of a cantilevered piezoelectric energy harvester based on distributed-parameter formulation. Later, single-mode and multi-mode electrical circuit representations using the Rayleigh-Ritz formulation were presented in [43] along with verifications against the former analytical solution. The circuit model can be easily extended to capture any number of vibrational modes. Figure 2.5 shows the equivalent circuit for a piezoelectric generator in which the first two modes are of interest. In the equivalent circuit, the equivalent mass M_{ii}, stiffness K_{ii}, and damping D_{ii} (i = 1, 2) is represented by an inductor, capacitor, and resistor. The electromechanical coupling is represented by an ideal transformer. The symbols $\dot{u}_i$, n_i, and F_i (i = 1, 2) represent the velocity, piezoelectric coupling, and force in the system.

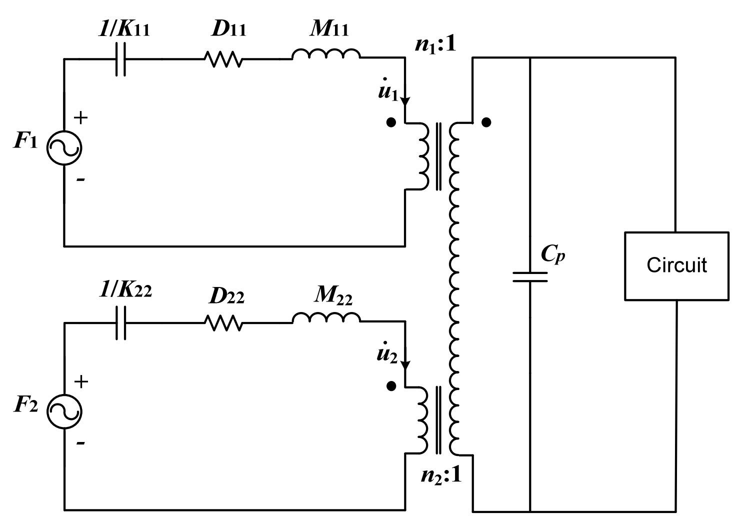

Figure 2.5 The equivalent circuit for a piezoelectric generator [43].

This equivalent circuit decouples the mechanical and electrical systems, which enables us to predict electrical output with different loading conditions and to optimize the power conditioning circuit easily. Computer programs for circuit simulation also can be applied to help the analysis.

2.2.2 Energy Flow in Piezoelectric Generators

The energetic analysis is derived in (2.2) by calculating the mechanical energy provided to the system from the external driving force *F*. According to this equation, the energy provided by the external driving force is distributed into the kinetic energy, the mechanical losses, the elastic energy, and the energy converted into electricity by the piezoelectric element.

$$\int F\dot{u}dt = \frac{1}{2}M\dot{u}^2 + \int D\dot{u}^2 dt + \frac{1}{2}Ku^2 + \int \alpha V\dot{u}dt \tag{2.2}$$

Ref [46] analyzes the energy flow in a piezoelectric energy harvesting device as shown Figure 2.6. The mechanical and electrical energy are linked by the bi-directional piezoelectric transducer. At the same time, mechanical and electrical energy can be converted into thermal energy by dissipative elements such as mechanical dampers or electrical resistors. During each cycle, the ambient vibration source injects energy A into the system in mechanical form. Energy A converts into three parts: the vibration energy cycling in the mechanical domain (loop B–D–E–K–L–B), thermal energy C, and electrical energy F. In the electrical domain, the electrical energy is also converted into three parts: thermal energy G, stored electric energy I for powering electric loads, and vibration energy J returning to the mechanical domain. Finally, if the total mechanical impedance of the piezoelectric device does not match the impedance of the ambient vibration source, some energy M will return to the source.

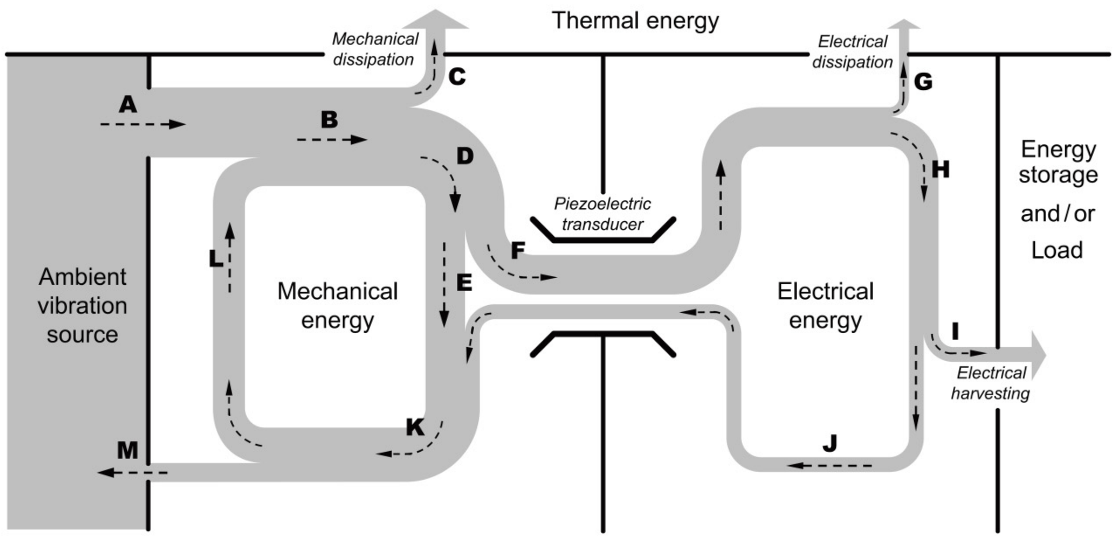

Figure 2.6 Energy flow chart in general piezoelectric energy harvesting devices [46] (used with permission of IOP Publishing Ltd).

2.3 Power Conditioning Circuits

For piezoelectric generators, the dynamic strain induced in the piezoceramic layers generates an AC voltage output across the electrodes. Since microelectronic devices and rechargeable batteries usually require a DC power supply, a power conditioning circuitry is necessary to rectify the AC power to stable DC power before the application to the electrical loads. Therefore, the power conditioning circuit usually includes a rectifier. Since the piezoelectric generators have relatively high internal impedance, which is different from conventional power supplies, the power conditioning circuit has to match source impedance for maximum power extraction. Often a DC-DC converter is connected after the rectifier to regulate the rectified voltage for the maximum power transfer. For weakly coupled energy harvesting devices, a switched-inductor based series of circuits have been used for increasing the power output. In this section, the previous approaches of AC-DC rectification, DC-DC converters for maximum power extraction and switched-inductor based circuits are briefly reviewed.

2.3.1 AC-DC Rectification

Full-wave bridge rectifier shown in Figure 2.7 is the most common circuit for rectification in piezoelectric energy harvesting system. The circuit consists of a rectifier followed by a filtering capacitor and a load resistor, which is sometimes referred to as the standard power conditioning circuit.

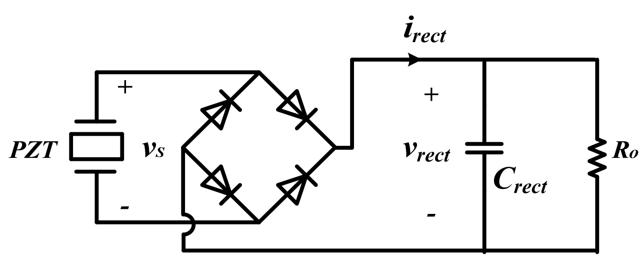

Figure 2.7 Standard power conditioning circuit [47].

Shu and Lien [47] investigated the steady state response and the harvested power from the standard power conditioning circuit. The derivation used the lumped-parameter electromechanical model in (2.1). The analysis is based on the assumption that the forcing function is a sinusoidal excitation of the form shown in (2.3):

$$F(t) = F_0 \sin(\omega t), \tag{2.3}$$

where F_0 is the constant excitation amplitude and ω is very close the resonance frequency. Equation (2.4) from [47] gives the normalized power output under different load conditions:

$$\overline{P}=\frac{P}{\dfrac{F_0^2}{\omega_n M}}=\frac{1}{\left(r\Omega+\dfrac{\pi}{2}\right)^2}\frac{k_e^2\Omega^2 r}{\left[\left(2\zeta+\dfrac{2k_e^2 r}{\left(r\Omega+\dfrac{\pi}{2}\right)^2}\right)^2\Omega^2+\left(1-\Omega^2+\dfrac{\Omega k_e^2 r}{r\Omega+\dfrac{\pi}{2}}\right)^2\right]} \tag{2.4}$$

The dimensionless terms are

$$k_e^2=\frac{\alpha^2}{KC_P},\quad \zeta=\frac{D}{2\sqrt{KM}},\quad r=C_P R\omega_n,\quad \Omega=\frac{\omega}{\omega_n},\quad \omega_n=\sqrt{\frac{K}{M}}, \tag{2.5}$$

where ω_n is the short-circuit natural frequency, k_e^2 is the electromechanical coupling factor, ζ is the mechanical damping ratio, r is the dimensionless resistance and Ω is the dimensionless frequency. There are two resonances for the system since the piezoelectric structure exhibits both short circuit and open circuit stiffness. The normalized short- and open circuit resonant frequency are defined as

$$\Omega_{sc}=1,\quad \Omega_{oc}=\sqrt{1+k_e^2}. \tag{2.6}$$

As coupling factor increases, the splitting of the two resonances is more pronounced. From (2.4), the average power output increases as mechanical damping ratio ζ decreases. The average power output with optimal load resistor under different electromechanical coupling factors is shown in Figure 2.8. When the electromechanical coupling factors

k_e^2 is small, the average power output increases as k_e^2 becomes larger. Eventually, the average power saturates when k_e^2 further increases.

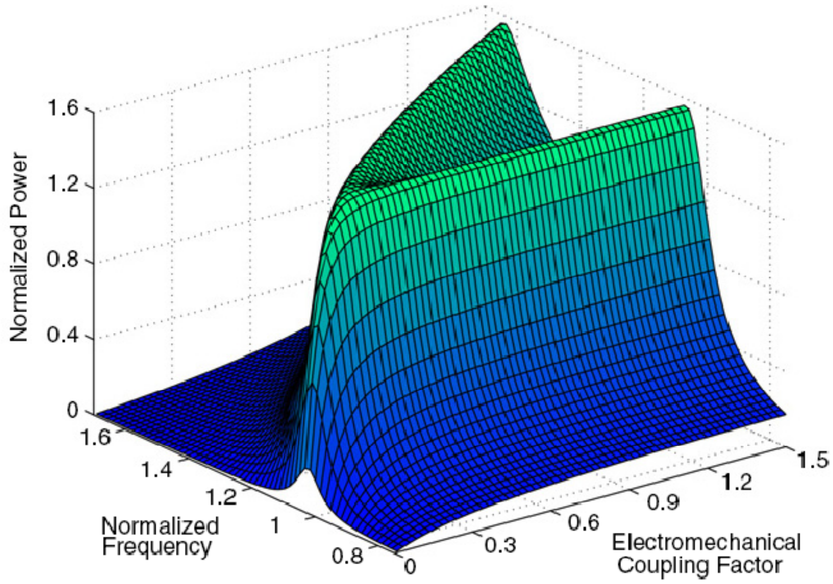

Figure 2.8 The normalized power P (for ζ = 0.04) against the normalized frequency Ω and the electromechanical coupling factor k_e^2 at the optimal conditions [48] (used with permission of IOP Publishing Ltd).

Since the analysis of Shu and Lien takes into account the effect of power generation on the harvester, it improves the power estimation compared to the previous approaches of Ottman et al. [31] and Guyomar et al. [25]. Ref [31] assumes that the vibration amplitude is not affected by the electric load, which is equivalently to assume the electromechanical coupling is very weak. Ref [25] assumes that the external force and the velocity of the mass are in phase for structures with low viscous losses. Shu and Lien reveal that when the coupling coefficient and quality factor of the system are large, the un-coupled model and in-phase approach have significant discrepancies in power prediction. The conventional un-coupled solution and in-phase estimate are suitable provided that $\frac{k_e^2}{\zeta} = \frac{2\alpha^2}{\omega_n C_P D} << 1$.

In order to reduce the power consumption caused by diodes due to its finite forward voltage drop, the gate cross-coupled MOSFET-based rectifiers [49],[50] (in Figure 2.9) and active rectifiers [51] (in Figure 2.10) are used for integrated circuit design for improving conversion efficiency, and typically used for inductive or electromagnetic energy harvesting.

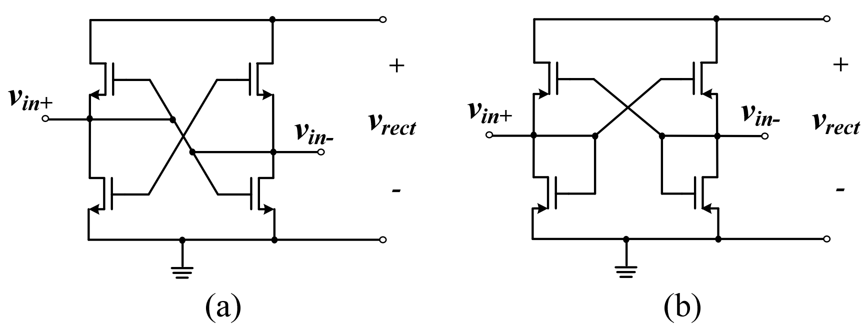

Figure 2.9 Gate cross-coupled MOSFET-based rectifiers: (a) NMOS; (b) PMOS. [50]

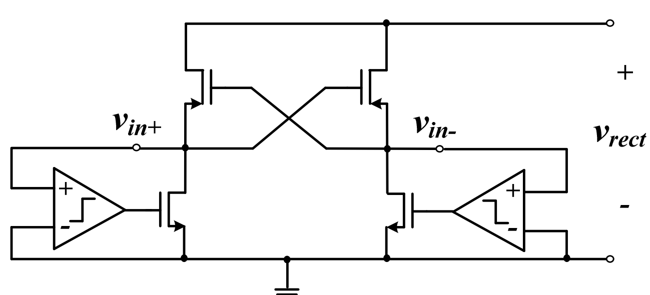

Figure 2.10 Active rectifier with cross-coupled PMOS switches [51].

Other than full-wave rectifier, voltage doubler shown in Figure 2.11 is also used for rectification [52],[36]. Since the maximum power is extracted at higher voltage and lower current, compared to full-wave rectifier, voltage doubler circuits provide a higher efficiency [30].

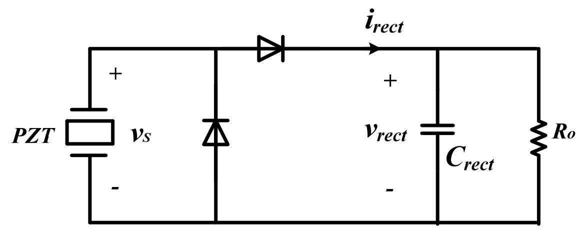

Figure 2.11 Voltage doubler for a piezoelectric generator [36].

2.3.2 DC-DC Converters for Maximizing Power Extraction

In order to tune the load resistor to the optimal value or equivalently tune the DC voltage at the output of rectifier, DC-DC converter is usually applied as the second stage of power conditioning circuit for piezoelectric energy harvesting system [31]-[34], as shown in Figure 2.12.

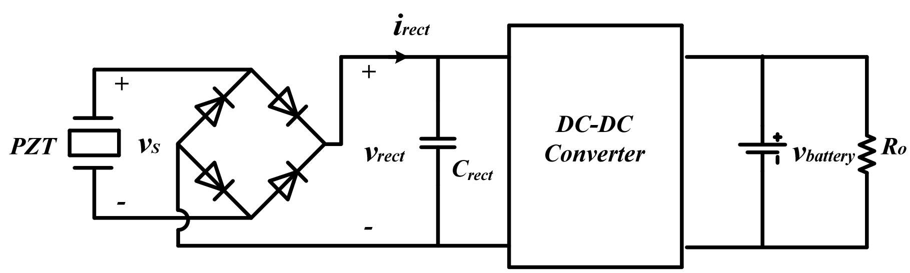

Figure 2.12 Two-stage power conditioning circuit.

Ref [31] presented an adaptive solution using the buck converter as the second stage (Figure 2.13). The circuit employs a DSP-based controller powered by an external power source, and the controller consumes more power than it can harvest from a typical size piezoelectric cantilever. Later, in order to reduce power dissipation, the processor is replaced with discrete components and the converter runs at a fixed duty cycle, while giving up dynamic control [32]. The controller dissipates around 5.74 mW power, which is far less than a DSP based controller, but still excessive for the intended application. Moreover, the buck converter can only work when the input voltage is higher than its output voltage, which limits the application of the circuit to vibration harvesters generating voltage higher than the output voltage. For example, for piezoelectric power generators excited by low-level accelerations, buck converters cannot be used directly due to low voltage output from the device.

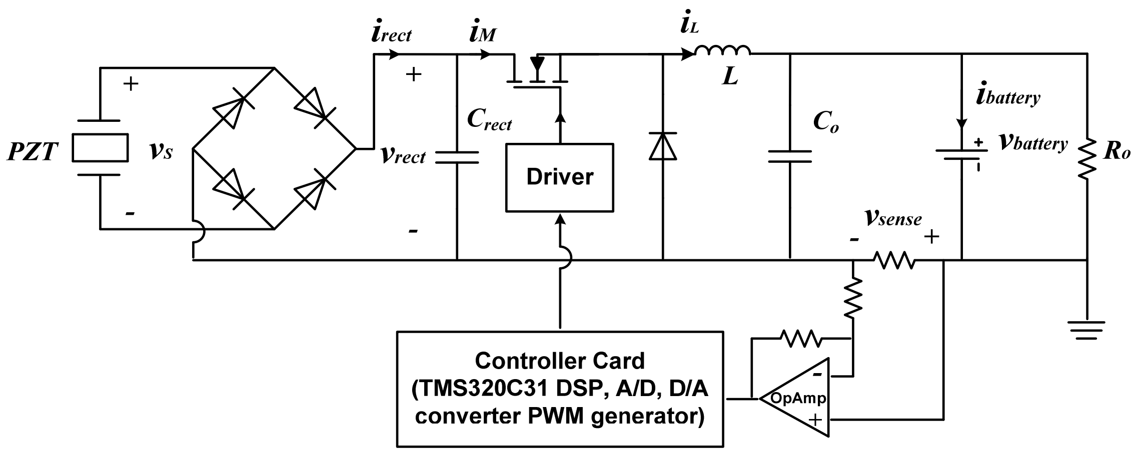

Figure 2.13 Adaptive energy harvesting circuit in [31].

A DC-DC converter should be able to step up or step down the input voltage, so it can be applied for a wide range of energy harvesters. Some traditional DC-DC converters can provide this, such as buck-boost, flyback, and Sepic converters. Also importantly, these converters operating in discontinuous conduction mode (DCM) mode behave as a lossless resistor, and the resistance is a function of the duty cycle and the switching period, rather than the input or output voltages of the converter [53]. A buck-boost converter requires a smaller number of components compared with flyback and Sepic converters and hence less complex, hence Ref [33],[34] proposed to use DCM buck-boost converter shown in Figure 2.14 functioning as a matched resistance. In order to reduce the power consumption of the control circuit, a low-power crystal clock with a fixed duty cycle and a fixed frequency was used to drive the power switch for their circuit [33]. Unfortunately, it makes the circuit less flexible for various piezoelectric generators and limits on the output voltage of the generator due to a limited voltage range of the crystal clock.

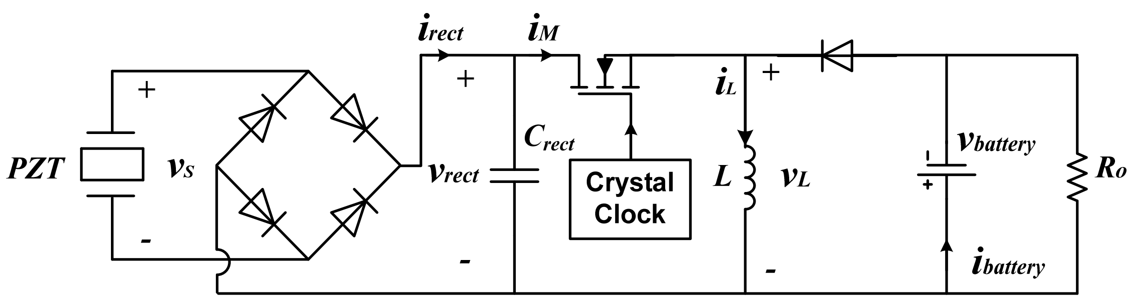

Figure 2.14 Power conditioning circuit in [33].

Another important requirement of a PM circuit for energy harvesting is the stand-alone operation, especially the ability of the DC-DC converter to cold start. A rudimentary solution for start-up problem is to include a precharged battery, as adopted by most existing self-powered energy harvesting systems [27]-[30], [36]-[38]. However, if the battery of a such system is discharged completely, the system fails to self-start. To our knowledge, existing PM circuits capable of dynamic impedance matching have not addressed the start-up problem.

2.3.3 Switched-Inductor Circuits

For weakly coupled piezoelectric generator, the mechanical displacement is not affected by the electric load. The equivalent electric circuit is modeled as a sinusoidal current source in parallel with piezoelectric capacitance as shown in Figure 2.15.

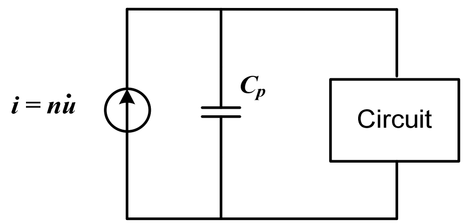

Figure 2.15 The equivalent circuit model for weakly coupled piezoelectric generator [31].

The basic principle of the power optimization is to shape the voltage delivered by the piezoelectric element in order to reduce the phase shift between voltage on piezoelectric disk and its outgoing current, and at the same time, to increase the voltage amplitude. Guyomar and his colleagues extended the concept of synchronized switch damping [24],[54] for structural vibration damping to the switched-inductor based circuits called synchronized switch harvesting on inductor (SSHI) [13],[25],[26],[55]-[57] for piezoelectric energy harvesting. In this section, two basic SSHI circuits – parallel SSHI and series SSHI – are reviewed and the comparison of the switched-inductor circuits with standard AC-DC rectification circuit is given.

2.3.3.1 Parallel SSHI

The parallel SSHI circuit is composed of an inductor L in series with an electronic switch S connected in parallel with the standard conditioning circuit (in Figure 2.7). The circuit is shown in Figure 2.16.

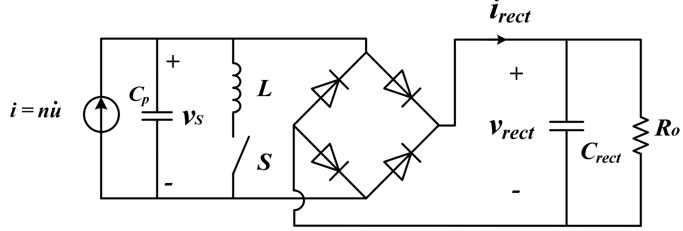

(a)

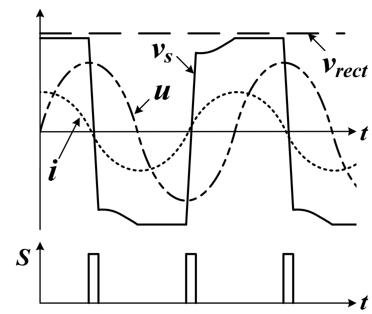

(b)

Figure 2.16 (a) Parallel SSHI circuit; (b) displacement, current and voltage waveforms [26].

The switch is turned on when the mechanical displacement reaches a maximum or a minimum. An L-C oscillation circuit is established. The electrical oscillation period is chosen much smaller than the mechanical vibration. The switch is turned off after a half of the electrical oscillation period, resulting in a fast voltage sign inversion on the piezoelectric element. Instead of charging by the piezoelectric element, the voltage polarity on the blocking capacitor is changed by the L-C oscillation circuit during a short time, that part of energy is greatly saved. Since the delivered voltage is phase shifted so that the voltage and the outgoing current are always on the same sign, leading to a maximization of the average converted power. Except the L-C oscillation interval, the piezoelectric element delivers power to the storage cell during the rest part of the period.

2.3.3.2 Series SSHI

The series SSHI technique in Figure 2.17 is very close to that of the parallel SSHI but the inductor and switching device are connected in series with the piezoelectric element and the rectifier input. The piezoelectric element is left as an open circuit most of time. Each time the switch is closing, the electric charge passing through the inductor L transmits a part of the energy stored in the piezoelectric blocking capacitor to the storage cell.

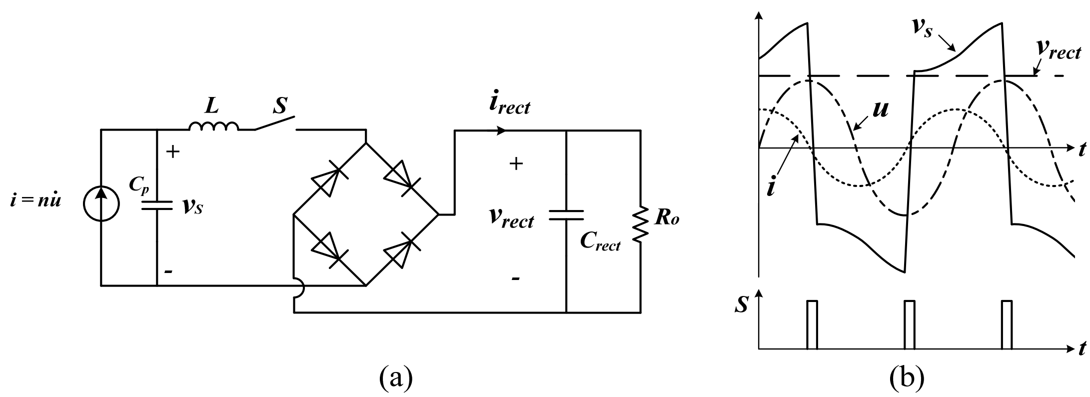

Figure 2.17 (a) Series SSHI circuit; (b) displacement, current and voltage waveforms [26].

2.3.3.3 Comparison of Switched-Inductor Circuits with Standard Circuit

The voltage inversion and hence the power output is limited by the quality factor of the inductor and the voltage drops across the switching devices. For weakly coupled piezoelectric generators, the harvested power by SSHI circuits can be increased by a factor of four or even higher compared to standard conditioning circuit (in Figure 2.7) [26]. However, the energy extraction process induces vibration damping. The advantages of SSHI circuits diminish when the electrical damping is significant hence the electromechanical system cannot be viewed as weakly coupled [25],[58],[59]. In contrast with estimates based on weakly coupled assumption, Shu et al. [48],[60] derived the analytic expressions of harvested power using SSHI technique based on the complete lumped-parameter model in (2.1). Equation (2.7) and (2.8) from [60] give the normalized power output of parallel and series SSHI circuits under different load conditions:

$$\overline{P}^{para-SSHI} = \frac{P^{para-SSHI}}{\frac{F_0^2}{\omega_n M}} = \frac{1}{\left(\frac{(1-q_I)}{2}r\Omega+\frac{\pi}{2}\right)^2}\frac{k_e^2\Omega^2 r}{\left(2\zeta\Omega+\frac{2\Omega k_e^2 r\left(1+\frac{r\Omega}{2\pi}(1-q_I)^2\right)}{\left(\frac{(1-q_I)}{2}r\Omega+\frac{\pi}{2}\right)^2}\right)^2+\left(1+\frac{k_e^2\frac{(1-q_I)}{2}r\Omega}{\frac{(1-q_I)}{2}r\Omega+\frac{\pi}{2}}-\Omega^2\right)^2} \tag{2.7}$$

$$\overline{P}^{series-SSHI} = \frac{P^{series-SSHI}}{\frac{F_0^2}{\omega_n M}} = \left[\frac{2(1+q_I)}{(1-q_I)\pi+2r\Omega(1+q_I)}\right]^2\frac{k_e^2\Omega^2 r}{\left(2\zeta\Omega+\frac{4k_e^2(1+q_I)}{(1-q_I)\pi+2r\Omega(1+q_I)}\right)^2+\left(1+k_e^2-\Omega^2\right)^2} \tag{2.8}$$

where q_I is the voltage inversion factor as a function of the inductor's quality factor Q_I as shown in (2.9).

$$q_I = e^{\frac{-\pi}{2Q_I}} \tag{2.9}$$

Other parameters are the same as defined in (2.5).

The results from [60] shown in Figure 2.18 are the power harvested by different electrical load and applied frequency for SSHI circuits and standard circuit under weak coupling ($k_e = 0.1, \zeta = 0.03, \frac{k_e^2}{\zeta} = 0.33$), medium coupling ($k_e = 0.3, \zeta = 0.03, \frac{k_e^2}{\zeta} = 3.0$)

and strong coupling ($k_e = 0.1, \zeta = 0.03, \frac{k_e^2}{\zeta} = 33.3$) with Q_I = 4.4. In Figure 2.18, (a) – (c) are obtained using the parallel-SSHI circuit with $\frac{k_e^2}{\zeta} = 0.33, 3.0, 33.3$ respectively; (d) – (f) are obtained using the standard conditioning circuit with $\frac{k_e^2}{\zeta} = 0.33, 3.0, 33.3$ respectively; and (g) – (i) are obtained using the series-SSHI circuit with $\frac{k_e^2}{\zeta} = 0.33, 3.0, 33.3$ respectively. SSHI circuits can significantly boost the harvested power of weakly coupled electromechanical systems. For strongly coupled system, SSHI circuits do not have obvious advantages over the standard system. Since there are two identical peaks of optimal power in the standard case, while there is only one peak of power in either parallel-SSHI or series-SSHI, standard circuit is preferred for broadband energy harvesting.

Some self-powered power management circuits based on the switched-inductor circuits are reported in [27]-[30]. The constraint for the circuit design is to process the piezoelectric voltage using the minimum of energy. Same to the standard DC-DC converter for maximizing power extraction, the SSHI circuit also requires a DC-DC conversion stage to tune the piezoelectric generator's output to the optimal value [30], which is a function of the environmental conditions. The optimal value is given as the reference voltage for the feedback control in [30]; however, it is not mentioned how this optimal value is obtained. Moreover, the control command for the switch which is synchronous to the extremes of displacement also can be costly in terms of energy consumption [28]. It is challenging to realize stringent timing control with reasonably low circuit complexity and low power consumption [28], [29].

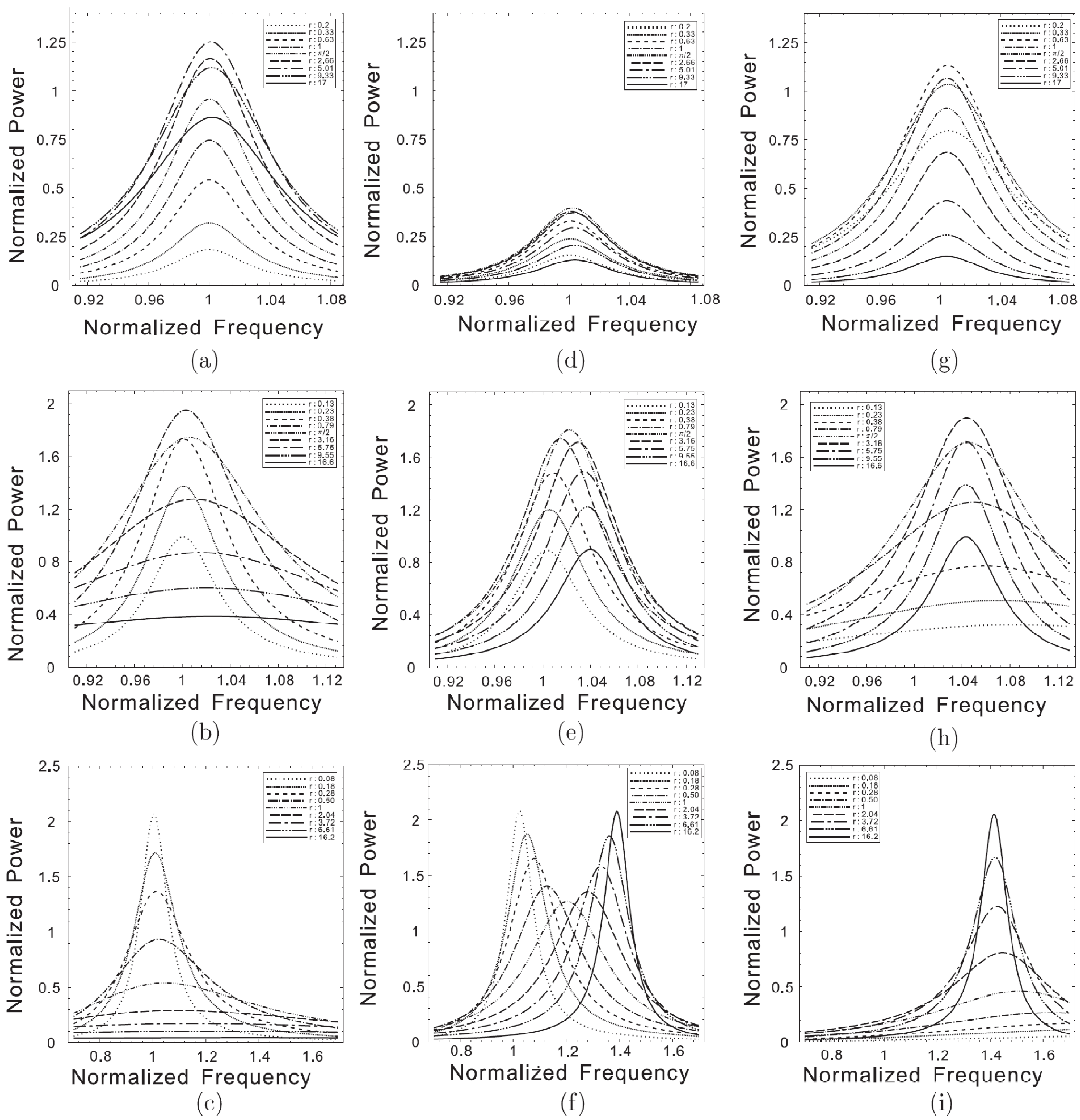

Figure 2.18 Normalized power versus frequency ratio for different values of normalized resistance [60] (used with permission of IOP Publishing Ltd).

2.4 Summary

In this chapter, the characteristics of WSNs are reviewed. Advances in low power sensors and electronics design along with the low duty cycle operation of wireless sensors have reduced power requirements to sub-microwatt. Such low power dissipation opens up the possibility of powering the WSNs by harvested energy from the environment, eliminating the need for repeated maintenance for batteries.

Piezoelectric generator has attracted great attention in the past five years because of the relatively high power density and it is the energy harvesting source of interest for this research. The property and model of piezoelectric generator are studied in this chapter. The equivalent circuit of piezoelectric decouples the mechanical and electrical systems, which will be used to design the power conditioning circuit in the following chapter.

The existing power conditioning circuits are reviewed. Rectifier circuit followed by a DC-DC converter is the common practice for the power conditioning of piezoelectric energy harvesting. The DC-DC converter servers two purposes. One is for generating a stable DC output voltage; another is providing a matched interface for the harvester to deliver maximum power. Buck, boost, buck-boost converters have been used for this stage. However, previous approaches either use external power supply to power the controller circuit or adopt open-loop operation to save power consumption. Self-powered circuit with dynamic control has not been developed.

The nonlinear circuits based on switched-inductor are proposed for weakly coupled system to increase the power output. However, the comparison of different power conditioning circuits indicated that for structures with low mechanical damping and/or with high electromechanical coupling, the less complex standard power conditioning circuit is preferred because of the higher power output and wider bandwidth.

Chapter 3:
Resistive Impedance Matching Circuit

As discussed in the previous chapter, the power conditioning circuit will affect the power extraction from piezoelectric generators. Standard configuration with rectifier and switched-inductor based nonlinear processing circuits are proposed to be the interface/conditioning circuits. The circuit analysis is complicated due to the coupling of electrical and mechanical energies and the existence of nonlinear elements. Here we propose to view the circuit design problem from the impedance matching perspective. The classic impedance matching theory is reviewed in Chapter 3.1. The equivalent circuit discussed in Chapter 2.2 decouples the mechanical and electrical systems, which enables us to predict electrical output with different loading conditions and to optimize the power conditioning circuit. Based on the equivalent circuit, the analysis from impedance matching perspective is given in Chapter 3.2 and the impedance matching circuit is proposed in Chapter 3.3.

3.1 Review of Impedance Matching Theory

3.1.1 Complex Conjugate Matching

The maximum power transfer occurs for a fixed AC source if the load impedance is the complex conjugate of the source impedance [61]. Consider an AC current source shown in Figure 3.1, for which $i_S(t)=\sqrt{2}I_S\sin(\omega t)$, the internal impedance is $Z_S = R_S + jX_S$ and the load impedance is $Z_L = R_L + jX_L$.

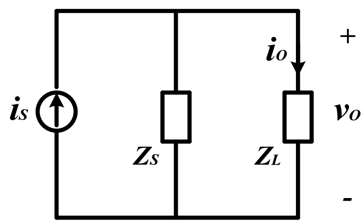

Figure 3.1 The circuit with an AC current source.

The average power delivered to the load is

$$P_o = I_{o,rms}^2 R_L = \left|\frac{Z_S}{Z_S+Z_L}\right|^2 I_S^2 R_L = \frac{R_S^2+X_S^2}{(R_S+R_L)^2+(X_S+X_L)^2} I_S^2 R_L \qquad (3.1)$$

When the load is the complex conjugate of the source impedance or

$$Z_{L,opt} = R_S - jX_S \qquad (3.2)$$

the maximum power is delivered, that is

$$P_{o,\max} = \frac{R_S^2+X_S^2}{4R_S} I_S^2 \qquad (3.3)$$

where the maximum power output is determined by the source properties only. The voltage output across the source or the load is called optimal voltage and is obtained as

$$V_{o,opt} = \frac{Z_S I_S}{Z_S+Z_{L,opt}} Z_{L,opt} = \frac{R_S+jX_S}{R_S+jX_S+R_S-jX_S} I_S(R_S-jX_S) = \frac{R_S^2+X_S^2}{2R_S} I_S \qquad (3.4)$$

where the optimal voltage is in phase with the current source.

The same conclusion can be drawn for a voltage source of $v_S(t) = \sqrt{2}V_S \sin(\omega t)$ shown in Figure 3.2. Then the maximum power delivered to the load and the optimal output current are given by (3.5) and (3.6), respectively:

$$P_{o,\max} = \left| \frac{V_S}{Z_S + Z_{L,opt}} \right|^2 R_{L,opt} = \frac{V_S^2}{(R_S + R_S)^2 + (X_S - X_S)^2} R_S = \frac{V_S^2}{4R_S} \tag{3.5}$$

$$I_{o,opt} = \frac{V_S}{2R_S} \tag{3.6}$$

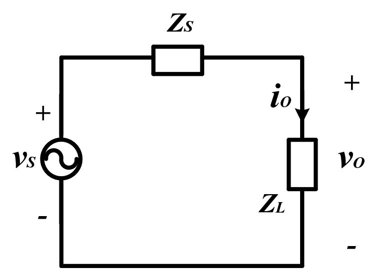

Figure 3.2 The circuit with an AC voltage source.

3.1.2 Resistive Impedance Matching

Although the conjugate matching load extracts the maximum power from the source, a direct impedance matching is usually impractical for piezoelectric energy harvesting due to the requirement of a huge inductor. An alternative and suboptimal approach is to use only a resistive load and try to match only the source impedance. The power delivered from a current source to a load resistance of R_L can be given by

$$P_o = \frac{R_S^2 + X_S^2}{(R_S + R_L)^2 + X_S^2} I_S^2 R_L = \frac{R_S^2 + X_S^2}{R_L + \frac{(R_S^2 + X_S^2)}{R_L} + 2R_S} I_S^2 \tag{3.7}$$

The optimal load resistance maximizing the power delivery to the load and the optimal power for the resistive load can be obtained from (3.8) and (3.9), respectively:

$$R_{L,opt} = \sqrt{R_S^2 + X_S^2} \tag{3.8}$$

$$P_{o,\max} = \frac{R_S^2 + X_S^2}{2\left(\sqrt{R_S^2 + X_S^2} + R_S\right)} I_S^2 \tag{3.9}$$

Clearly, the power delivered to the resistive load (given by (3.9)) is smaller than the optimal power delivery under the complex conjugate matching (given by (3.3)). The resistive load matching becomes less efficient for large values of the reactive source component.

The same conclusion can be drawn for a voltage source of $v_S(t) = \sqrt{2} V_S \sin(\omega t)$. Then the maximum power delivered to the resistive load is given by (3.10):

$$P_{o,\max} = \left| \frac{V_S}{Z_S + R_{L,opt}} \right|^2 R_{L,opt} = \frac{V_S^2 \sqrt{R_S^2 + X_S^2}}{\left(R_S + \sqrt{R_S^2 + X_S^2}\right)^2 + \left(X_S\right)^2} \tag{3.10}$$

3.2 Impedance Matching for Piezoelectric Generators

3.2.1 Source Impedance of Piezoelectric Generators

The equivalent circuit based on the Rayleigh-Ritz formulation is shown in Figure 3.3 for the fundamental mode. The voltage generator $v = m^* a$ represents the effective force induced by the base vibration and is the only source in the electrical model, where m^* is the effective mass term and a is the base acceleration amplitude. The product

$m^* a$ is the effective inertia of the cantilever, which is the forcing term in the base excitation problem. The current i_S out of the voltage source v is the velocity of the tip mass at the end of the beam along 3-axis, i.e. the derivative of the displacement u of the tip mass. The equivalent inductance $L = M_{11}$ represents the modal mass of the first mode. The resistance $R = D_{11}$ and the capacitance $C = 1/K_{11}$ represent mechanical damping and compliance (reciprocal of stiffness), respectively. The electromechanical coupling is modeled as a transformer with the turn-ratio n representing the piezoelectric coupling vector. C_P is the equivalent inherent capacitance of the piezoceramic layers. Typically, the leakage resistance of the piezoelectric material is considered in parallel to the inherent capacitance C_P. However, the leakage resistance is normally two orders of magnitude higher than the impedance obtained without taking it into account. Therefore, the effect of the leakage resistance on the overall impedance is neglected in the electrical circuit [11], [43]-[45].

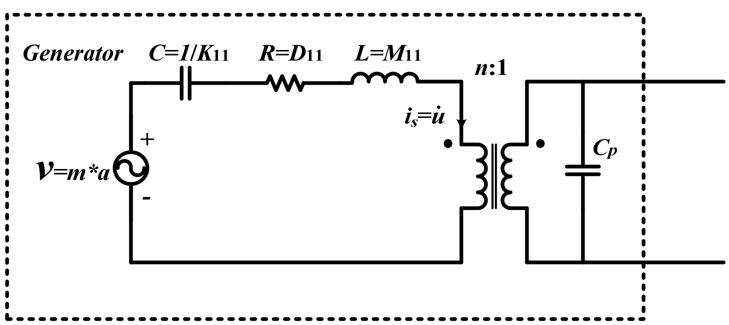

Figure 3.3 The equivalent circuit for the first mode piezoelectric generator.

The open-circuit natural resonance frequency ω_{oc} of a piezoelectric generator is the frequency which makes the output voltage maximum as the load resistance tends to be infinity (open-circuit condition). In contrast, the short-circuit resonance frequency ω_{sc}

is one that makes the output current maximum as the load resistance tends to be zero (short-circuit condition). In other words, the open-circuit resonance frequency corresponds to the frequency where the resistance component of the impedance is the maximum. Likewise the short-circuit resonance frequency corresponds to the frequency where the conductance component of the admittance is the maximum. From Figure 3.3, the short-circuit and open-circuit resonance frequency can be readily obtained as

$$\omega_{sc} = \frac{1}{\sqrt{LC}} \tag{3.11}$$

$$\omega_{oc} = \frac{1}{\sqrt{L\left(\dfrac{C\dfrac{C_P}{n^2}}{C+\dfrac{C_P}{n^2}}\right)}} = \frac{1}{\sqrt{L\left(\dfrac{CC_P}{n^2C+C_P}\right)}} = \sqrt{\frac{1+\dfrac{n^2C}{C_P}}{LC}} = \omega_{sc}\sqrt{1+\frac{n^2C}{C_P}} \tag{3.12}$$

Equ (3.12) and (3.11) are in consistence with the definition of short- and open-circuit resonance frequency in (2.5) and (2.6).

The piezoelectric generator can be represented as Norton or Thévenin equivalent circuits shown in Figure 3.4. To calculate the internal impedance Z_S of the generator, we can replace the current source with open circuit and the voltage source with short circuit. The internal impedance Z_S of the generator then can be represented as shown in Figure 3.5, where

$$L_S = \frac{L}{n^2} = \frac{M_{11}}{n^2};\ R_S = \frac{R}{n^2} = \frac{D_{11}}{n^2};\ C_{S1} = n^2C = \frac{n^2}{K_{11}};\ C_{S2} = C_P \tag{3.13}$$

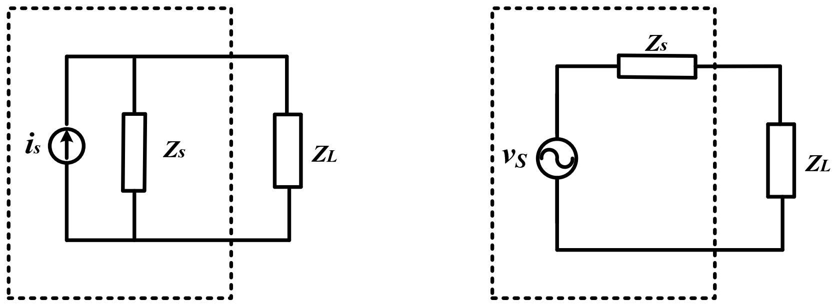

(a) (b)

Figure 3.4 The simplified generator model: (a) Norton equivalent; (b) Thévenin equivalent.

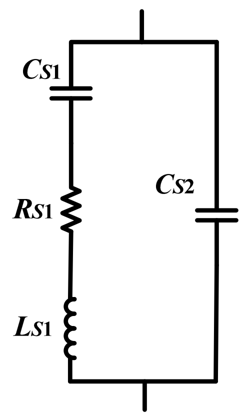

Figure 3.5 Equivalent internal impedance Z_S of a piezoelectric generator.

The internal impedance then can be derived:

$$Z_S = \frac{1}{\dfrac{1}{\dfrac{1}{j\omega C_{S1}} + R_{S1} + j\omega L_{S1}} + j\omega C_{S2}} = R_S + jX_S \tag{3.14}$$

The current source i_S in Figure 3.4(a) is the short-circuit output current given in (3.15), and the voltage source v_S in Figure 3.4(b) is the open-circuit output voltage given in (3.16).

$$i_S = \frac{nv}{\frac{1}{j\omega C} + R + j\omega L} \tag{3.15}$$

$$v_S = \frac{\frac{nv}{j\omega C_P}}{\frac{1}{j\omega C} + R + j\omega L + \frac{n^2}{j\omega C_P}} \tag{3.16}$$

Then, substituting (3.14) and (3.15) into (3.3) and (3.9), we are able to calculate the maximum power output for conjugate impedance matching and resistive impedance matching and find out the optimal load according to (3.2) and (3.8).

3.2.2 Case Study

3.2.2.1 Modal Parameters and Source Impedance

The bimorph piezoelectric generator used in [45] is presented here as an example, whose properties are listed in Table 3.1. The impedance and admittance curves are plotted in Figure 3.6. The open-circuit resonance frequency is 48.2 Hz in Figure 3.6(a). The short-circuit resonance frequency is 45.7 Hz in Figure 3.6 (b).

Table 3.1 Modal parameters of the bimorph piezoelectric harvester.

$M_{11}(\text{kg})$	$D_{11}(\text{kg/s})$	$K_{11}(\text{kg/s}^2)$	$n(\text{kg}/(\text{s}^2\text{V}))$	$C_P(\text{F})$	$m^*(\text{kg})$
1	15.50671	82461.67	0.01964044	41.24e-9	0.1286161

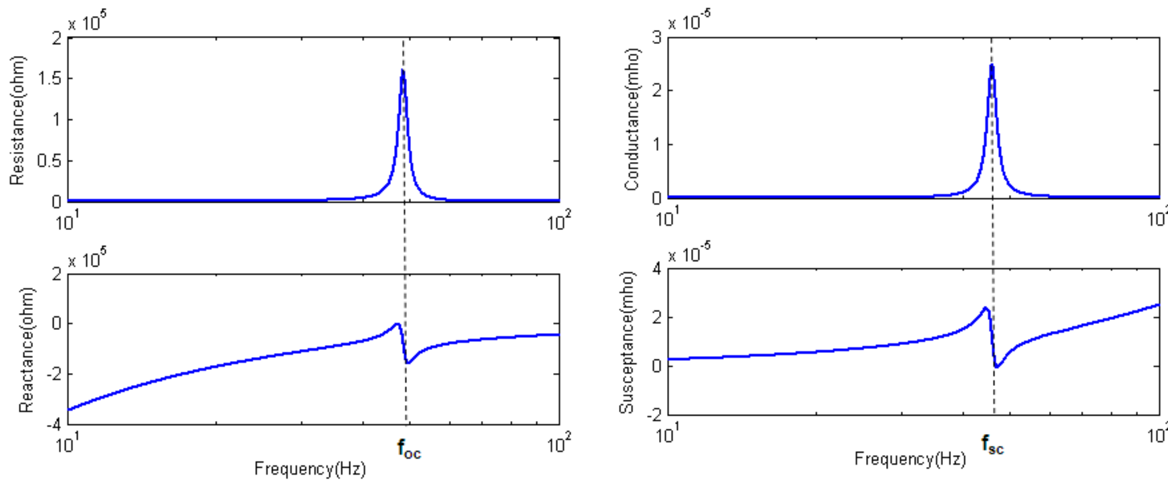

(a) Impedance **(b) Admittance**

Figure 3.6 Source impedance and admittance of a bimorph piezoelectric harvester.

3.2.2.2 Conjugate Matching and Resistive Matching

From Figure 3.6(a), the source impedance is purely resistive around 47 Hz, where resistive matching can be used to extract maximum power. The source can be approximated as a series of a resistor and a capacitor at other frequencies, and a series of a resistor and an inductor can match the source as shown in Figure 3.7.

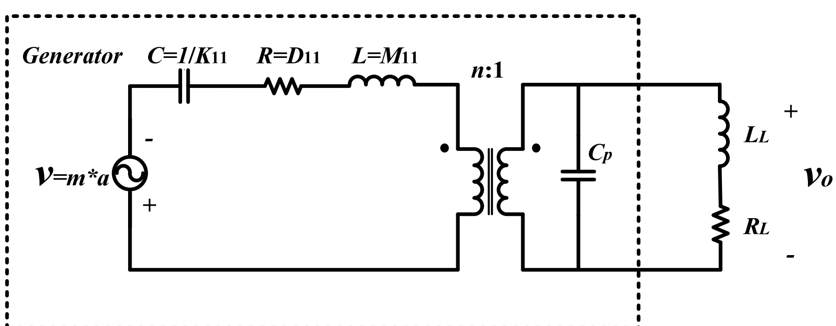

Figure 3.7 Piezoelectric generator connected with a matching load.

For the specific generator under a constant base acceleration level 0.5g (rms), the matching load impedances for different vibration frequencies are tuned through circuit simulation. The average power P_o dissipated by the resistor can be obtained and tabulated in Table 3.2. The output power for resistive matching is also plotted in Figure 3.8, compared along with the theoretical value through calculation discussed in Chapter 3.1. The matched results shown in Figure 3.8 verify the derivation of output power by resistive impedance matching.

Table 3.2 Simulation results with matching load impedance.

Frequency (Hz)	$V_{oc,peak}$ (V)	Conjugate Matching R_L (kohm)	Conjugate Matching L_L (H)	Conjugate Matching P_o (mW)	Resistive Matching R_L (kohm)	Resistive Matching P_o (mW)
44.0	26.6	13.9	137.6	6.40	40.6	3.24
45.0	33.5	22.5	90.8	6.40	34.3	5.00
45.7	41.3	32.8	54.2	6.40	36.2	6.04
46.0	45.1	39.4	37.2	6.40	41.1	6.29
47.0	65.2	83.2	0	6.40	83.2	6.40
48.0	89.0	157.2	191.4	6.40	164.2	6.23
48.2	90.3	159.4	254.5	6.40	177.1	6.05
49.0	75.7	106.5	486.2	6.40	185.2	4.81
50.0	50.1	50.7	469.8	6.40	155.2	3.10

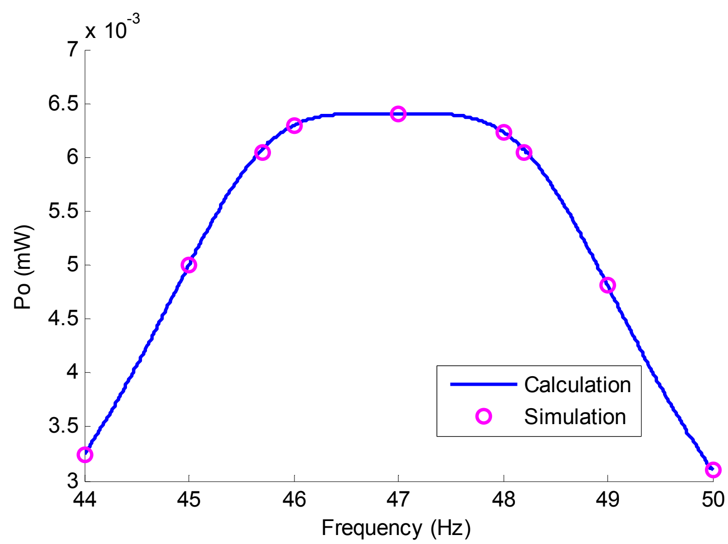

Figure 3.8 Power output with matched resistive load from theoretical calculation and circuit simulation.

As can be seen from the Table 3.2, under the same base acceleration level, the theoretical maximum power delivered from a given piezoelectric power generator to the conjugate matching load is constant with respect to different base vibration frequencies. It can be easily deduced from (3.5) that the maximum power depends only on the source voltage and the internal resistance. The theoretical maximum power delivered from a given piezoelectric generator is computed as

$$P_{o,\max} = \frac{V^2}{4R} = \frac{\left(m^* a_{rms}\right)^2}{4D_{11}} = \frac{\left(0.1286161 \times 0.5 \times 9.8\right)^2}{4 \times 15.5061} = 6.4 \text{ mW} \tag{3.17}$$

Therefore, to increase the output power, the generator should be designed to have less mechanical damping D_{11} or smaller internal resistance R in Figure 3.3. As long as the operation does not cause any damage, large base accelerations and large effective mass m^* (which will result in large effective forcing) are preferable to harvest larger power.

Table 3.2 shows that the complex conjugate matching requires tens of or even several hundreds of henries inductance, even around the generator's resonance frequency, which makes the conjugate impedance matching impractical. When a resistive impedance matching is employed, the output power can only be a fraction of the theoretical maximum power. The power harvesting efficiency is around 75 percent between the short-circuit and the open-circuit resonance frequencies. However, the efficiency drops off sharply outside the frequency range.

3.2.2.3 Effect of Piezoelectric Coupling and Mechanical Damping on Output Power

In order to study the effect of piezoelectric coupling and mechanical damping on the output power, we keep other modal parameters unchanged and calculate the output power with resistive matching load under different piezoelectric coupling coefficient n and different mechanical damping D_{11}. The results are plotted in Figure 3.9 and Figure 3.10. The output power is normalized to the theoretical maximum power output with conjugate matched load.

In Figure 3.9, as piezoelectric coupling increases from small magnitude, the power obtained by the matched resistive load gets closer to the theoretical maximum. If the piezoelectric coupling is higher than 0.2 kg/(s^2V) for the particular cantilever, the maximum power obtained by matched resistive load can reach the theoretical maximum value obtained by the conjugate matched load. If the piezoelectric coupling is further increased, there will be two peaks of power corresponding to short-circuit and open-circuit resonance. As piezoelectric coupling increasing, the two peaks will further apart, which can be foreseen from (3.12).

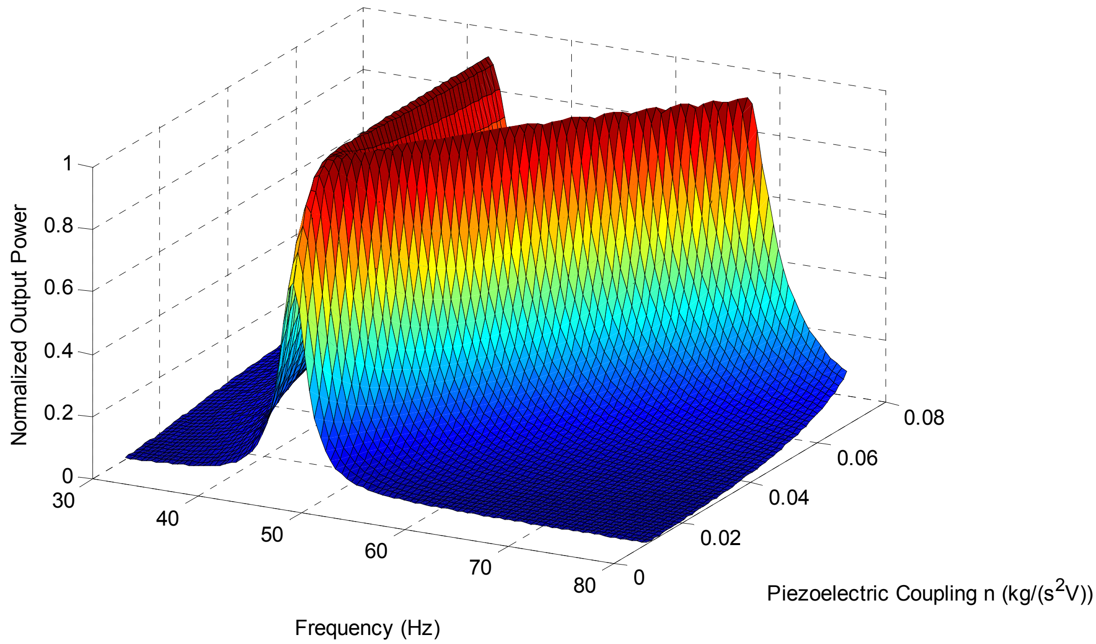

Figure 3.9 Normalized power output with matched resistive load under different piezoelectric coupling.

In Figure 3.10, as mechanical damping decreases from high magnitude, the power obtained by the matched resistive load gets closer to the theoretical maximum. If the mechanical damping is lower than 18 kg/s for the particular cantilever, the maximum power obtained by matched resistive load can reach the theoretical maximum value obtained by the conjugate matched load. If the mechanical damping is further decreased, there will be two peaks of power corresponding to short-circuit and open-circuit resonance. If the mechanical damping is smaller than 1.55 kg/s for the particular cantilever, the ratio of power harvested by resistive matching to the power harvested by conjugate matching will decrease.

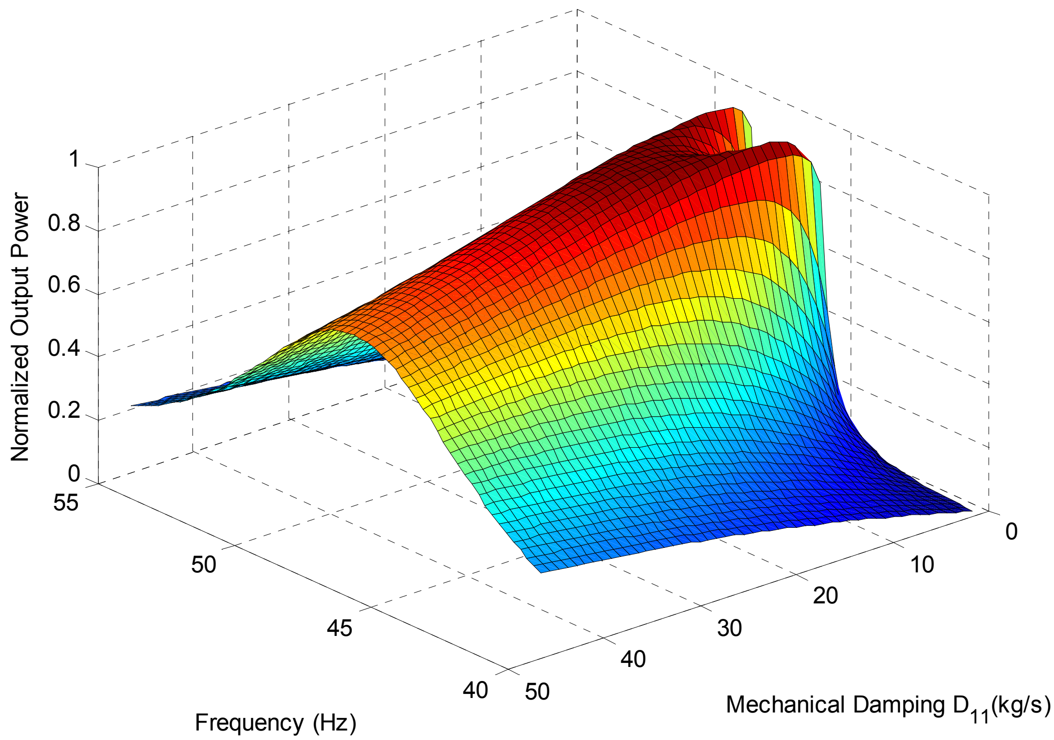

Figure 3.10 Normalized power output with matched resistive load under different mechanical damping.

From the above analysis, it can be noticed that if the piezoelectric cantilever is well designed, resistive matching has as good performance as conjugate matching around resonance frequency. There are also some techniques for extending the bandwidth [62]. Therefore, the resistive impedance matching is an acceptable compromise, provided that the resonance frequency band of the harvester is tuned to the excitation frequency. In the following, we propose a circuit with adjustable input impedance to realize resistive impedance matching.

3.3 Proposed Resistive Impedance Matching Circuit

3.3.1 Circuit Operation

As described in the above section, resistive matching can be quite effective between the short-circuit and the open-circuit resonance frequencies of a generator. Hence, if the load resistance value can be changed adaptively to match the source impedance, high power extraction efficiency can be achieved in the short-to-open resonance frequency band.

Some traditional DC-DC converters, such as buck-boost, flyback, and Sepic converters operating in DCM mode behave as a resistor [53]. More importantly, these converters are able to step up or step down the input voltage to desired output voltage, so it can be applied for a wide range of energy harvesters. A buck-boost converter requires a smaller number of components compared with flyback and Sepic converters and hence less complex. Ref [34] first proposed to use DCM buck-boost converter functioning as a matched resistance. In order to reduce the power consumption of the control circuit, a low-power crystal clock with a fixed duty cycle and a fixed frequency was used in [33] to drive the power switch for their circuit. Unfortunately, it makes the circuit less flexible for various piezoelectric generators.

In this section, a DCM buck-boost converter based conditioning circuit is proposed to achieve the resistive matching. The proposed circuit consists of a buck-boost converter running in DCM directly preceded by a rectifier is shown in **Error! Reference ource not found.**. Different from previous approaches, the big smoothing capacitor right after the rectifier, i.e. C_{rect} in Figure 2.13 and Figure 2.14 is not necessary and therefore eliminated; a low-power oscillator circuit is built to drive the power switch. The duty cycle and the frequency of the oscillator can be adjusted in a wider range than the crystal clock by adjusting the RC network around the comparator to match the source impedance.

To proof the resistive impedance matching ability, the proposed conditioning circuit is run in open-loop mode and the low-power closed-loop circuit and system design is developed later in Chapter 4.

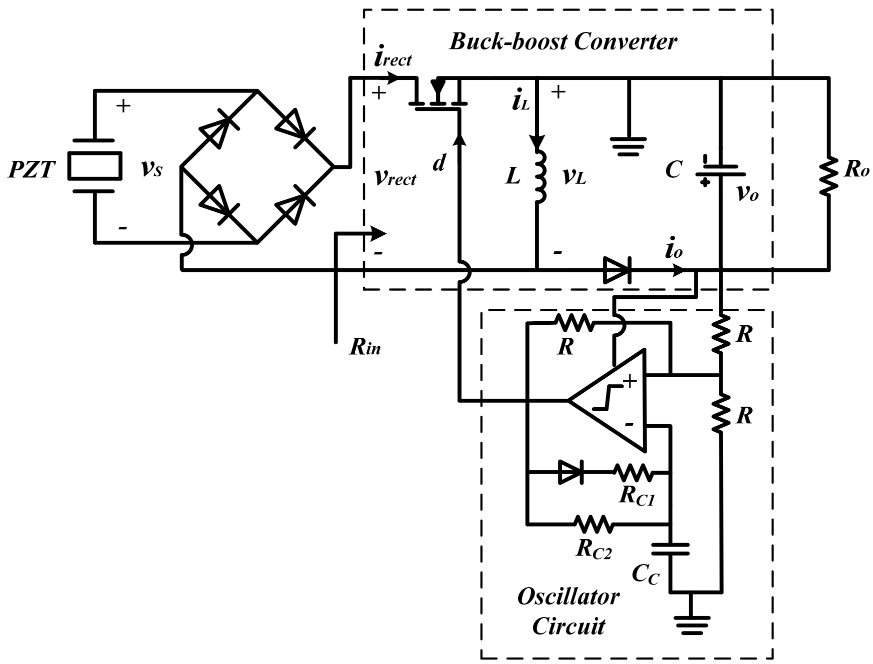

Figure 3.11 Proposed open-loop resistive impedance matching circuit.

3.3.1.1 Operation of DCM Buck-Boost Converter

The voltage and current waveforms of the DCM buck-boost converter during half cycle of a harmonic base vibration are shown in Figure 3.12. Since the base vibration frequency is much slower than the designed switching frequency F_S, the rectified voltage or the input voltage of the buck-boost converter can be treated as DC during a switching period T_S. The voltage and current waveforms during one switching period are shown in Figure 3.13.

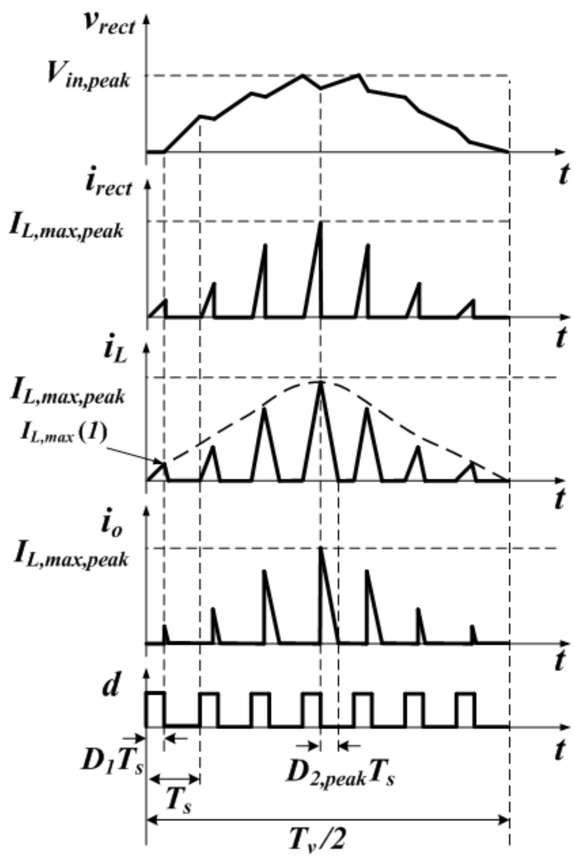

Figure 3.12 Waveforms during half cycle of a harmonic base vibration.

For simplicity, the power switch, diodes and LC filters are assumed to be lossless. The derivation considering the losses in the electrical components is presented later in this section. The effective input resistance of a DCM buck-boost converter is given by [53] as

$$R_{in} = \frac{v_{rect}}{\frac{1}{T_S}\int_0^{D_1T_S} i_L\,dt} = \frac{v_{rect}}{\frac{1}{T_S}\int_0^{D_1T_S} \frac{v_{rect}}{L} t\,dt} = \frac{v_{rect}}{\frac{1}{T_S}\frac{v_{rect}}{L}\frac{\left(D_1T_S\right)^2}{2}} = \frac{2L}{D_1^2T_s} \qquad (3.18)$$

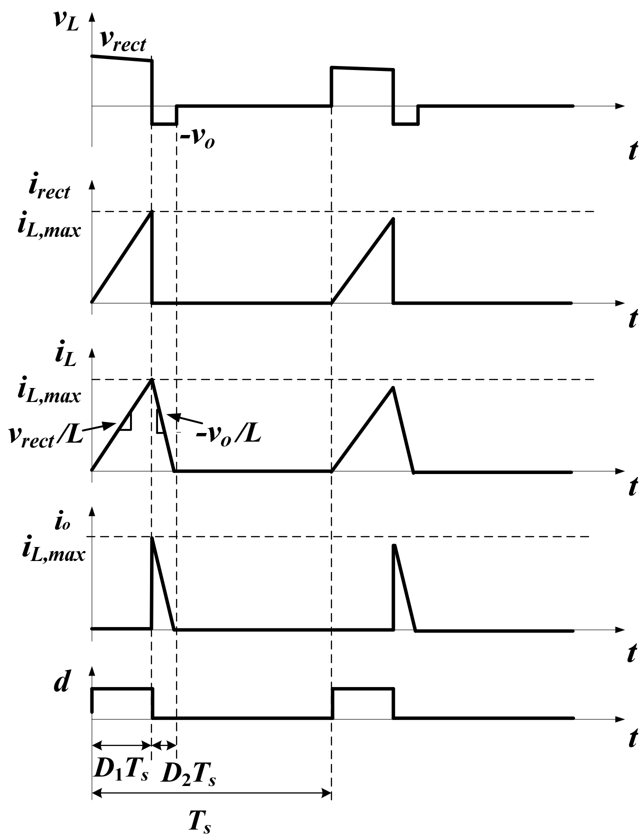

Figure 3.13 Waveforms during one switching period.

In order to achieve the resistive impedance matching, the effective input resistance R_{in} should be equal to the optimal resistive load $R_{in,opt}$ given in (3.8). Hence, the optimal duty cycle can be expressed as

$$D_{1,opt} = \sqrt{\frac{2L}{R_{in,opt} T_s}} \tag{3.19}$$

When the losses of the electrical components are considered, the switch current or the inductor current waveform during the switch on-time (0~$D_1 T_S$) in Figure 3.13 is not a straight line with a slope of v_{rect}/L, but can be described as

$$L\frac{di_L}{dt} = v_{rect} - i_L\left(R_{dson} + R_{dcr}\right) \text{ for } 0 \le t \le D_1 T_S \tag{3.20}$$

where R_{dson} is the resistance of MOSFET during on-time and R_{dcr} is the parasitic resistance of the inductor. It can be readily obtained that

$$i_L = \frac{v_{rect}}{R_{dson} + R_{dcr}}\left[1 - \exp\left(-\frac{R_{dson} + R_{dcr}}{L}t\right)\right] \text{ for } 0 \le t \le D_1 T_S. \tag{3.21}$$

Then the effective input resistance of the buck-boost converter becomes

$$\begin{aligned} R_{in} &= \frac{v_{rect}}{\frac{1}{T_S}\int_0^{D_1 T_S} i_L\,dt} \\ &= \frac{v_{rect}}{\frac{1}{T_S}\int_0^{D_1 T_S}\frac{v_{rect}}{R_{dson} + R_{dcr}}\left[1 - \exp\left(-\frac{R_{dson} + R_{dcr}}{L}t\right)\right]dt} \\ &= \frac{T_S\left(R_{dson} + R_{dcr}\right)}{D_1 T_S + \frac{L}{R_{dson} + R_{dcr}}\left[\exp\left(-\frac{R_{dson} + R_{dcr}}{L}D_1 T_S\right) - 1\right]} \end{aligned} \tag{3.22}$$

where the optimal value of D_1 to achieve a matched input resistance can be computed numerically. The equation can be further simplified by using Taylor series expansion of the exponential function, i.e. $\exp(x) \approx 1 + x + x^2/2$ for $|x| << 1$. Therefore, (3.22) can be reduced to

$$R_{in} \approx \frac{T_S\left(R_{dson} + R_{dcr}\right)}{D_1 T_S + \frac{L}{R_{dson} + R_{dcr}}\left(\frac{R_{dson} + R_{dcr}}{L}D_1 T_S + \frac{\left(\left(R_{dson} + R_{dcr}\right)D_1 T_S\right)^2}{2L^2}\right)} = \frac{2L}{D_1^2 T_S} \tag{3.23}$$

Here, the third and higher order terms of the Taylor series are neglected provided

$$\frac{R_{dson} + R_{dcr}}{L} D_1 T_S << 1 \tag{3.24}$$

Note that (3.23) and (3.18) are identical. By substituting (3.19) into (3.24), we obtain (3.25), which is the assumption of (3.23) in practice:

$$\left(R_{dson} + R_{dcr}\right)\sqrt{\frac{2T_S}{R_{in,opt} L}} << 1 \tag{3.25}$$

It should also be noticed that v_{rect} is canceled out in (3.22), i.e. the input impedance of the DCM buck-boost converter is not a function of the input voltage. Therefore, even though there is a finite voltage drop on the conducting diodes of the rectifier, it will not affect the impedance matching between the piezoelectric generator and the interface circuit. Other losses such as the voltage drop of conducting diode connected to the output capacitor and the parasitic resistance of output capacitance will not affect the impedance matching either.

In summary, if the circuit parameters satisfy the inequality given by (3.25), the duty cycle D_1 of the power switch can be simply calculated using (3.19). However, if the inequality given by (3.25) cannot be satisfied, the duty cycle D_1 should be solved from (3.22). Using (3.19) will result in impedance mismatch as well as power losses.

3.3.1.2 Operation of Low-Power Oscillator Circuit

From (3.19), once the inductance value and the switching frequency are chosen, the duty cycle for the maximum output power can be obtained. In the proposed circuit, a low-power comparator with an RC network is used to generate the gate signal driving the power switch. The duty cycle and switching frequency can be tuned by the R_{C1}, R_{C2} and C_C [16] in Error! Reference source not found.. The voltage waveforms of the comparator's output nd two input nodes are shown in Figure 3.14.

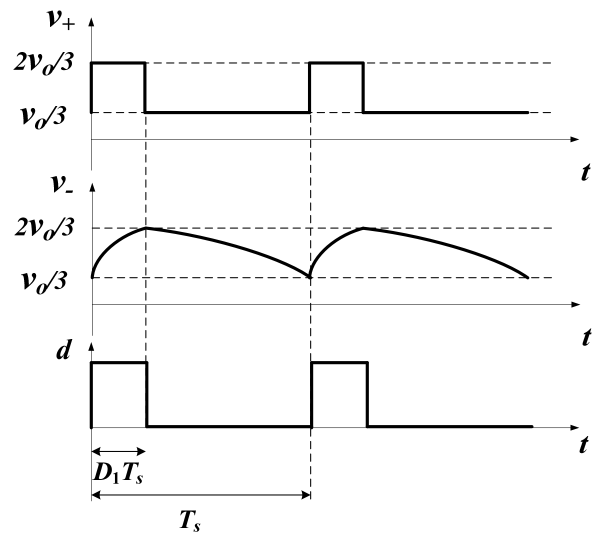

Figure 3.14 Waveforms of the output and two input nodes of the comparator.

If the comparator output is high, i.e. equal to the supply voltage (v_o in the proposed circuit in **Error! Reference source not found.**), the voltage at the non-nverting input of the comparator is 2/3 of the supply voltage. Capacitor C_C is charged through parallel R_{C1} and R_{C2}. Once the capacitor voltage reaches 2/3 of the supply voltage, the comparator output goes low, i.e. the ground voltage. The voltage at the non-inverting input of comparator is now 1/3 of the supply voltage. Capacitor C_C is discharged through R_{C2}. Once the capacitor voltage reaches 1/3 of the supply voltage, the comparator output becomes high and the entire cycle repeats. If R_{C2} is chosen to be much larger than R_{C1}, the duty cycle and its frequency are approximately as follows

$$D_1 \approx \frac{R_{C1}}{R_{C2}} \tag{3.26}$$

$$F_S \approx \frac{1}{(R_{C1} + R_{C2})C_C \ln 2} \tag{3.27}$$

3.3.2 Experimental Results

To verify the feasibility of the proposed resistive impedance matching circuit, experiments were performed using a cantilevered bimorph generator with a tip mass. The experimental setup is shown in Figure 3.15. The bimorph (manufactured by Piezo Systems, Inc. with model number T226-A4-503X) consists of two oppositely poled PZT-5A piezoelectric elements bracketing a brass substructure layer, and the two piezoelectric elements are connected in series.

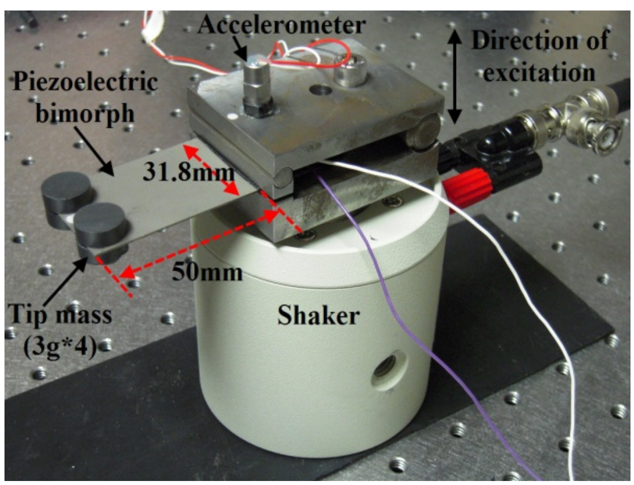

Figure 3.15 Cantilevered bimorph generator.

The electromechanical frequency response functions (FRFs) that relate the tip velocity to the base acceleration were measured to obtain the short-circuit and open-circuit resonance frequencies of the cantilevered bimorph generator, and the measurement results are shown in Figure 3.16. The short-circuit and open-circuit resonance frequencies are 53.0 Hz and 56.1 Hz, respectively. The external load resistance was tuned based on real power output to find the optimal resistive load of the piezoelectric energy harvester around the resonance frequency, and the result is shown in Figure 3.17. The optimal resistive load is in the range of 20 kΩ to 120 kΩ.

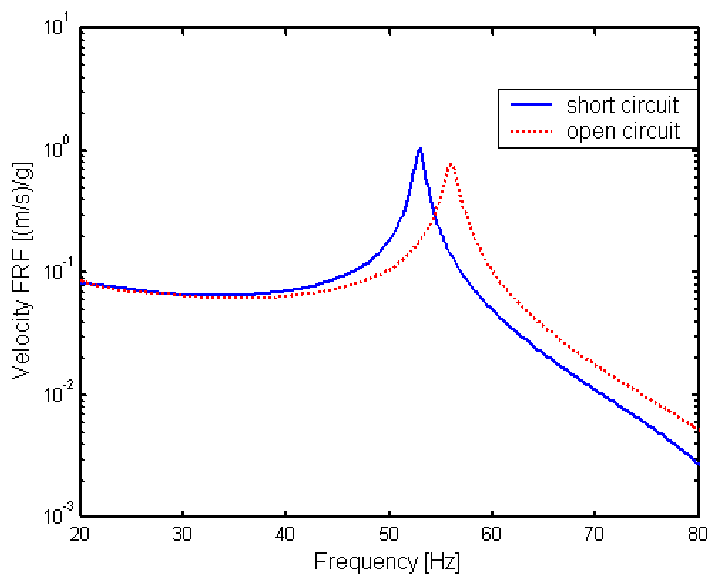

Figure 3.16 Short-circuit and open-circuit velocity FRFs of the energy harvester.

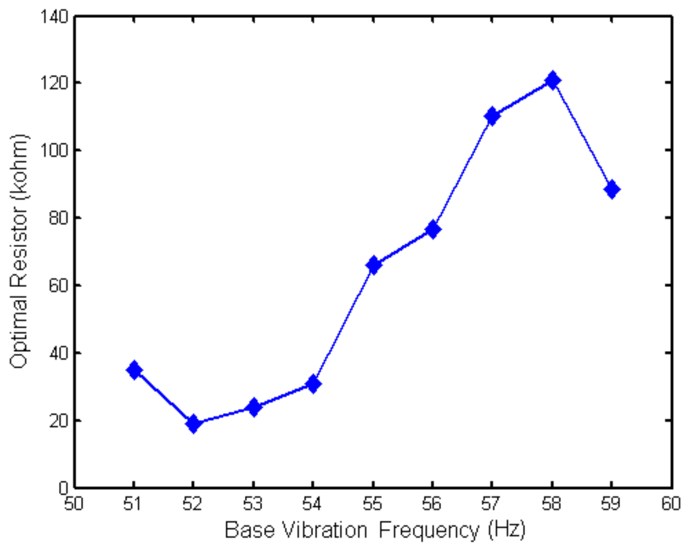

Figure 3.17 Optimal resistance versus excitation frequency.

The next step is to decide the component values of the buck-boost converter and circuit parameters including the switching frequency. A lower switching frequency should be much higher than the base vibration frequency to manipulate the shape of the generator's voltage output; on the other side, a higher switching frequency causes higher switching loss on the power switch and the diode. We chose the switching frequency of 1 kHz, around 20 times of the excitation frequency, which is not necessary optimal, but sufficient for a proof of the concept. A larger inductor causes smaller current ripple and therefore smaller rms current and conduction loss. However, a larger inductor is bulkier and has larger parasitic resistance to result in higher conduction loss. We chose a 1-mH inductor. Other components were selected based on the voltage and current stresses. For the experiment, the harvester is designed to be excited under the rms acceleration amplitude of 0.5 g. The voltage and current stresses are around 30 V and 200 mA, respectively. The components used in the experiment are listed in Table 3.3.

Table 3.3 Components used in the proposed circuit.

Component	Part Number	Notes
Rectifier	BAS3007	V_F = 0.35 V@ 100 mA.
MOSFET	2N7002	R_{dson} = 1.7 Ω; C_{iss} = 20 pF, C_{oss} = 11 pF.
Schottky Diode	PMEG4005	V_F = 0.295 V@ 10 mA.
Inductor	SL2125-102K1R3	L = 1.0 mH; DCR = 0.35 Ω.
Supercapacitor	GW209F	C = 0.12 F; ESR = 70 mΩ.
Comparator	TLV3419	I_q = 0.85 μA @ 5V

The duty cycle and the switching frequency were tuned by choosing appropriate R_{C1}, R_{C2} and C_C to achieve the maximum power delivery. The optimal duty cycle values around the resonance frequency tuned in the experiment are shown in Figure 3.18 against the expected values from (3.19). The experimental results closely match the theoretical trend and the optimal value. The average power harvested by the proposed circuit is plotted in Figure 3.19 along with the average power harvested directly by the optimal resistive load (shown in Figure 3.17).

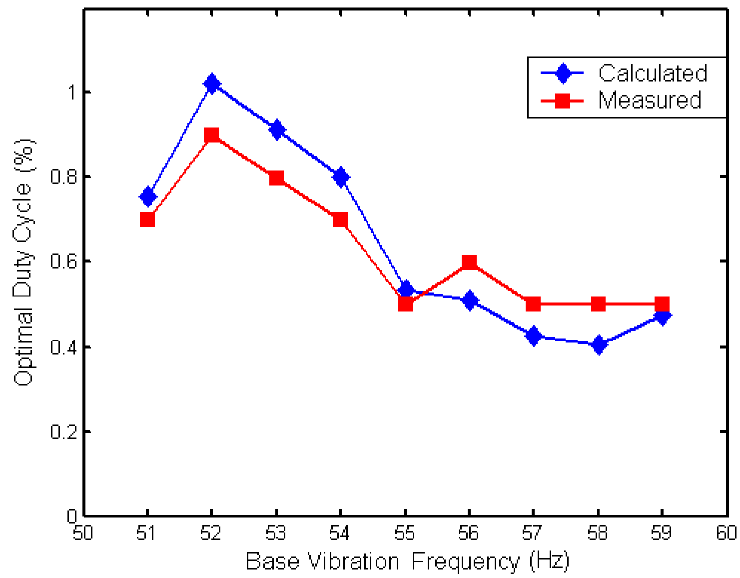

Figure 3.18 The optimal duty cycle of the proposed circuit versus excitation frequency.

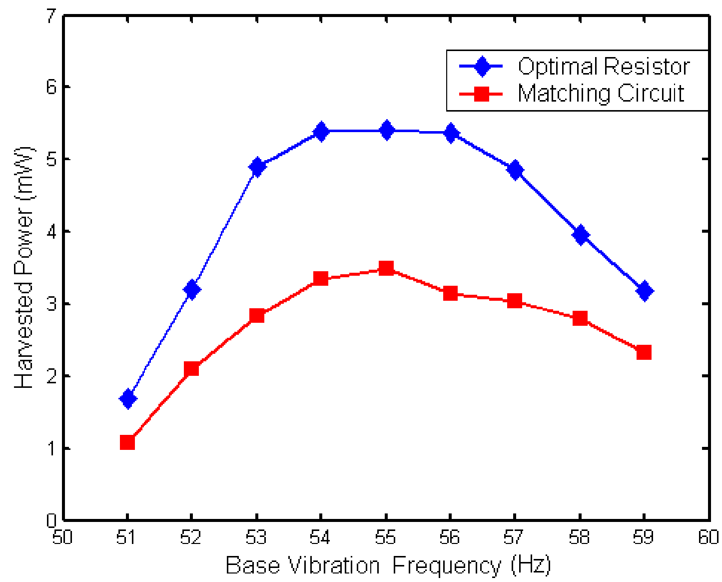

Figure 3.19 Harvested power by the optimal resistive load and the proposed circuit.

The power harvested by the proposed circuit is in the range of 1.0 mW to 3.5 mW around the resonance frequency for an rms base acceleration amplitude of 0.5 g.

According to Figure 3.19, the overall power harvesting efficiency of the proposed circuit is 58 percent to 72 percent of the available power extracted by the optimal resistive loads.

3.4 Summary

In this chapter, we propose to view the circuit design problem from impedance matching perspective. By applying Norton or Thévenin theorem to the equivalent circuit model of piezoelectric cantilevers, we are able to easily calculate the maximum power output for conjugate impedance matching and resistive impedance matching and find out the optimal load. Simulation results show that resistive matching could be an acceptable compromise for conditioning circuit design when the vibration frequency is around the resonance frequency band of the piezoelectric power generator. Therefore, a two-stage conditioning circuit with a rectifier and a DCM buck-boost converter is proposed to achieve the resistive impedance matching. Experimental results are presented to validate the effectiveness of the resistive impedance matching circuit.

Chapter 4:
Low-power Circuit and System Design

In the previous chapter, the resistive impedance matching circuit is run at open-loop condition. However, the vibration frequency and amplitude of host structure may change, additional control circuit is necessary to dynamically adjust the operation of the circuit through controlling the duty cycle of the main switch to match the variable source impedance. However, on the other side, the power overhead caused by the controller has to be minimized to gain more power for the whole system. To allow a dynamic tuning of the impedance of interface circuit, a MCU based digital controller is applied to build a self-powered closed-loop energy harvesting system in this chapter. The proposed system adopts dynamic resistive matching and is able to cold start without relying on a backup battery. Several low-power design schemes to reduce power dissipation of the proposed system are described, and sources of power loss are analyzed to improve the power efficiency. Experimental results show that the efficiency is comparable to the previous approach without closed-loop control.

This chapter is organized as follows. Chapter 4.1 presents overview of the proposed system and its operation. Chapter 4.2 describes the low-power design schemes employed for our system. Chapter 4.3 analyzes sources of power loss and Chapter 4.4 presents efficiency metrics. The start-up strategy is proposed in Chapter 4.5. Chapter 4.6 presents experimental results including the system performance and a breakdown of the power loss.

4.1 System Diagram and Operation

Figure 4.1 shows the diagram of the proposed system, which intends to illustrate the system operation instead of the actual implementation. The derivative of a buck-boost converter, flyback converter, is adopted for our system owing to the non-inverting output voltage and the relative low circuit complexity. A 5-V supercapacitor is chosen as the energy storage device due to its virtually unlimited life cycles and simple charge mechanism. Linear Regulator 1 and the oscillator in Figure 4.1 are responsible for the start-up. A low-power MCU MSP430 from Texas Instruments implements a maximum power point tracking (MPPT) algorithm. Linear Regulator 2 regulates the supercapacitor's voltage to 3 V to power up the MCU.

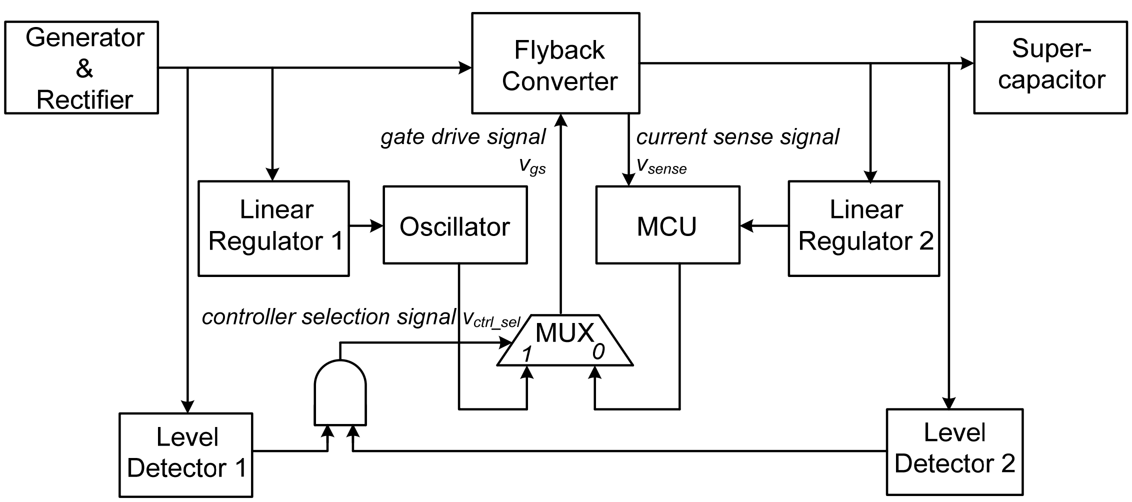

Figure 4.1 Diagram of the proposed system.

The piezoelectric generator for our experiment is shown in Figure 4.2, which has four bimorph cantilevers connected in parallel, which is T226-A4-503X from Piezo Systems, Inc., the same patch used in Chapter 3. Two 4-gram magnets attached to the tip of each cantilever increase the effective mass and enable us to tune the resonant frequency of the beam. The resonant frequencies of each cantilever are tuned to be the same, at around 47 Hz.

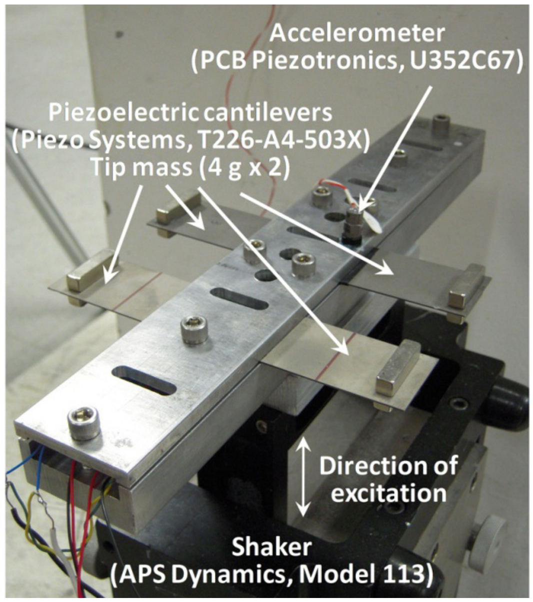

Figure 4.2 The piezoelectric generator for our experiment.

By connecting different load resistors to the output of rectifier, the optimal resistive load around the resonant frequency was identified by tuning the load manually to find the maximum power output. The optimal resistor ranges from 10 kΩ to 50 kΩ as shown in Figure 4.3. The MPPT executed by the MCU is designed to tune the operation of the flyback converter so that the equivalent input resistance is equal to the optimal value.

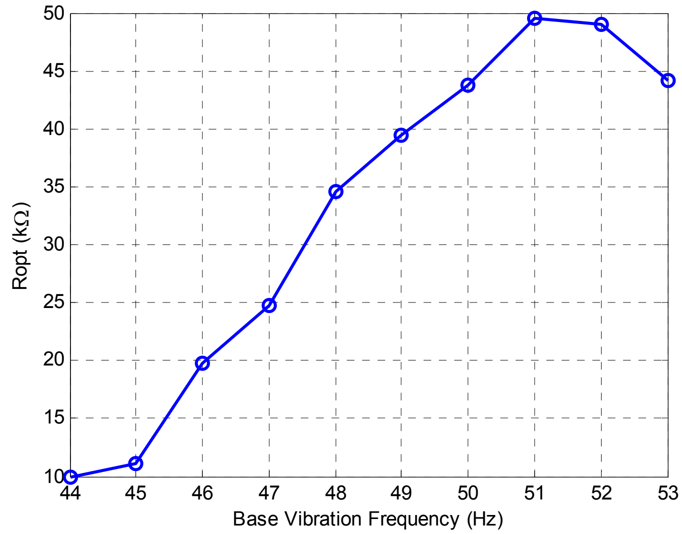

Figure 4.3 Measured optimal load resistance.

4.2 Low-power Design Schemes

Low power dissipation is the key design objective for the proposed system. All design choices including the circuit topology are made judiciously to reduce the overall power dissipation without an excessive sacrifice on the performance. A few major design choices are described in the following.

4.2.1 DCM Flyback Converter

As mentioned in the Chapter 3, the buck-boost type converter is able to handle a wide range of the input voltage, below or above the output voltage. DCM buck-boost converter behaves as a lossless resistor [53]. These two features make the buck-boost converter a popular choice for piezoelectric energy harvesting [33]-[35]. To apply an MPPT algorithm, a controller needs to know the average harvested power, which typically requires sensing both the voltage and the current. However, the power information of a DCM buck-boost converter can be obtained by sensing only the inductor current, which saves power associated with the sensing. The feature is analyzed in detail as follows.

The derivative of a buck-boost converter, flyback converter, is adopted for our system owing to the non-inverting output voltage and the relative low circuit complexity. The circuit diagram of a flyback converter is shown in Figure 4.4, and the voltage and current waveforms are shown in Figure 4.5. For simplicity, the MOSFET, diode, and transformer are assumed lossless, and detailed loss analysis is given in Chapter 4.3. Magnetizing inductance, $L_{m,}$ functions in the same manner as the inductor in a traditional buck-boost converter. The magnetizing current for one switching cycle is obtained as follows.

$$i_{Lm}(t)=\begin{cases} \dfrac{v_{rect}}{L_m}t, \quad 0<t\le d_1T_s \\ \dfrac{V_{rect}d_1T_s}{L_m}-\dfrac{n_Tv_o}{L_m}(t-d_1T_s), \quad d_1T_s<t\le(d_1+d_2)T_s \\ 0, \quad (d_1+d_2)T_s<t\le T_s \end{cases} \tag{4.1}$$

The effective input resistance R_{in} of the flyback converter is obtained as (4.2) [53]. The input resistance is a function of the duty cycle d_1 and the switching period T_s, or the switch on-time, rather than the input or output voltages of the converter.

$$R_{in}=\frac{v_{rect}}{\dfrac{1}{T_S}\int_0^{d_1T_S}i_{Lm}dt}=\frac{v_{rect}}{\dfrac{1}{T_S}\int_0^{d_1T_S}\dfrac{v_{rect}}{L_m}tdt}=\frac{2L_m}{d_1^2T_s}=\frac{2L_mT_s}{T_{on}^2} \tag{4.2}$$

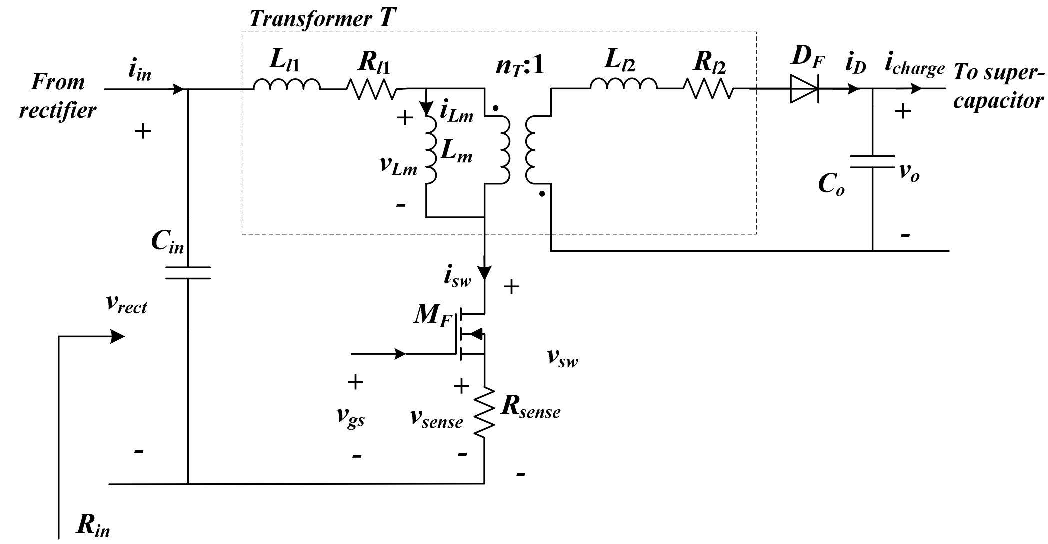

Figure 4.4 Circuit diagram of the flyback converter.

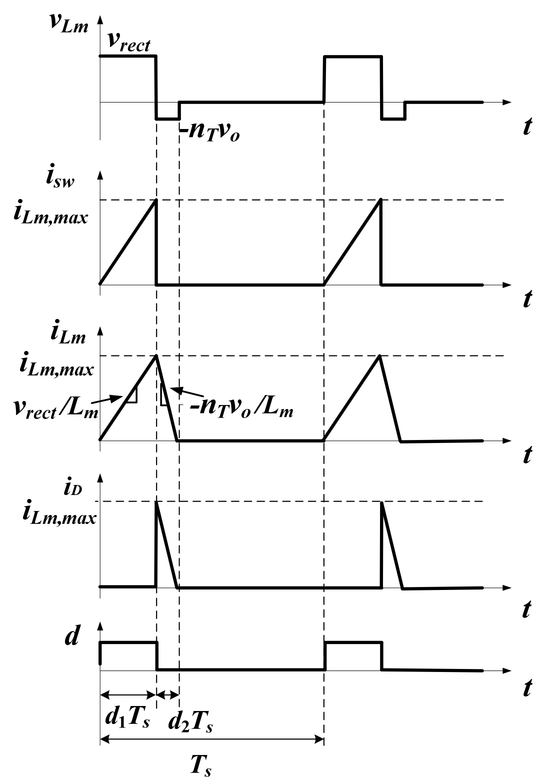

Figure 4.5 Waveforms in a switching cycle of the flyback converter.

The inductor current reaches its peak, $i_{Lm,max,}$ at the end of each switch on-time and releases the inductor energy completely to the load during the switch off-time due to the DCM operation. The average power delivered to the load for each switching cycle can be expressed as in (4.3).

$$P_{avg} = \frac{L_m i_{Lm,\max}^2}{2T_s} \tag{4.3}$$

Therefore, by sensing only the inductor current through the sensing resistor R_{sense} in Figure 4.4, the controller is able to compute the average power delivered to the converter, which simplifies the sensing circuit and the MPPT algorithm to save power.

4.2.2 Constant On-time Modulation

Power consumption of the controller for our system is mainly due to the dynamic power dissipation of the MCU, which is proportional to the MCU clock frequency. The clock frequency is determined by the resolution of the duty cycle that the system is required to achieve [63]. In order to realize MPPT (which implements the hill-climbing algorithm [64], [65]) for the proposed system, it adjusts the duty cycle, which in turn changes the input resistance of the converter. Therefore, the required resolution of the input resistance determines the clock frequency of the MCU. The resolution of the input resistance for the constant frequency modulation and the constant on-time modulations are given below.

$$\Delta R_{in\_constFs} = \frac{2L_m T_s}{T_{on}^2} - \frac{2L_m T_s}{\left(T_{on} + \Delta T_{on}\right)^2} \approx \frac{4L_m T_s \Delta T_{on}}{T_{on}^3} = \frac{2L_m}{T_{on}^2} \cdot \frac{2}{d_1} \cdot \Delta T_{on} \qquad (4.4)$$

$$\Delta R_{in\_constTon} = \frac{2L_m T_s}{T_{on}^2} - \frac{2L_m\left(T_s - \Delta T_{off}\right)}{T_{on}^2} = \frac{2L_m}{T_{on}^2} \cdot \Delta T_{off} \qquad (4.5)$$

The above expressions reveal that, to achieve the same resolution, the constant frequency modulation requires $\frac{2}{d_1}$ times higher clock frequency than the constant on-time modulation. Figure 4.6 shows the minimum clock frequency versus the resolution of the input resistance for the circuit used for our experiments (to be given in Chapter 4.6), whose parameters are T_{on} = 10 μs, L_m = 10 mH, n_T = 1, and $R_{in,opt}$ = 10 - 50 kΩ. The required clock frequency for the constant on-time modulation is reduced by a factor of 10 - 50 times compared to the constant frequency modulation, which in turn reduces the power consumption of the MCU.

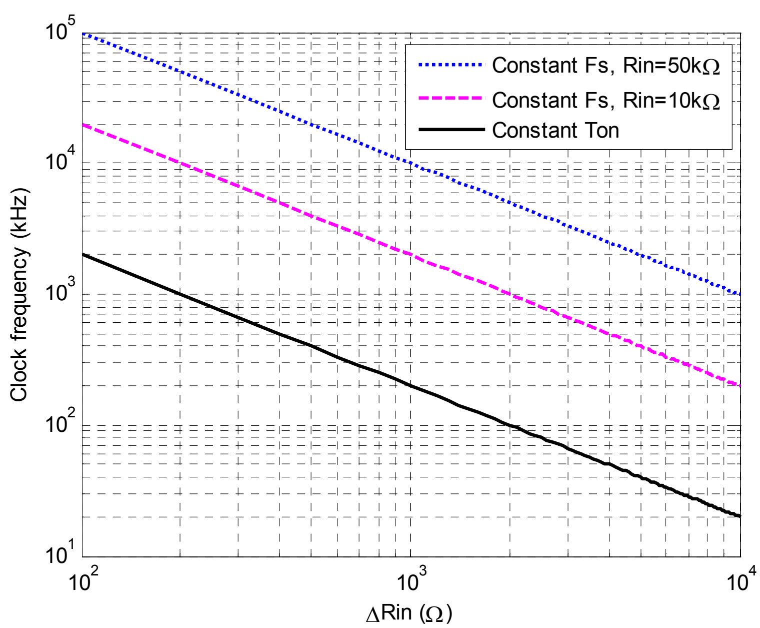

Figure 4.6 Minimum clock frequency versus resolution of the input resistance (Constant Fs: constant frequency modulation, Constant Ton: constant on-time modulation).

Under the constant on-time modulation, flow-chart of the hill-climbing MPPT algorithm is shown in Figure 4.7. The current switching period is decreased with a predetermined step. The inductor current is sampled at the middle of the switch on-time (to avoid the noisy peak current), and the controller calculates the average power using (4). If the average input power increases, the switching period is decreased again with the same predetermined step size; otherwise the switching period is increased by the same step size. The hill-climbing process continues to settle around the optimal switching period.

4.2.3 Switch of the MCU Clock Frequency

Since environmental conditions such as temperature and vibration frequency change relatively slow compared with the processor speed, the MPPT algorithm is performed periodically to save power. For the proposed system, the MCU executes the MPPT algorithm for 20 ms at 8-MHz clock frequency and is in sleep mode at 1-MHz clock frequency for the following 2 s. The MCU maintains the current duty cycle in the sleep mode. Figure 4.8 shows the current profile of the MCU with the supply voltage of 3 V. It consumes 7.8 mW (with its current 2.6 mA) in the active mode and 330 μW (with its current 110 μA) during the sleep mode, which results in the average MCU power of 408 μW during the operation.

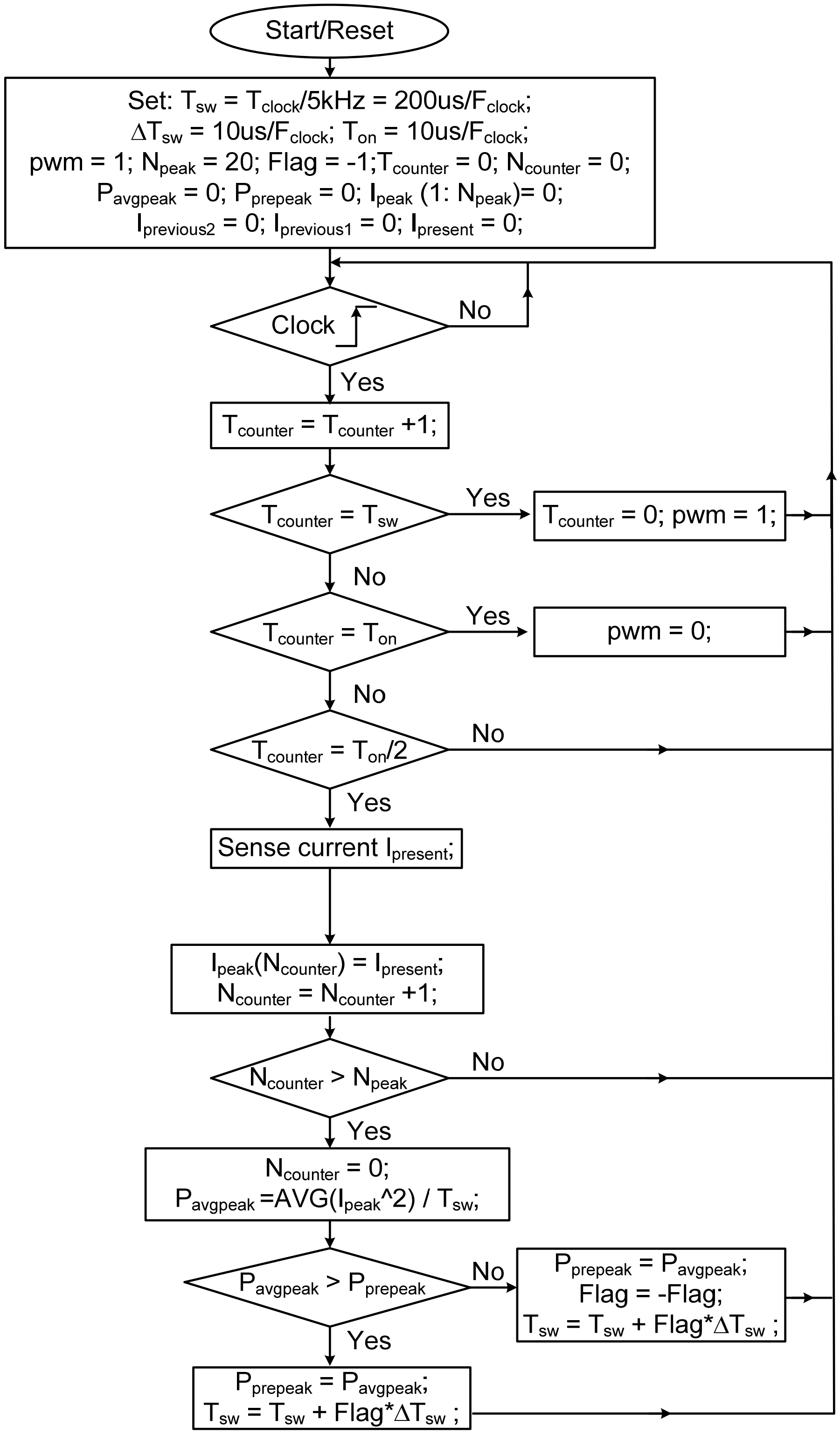

Figure 4.7 Flow chart of MPPT algorithm.

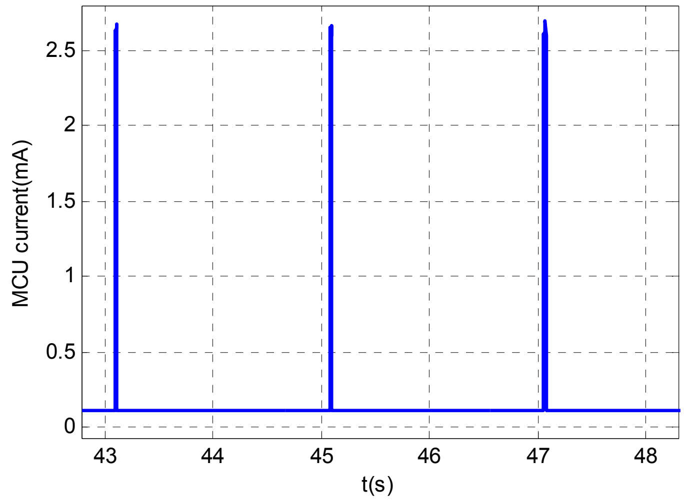

(a) Normal view

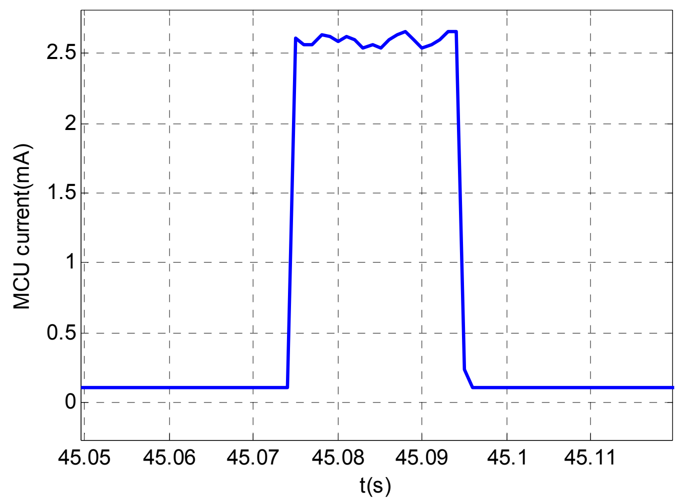

(b) Close-up view

Figure 4.8 Current profile of the MCU.

4.3 Loss Breakdown

We analyze the sources of power dissipation for the flyback converter, in order to select adequate circuit components and improve the efficiency. We assume the converter runs at a steady state, in which the resistive matching has already been achieved. Under this assumption, the major power loss is due to power dissipation of four components –

MOSFET M_F, transformer T, diode D_F, and sensing resistor R_{sense}. Refer to Figure 4.4 and Figure 4.5 for notations used for the expressions given below.

- MOSFET M_F

The loss associated with MOSFET M_F is mainly the conduction loss and switching loss. The conduction loss is due to the channel on-resistance $R_{ds,on}$ and occurs during the switch on-time. It can be obtained as:

$$P_{MOSFET,cond} = \frac{1}{T_s}\int_0^{d_1 T_s} i_{Lm}^2 R_{ds,on} dt = \frac{1}{T_s}\int_0^{d_1 T_s} \left(\frac{i_{Lm,\max}}{d_1 T_s} t\right)^2 R_{ds,on} dt = \frac{1}{3}\left(i_{Lm,\max}\right)^2 d_1 R_{ds,on} \tag{4.6}$$

where the maximum inductor $i_{Lm,max}$ is approximately

$$i_{Lm,\max} = \frac{V_{rect} T_{on}}{L_m} \tag{4.7}$$

Substituting (4.2) and (4.7) into (4.6) leads to

$$P_{MOSFET,cond} = \frac{2 V_{rect}^2 T_{on} R_{ds,on}}{3 L_m R_{in,opt}} \tag{4.8}$$

It indicates that a small T_{on}, a small $R_{ds,on}$, and a large L_m reduce the conduction loss.

The switching loss is due to the voltage-current overlap during the turn-off transition and the loss on output capacitance during the turn-on transition.

$$\begin{aligned} P_{MOSFET,switch} &= \left(\frac{1}{2}\left(V_{rect} + n_T V_o\right) i_{Lm,\max} t_f + \frac{1}{2} C_{oss}\left(V_{rect} + n_T V_o\right)^2\right) F_s \\ &= \left(\left(V_{rect} + n_T V_o\right)\frac{V_{rect} T_{on}}{L_m} t_f + C_{oss}\left(V_{rect} + n_T V_o\right)^2\right)\frac{L_m}{T_{on}^2 R_{in,opt}} \end{aligned} \tag{4.9}$$

where F_s is the switching frequency, t_f is the falling time of the gate input signal, and C_{oss} denotes the output capacitance of the MOSFET. It indicates that a small C_{oss}, and n_T reduce the switching loss.

- Transformer T

The loss associated with the transformer is mainly due to the parasitic resistance R_{l1} and R_{l2} of the copper wires. It can be obtained as

$$P_{transforme\ r} = \frac{1}{T_s}\left[\int_0^{d_1 T_s} i_{Lm}^2 R_{l1} dt + \int_{d_1 T_s}^{T_s} (n_T i_{Lm})^2 R_{l2} dt\right] = \frac{1}{3}(i_{Lm,\max})^2 \left(d_1 R_{l1} + d_2 n_T^2 R_{l2}\right) \quad (4.10)$$

where d_2 is approximately

$$d_2 = \frac{d_1 V_{rect}}{n_T V_o} \quad (4.11)$$

Substituting (4.2) and (4.11) into (4.10) leads to

$$P_{transformer} = \frac{2V_{rect}^2 T_{on}}{3L_m R_{in,opt}}\left(R_{l1} + \frac{n_T V_{rect}}{V_o} R_{l2}\right) \quad (4.12)$$

Small T_{on}, n_T, R_{l1}, and R_{l2} and a large L_m reduce the loss associated with the transformer. Note that the choice of T_{on}, n_T and L_m values should guarantee the DCM operation or meet $d_1 + d_2 < 1$.

- Diode D_F

The first-order forward voltage drop of the diode is expressed as v_F = ki_L + b, where i_L is the forward current, k and b are constants, and the power loss of a diode is $v_F i_{Lm}$. The current flows through the diode only during the switch off-time. The average conduction loss of the diode is obtained as

$$\begin{aligned}
P_{diode,cond} &= \frac{1}{T_s}\int_0^{d_2T_s}\left(k\left(\frac{n_T i_{Lm,\max}}{d_2T_s}t\right)+b\right)\left(\frac{n_T i_{Lm,\max}}{d_2T_s}t\right)dt \\
&= d_2\left(\frac{k}{3}\left(n_T i_{Lm,\max}\right)^2+\frac{b}{2}n_T i_{Lm,\max}\right) \\
&= \frac{2kn_T V_{rect}^3 T_{on}}{3V_o L_m R_{in,opt}}+\frac{bV_{rect}^2}{V_o R_{in,opt}}
\end{aligned} \quad (4.13)$$

Small values of k, b, n_T and T_{on} and large L_m reduce the diode conduction loss. Note that high performance diodes have small k and b values.

The switching loss of the diode is only the loss on its junction capacitance during its turn-on transition.

$$P_{diode,swtch} = \frac{1}{2}C_j\left(V_o+V_{rect}/n_T\right)^2 F_s = \frac{1}{2}C_j\left(V_o+V_{rect}/n_T\right)^2\frac{2L_m}{T_{on}^2 R_{in,opt}} \quad (4.14)$$

where C_j is diode capacitance. Small values of C_j, L_m and large T_{on}, n_T reduce the diode switching loss.

- Sensing resistor R_{sense}

Power loss due to the sensing resistor is similar to $R_{ds,on}$ of the MOSFET:

$$P_{Rsense} = \frac{1}{3}\left(i_{Lm,\max}\right)^2 d_1 R_{sense} = \frac{2V_{rect}^2 T_{on} R_{sense}}{3L_m R_{in,opt}} \quad (4.15)$$

Small T_{on} and R_{sense} and a large L_m reduce the power loss. However, small R_{sense} increases noise during the current sensing, which degrades the performance of the MPPT operation. Further, the range of the voltage drop across R_{sense} is also imposed by the ADC.

4.4 Metrics of Efficiency

We define the overall system efficiency $\eta_{overall}$ as the ratio of the harvested power P_{out} on the supercapacitor to the power P_{max} dissipated by a perfectly matched load directly connected at the rectifier output of the piezoelectric generator (equivalently at the input of the flyback converter). The overall system efficiency is formally expressed as follows.

$$\eta_{overall} = \frac{P_{out}}{P_{max}} \tag{4.16}$$

Two sources contribute to the overall system efficiency. One source is the impedance matching performance called MPPT efficiency in this paper, and the other one is the power conversion performance in the flyback converter called conversion efficiency. The MPPT efficiency η_{MPPT} is defined as the ratio of the power P_{in} flowing into the flyback converter to the power harvested by the optimal resistor, and the conversion efficiency $\eta_{conversion}$ is the ratio of the harvested power P_{out} on the supercapacitor to the power P_{in} flowing into the flyback converter. They are defined formally as below.

$$\eta_{MPPT} = \frac{P_{in}}{P_{max}} \tag{4.17}$$

$$\eta_{conversion} = \frac{P_{out}}{P_{in}} \tag{4.18}$$

Note that the overall system efficiency is the product of the two efficiency terms.

4.5 Start-up Strategy

The loading of the MCU is relatively heavy to the piezoelectric generator, which only generates several milliwatts. Connection of the MCU to the source changes the input impedance of the converter and complicates the impedance matching mechanism. Therefore, the MCU should be powered by the output voltage of the converter (or the supercapacitor). Then, the problem is to start-up the MCU when the energy stored on the supercapacitor is completely drained. A low-power oscillator directly powered by the source is proposed to solve the problem, and the system starts as follows. Suppose that the supercapacitor is initially discharged. The piezoelectric generator powers up Linear Regulator 1 in Figure 4.1, which in turn powers up the oscillator. The oscillator generates fixed duty cycle pulses to drive the flyback converter. Note that the oscillator does not perform dynamic resistive matching. When the supercapacitor is sufficiently charged, the MCU takes over the pulse generation and performs dynamic resistive matching, while the oscillator is shut off to save power. Since the average current dissipated by the MCU is approximately an order of magnitude higher than the oscillator, the MCU is active only when the piezoelectric harvester generates sufficient power to benefit from the dynamic resistive matching. More specifically, the MCU operates only when (i) the rectified voltage of the piezoelectric harvester is higher than a threshold voltage level, which is detected by Level Detector 1 in Figure 4.1, and (ii) the output voltage reaches a predetermined level, which is detected by Level Detector 2. The decision to operate the oscillator or MCU is elaborated in the following.

Dynamic resistive matching increases the efficiency at the cost of higher power dissipation of the MCU compared with the oscillator. Therefore, dynamic resistive matching should be performed only when the net power harvested increases. Assume that the source impedance of the piezoelectric harvester is pure resistive and its value R_i is in the range of [R_{smin}, R_{smax}]. The switching frequency and the duty cycle of the oscillator are set accordingly, so that the input resistance of the flyback converter is equal to the mid-point of the two source resistances, i.e.,

$$R_{smid} = \frac{R_{smin} + R_{smax}}{2} \tag{4.19}$$

Noting the input voltage to the flyback converter is V_{rect}, the input power delivered to the flyback converter under the oscillator is

$$P_{in,OSC} = \frac{V_{rect}^2}{R_{smid}} \tag{4.20}$$

Now, consider the input power delivered to the converter under the MCU. Since the current through the input resistance R_{smid} is (V_{rect}/R_{smid}), the source voltage V_s is readily obtained as

$$V_s = \left(\frac{V_{rect}}{R_{smid}}\right)R_i + V_{rect} \tag{4.21}$$

The MCU matches its input resistance to the source resistance R_i, and the power $P_{in,MCU}$ delivered to the flyback converter is obtained as follows.

$$P_{in,MCU} = \frac{1}{4R_i}\left[\left(\frac{V_{rect}}{R_{smid}}\right)R_i + V_{rect}\right]^2 \tag{4.22}$$

Now, let us consider the power dissipation. The oscillator is powered up by the input voltage V_{rect}, while the MCU by the output voltage V_o. (Refer to Figure 4.1 and Figure 4.4.) Hence, the total system loss under the oscillator and under the MCU are given as follows.

$$P_{loss,OSC} = P_{loss,ps}\left(V_{rect}, R_{smid}\right) + V_{rect} I_{OSC} \tag{4.23}$$

$$P_{loss,MCU} = P_{loss,ps}\left(\frac{1}{2}\left[\left(\frac{V_{rect}}{R_{smid}}\right)R_i + V_{rect}\right], R_i\right) + V_o I_{MCU} \tag{4.24}$$

where $P_{loss,ps}$ denotes the power dissipated by the power stage as elaborated in the previous section, which is a function of the converter input voltage and the equivalent input resistance. I_{OSC} and I_{MCU} denote the current through the oscillator and the MCU, respectively. The MCU operates only if the net power harvested is greater than the net power harvested under the oscillator, which is expressed as follows.

$$\left(P_{in,MCU} - P_{loss,MCU}\right) > \left(P_{in,OSC} - P_{loss,OSC}\right) \tag{4.25}$$

If the rectifier output voltage V_{rect} is greater than a predetermined threshold voltage $V_{rect,\,th}$, the above condition can be met.

4.6 Experimental Results

To verify the feasibility and measure the performance of the proposed PM system, we prototyped the system and experimented it with the aforementioned piezoelectric generator. Experimental results are presented in this section.

4.6.1 Prototyping and Experimental Setup

Based on the loss analysis described in the previous section, circuit parameters are judiciously chosen to minimize the loss of components. The circuit parameters for our system are listed in Table II and the prototyped circuit board is shown in Figure 4.9.

Table 4.1 Components and circuit parameters in the prototype.

Component	Part Number	Circuit Parameters
Rectifier	BAS3007	V_F = 0.35 V@ 100 mA.
MOSFET M_F	2N7002	R_{dson} = 1.7 Ω-5.3 Ω, C_{oss}= 15 pF.
Schottky Diode D_F	PMEG4005	V_F = 0.220V@10mA; 0.295V@100mA; C_j = 50 pF
Supercapacitor	GW209F	C = 0.12 F; ESR = 70 mΩ.
Sensing resistor R_{sense}	--	47 Ω
Transformer T	--	L_m = 10mH; n_T =1; R_{l1} = 6Ω, R_{l2} = 6Ω.
Switch on-time T_{on}	--	10 μs

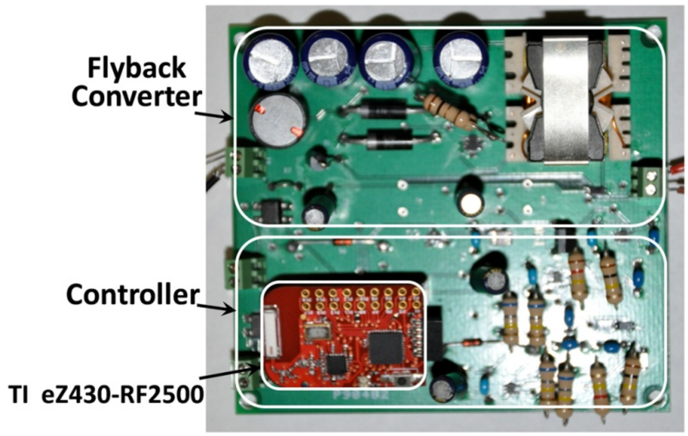

Figure 4.9 Prototype of our system.

4.6.2 Start-up and MPPT

The optimal resistive load ranges from 10 kΩ to 50 kΩ as shown in Figure 4.3. The mid-point value is 30 kΩ, which is the target value set for the oscillator. The average current of the oscillator circuit I_{osc} is measured as 50 μA. According to the start-up strategy described in Chapter 4.5, the potential power output driven by the oscillator and the MCU performing MPPT is calculated and plotted in Figure 4.10. If the voltage after rectifier is higher than 5 V, switching to the MCU generates more power. Therefore, the threshold rectified voltage $V_{rect,\ th}$ is set to 5 V.

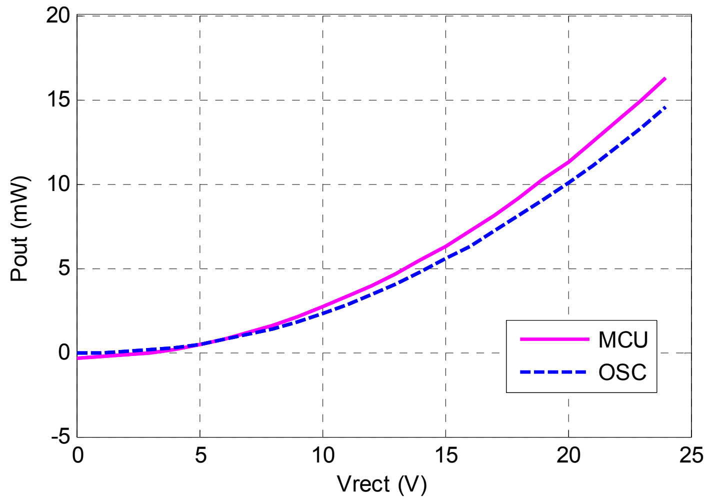

Figure 4.10 Predicted power output of the system under different rectified voltage.

Figure 4.11 shows a transient response during a switch over from the oscillator to the MCU, while the supercapacitor is being charged up. Initially, the input voltage v_{rect} is around 13 V, which is above the threshold voltage $V_{rect,\ th}$ = 5V. When the supercapacitor voltage reaches above 3 V, the MCU takes over the control at 46 second as shown in Figure 4.11(a). The transition from the oscillator to the MCU is also captured by oscilloscope as shown in Figure 4.11(b). To illustrate the transition, the initial off-time generated by the MCU is intentionally configured much higher than that of the oscillator for this experiment. Due to the abrupt increase of the off-time, the rectified voltage v_{rect} increases abruptly, while the input power P_{in} drops accordingly. As the MCU executes the MPPT algorithm, the input power increases steadily and reaches the peak around at 120 second. The rectified voltage decreases accordingly during the period and oscillates as it reaches the steady state.

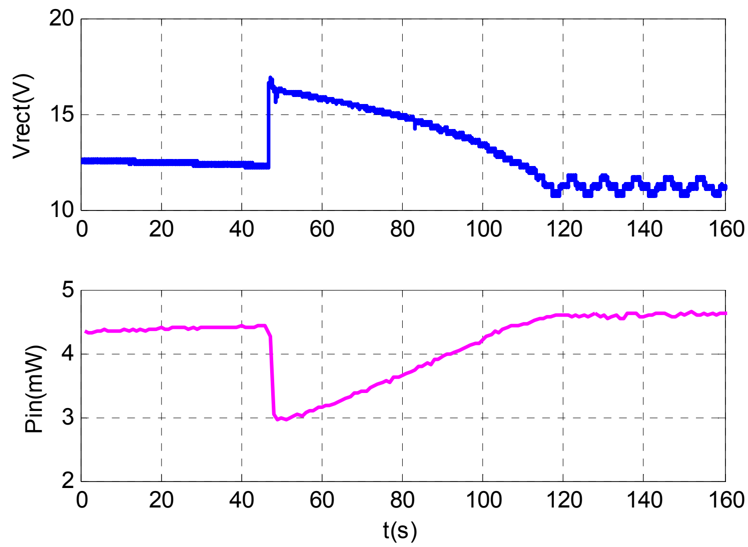

(a)

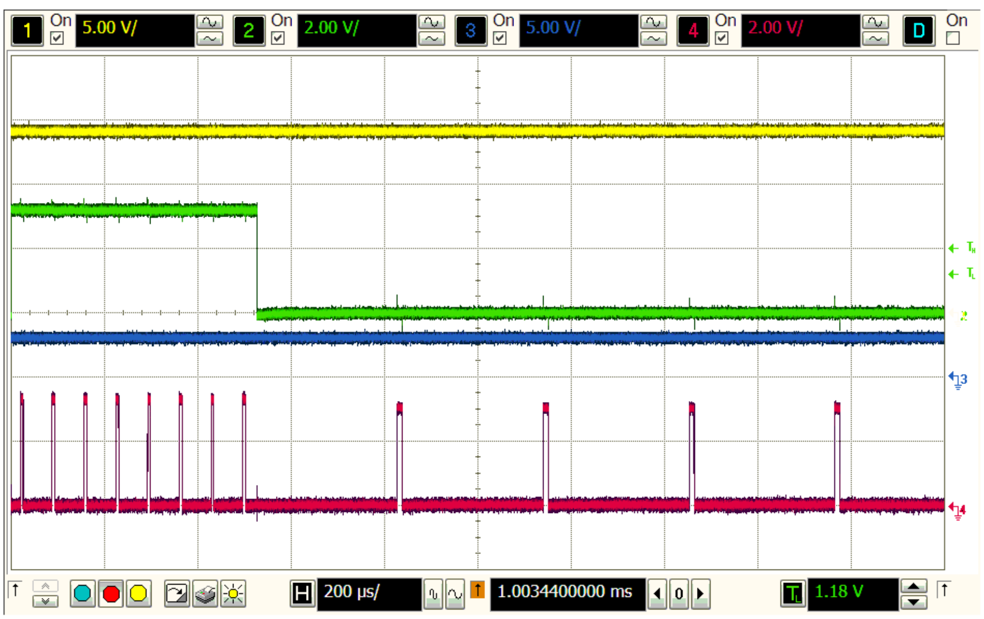

(b)

Figure 4.11 Transient response during the switch over from the oscillator to the MCU (a) rectified voltage V_{rect} and converter input power P_{in}; (b) Ch1: rectified voltage v_{rect}, 5 V/div; Ch2: controller selection signal v_{ctrl_sel}, 2 V/div; Ch3: converter output voltage v_o, 5 V/div; Ch4: gate drive signal v_{gs}, 2 V/div; 200 µs/div.)

Figure 4.12 shows the steady state waveforms of the current sensing signal v_{sense}, switching node voltage v_{sw}, charging current i_{charge} and the gate drive signal v_{gs}. The waveforms in Figure 4.12 match the DCM operation of a flyback converter depicted in Figure 4.5. Note that when the diode current reduces to zero, the switching node voltage (the second one from top) rings due to the oscillation of the magnetizing inductance and the output capacitance of the MOSFET.

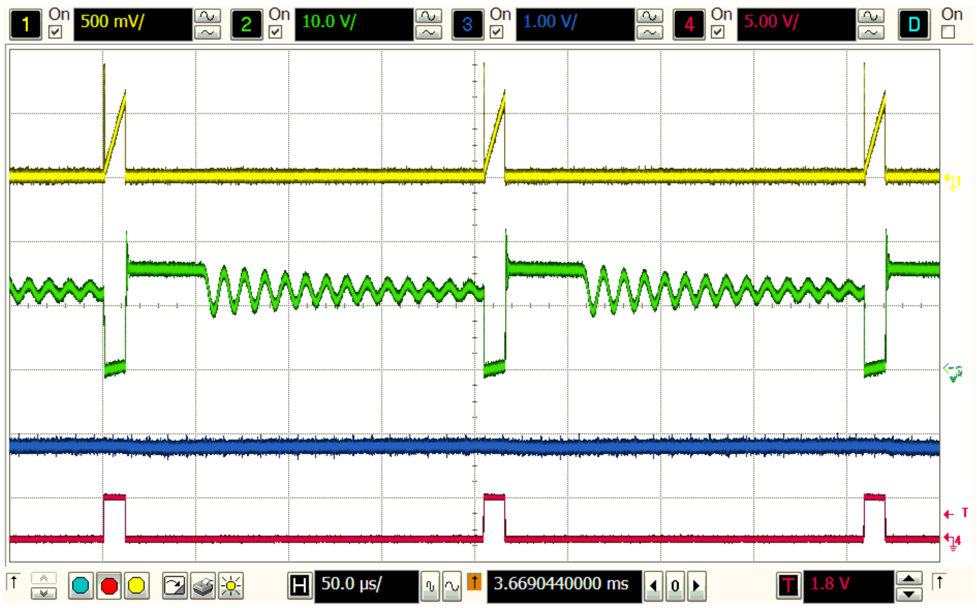

Figure 4.12 The steady state waveforms. (Ch1: current sensing signal v_{sense}, 500 mV/div; Ch2: switching node voltage v_{sw}, 10 V/div; Ch3: charging current i_{charge}, 1 mA/div; Ch4: gate drive signal v_{gs}, 5 V/div; 50 µs/div.)

Next, we examine the performance of the MPPT algorithm executed by the MCU. We measured the on-time of the MOSFET after the flyback converter reached the steady state, and calculated the equivalent input resistance of the converter using (3). The equivalent input resistance was compared with the optimal resistor load obtained manually. Figure 4.13 shows the comparison of the two resistances for the frequency range of interest. The graphs show that the equivalent input resistance obtained by the

MPPT algorithm is ±3 kΩ off the optimal resistor load. So, the MPPT algorithm executed by the MCU achieves good performance.

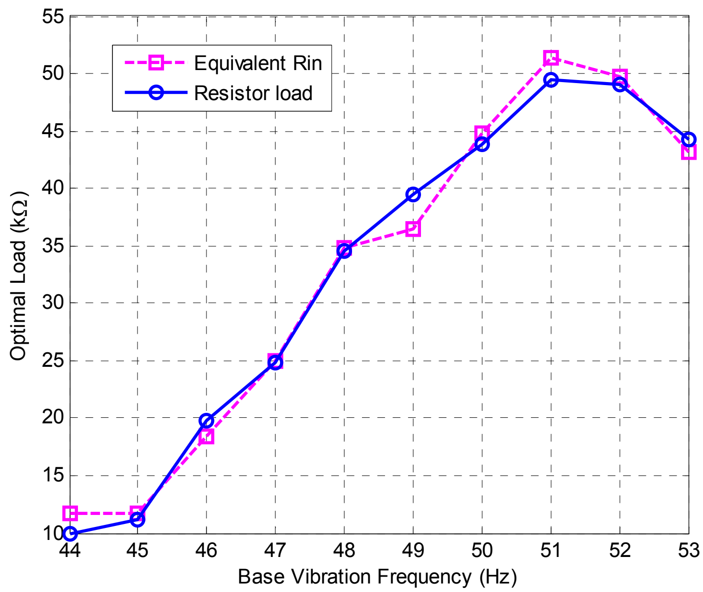

Figure 4.13 Comparison of the equivalent input resistance of the flyback converter obtained through the MPPT and the optimal resistor.

4.6.3 Efficiency

We measured the power output of the proposed PM system and compared it against that obtained by the optimal resistive load under 0.5 g base acceleration. The harvested power P_{out} on the supercapacitor delivered by our system and the maximal power P_{max} delivered to the optimal load are shown in Figure 4.14. The maximal power P_{max} is about 11.9 mW at the resonant frequency of 47 Hz, and the harvested power P_{out} is 8.4 mW yielding the overall system efficiency $\eta_{overall}$ of 70 percent. The maximal power P_{max} decreases rapidly as the vibration frequency moves away from the resonant frequency and hence harvested power P_{out} of the system. The harvested power ranges from 1.4 mW to 8.4 mW for the frequency range of 44 Hz to 53 Hz, and the overall efficiency $\eta_{overall}$ remains from 62 percent to 72 percent.

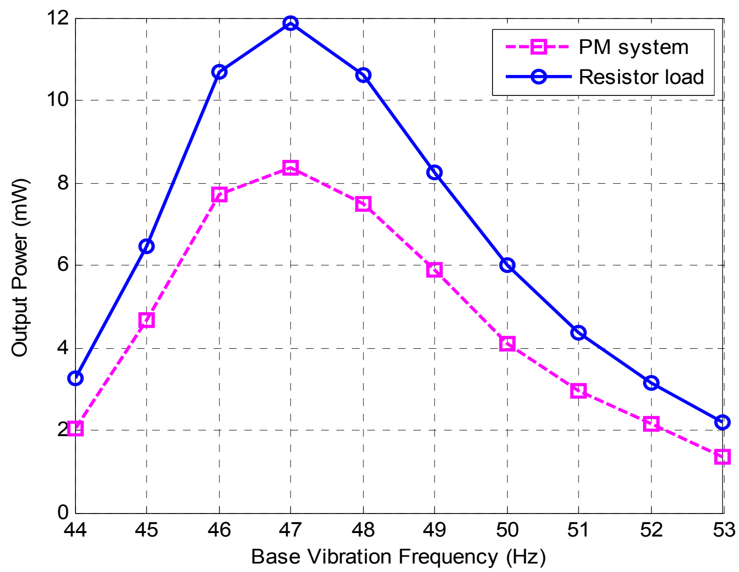

Figure 4.14 Maximal power delivered by the piezoelectric generator and power harvested by the proposed system.

We are interested in the impact of MPPT and the component loss to the overall efficiency, or MPPT efficiency η_{MPPT} and conversion efficiency $\eta_{conversion}$. (Refer to Section III.D for definitions of the efficiency.) The MPPT efficiency, the estimated and measured conversion efficiency, and the overall system efficiency are shown in Figure 4.15. The MPPT efficiency stays above 94 percent for the entire frequency range of interest. High MPPT efficiency is expected, as the equivalent input resistance is close to the optimal one as shown in Figure 4.13. The conversion efficiency stays in the range of 65 percent to 76 percent for the frequency range, and it is clear that the conversion dictates the overall system efficiency. The loss in the flyback converter is a function of the input voltage and input resistance. Substituting the measured input voltage and input resistance, we estimated the loss in the flyback converter, as well as the conversion efficiency. The discrepancy of the estimated efficiency and measured efficiency is less than 5 percent, which is possibly caused by the parasitic in the prototype. It implies that the loss analysis is relatively accurate and the reduction of power loss for components is essential to improve the system performance.

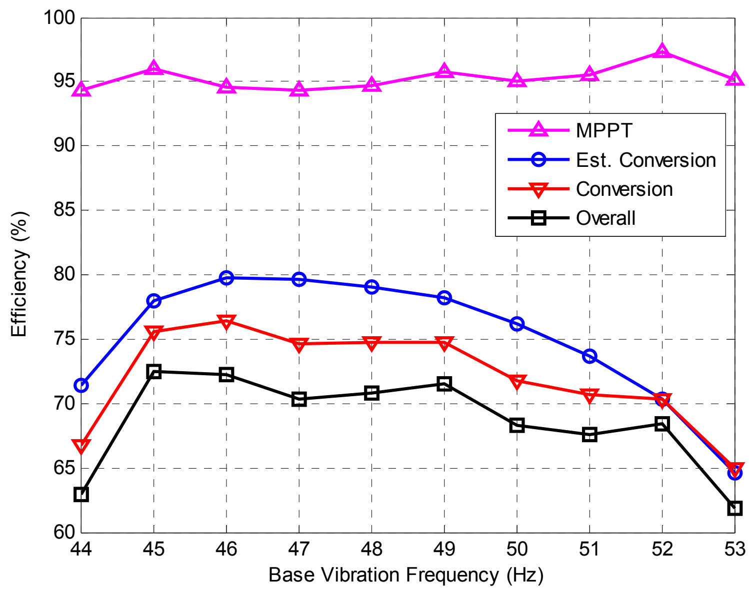

Figure 4.15 The MPPT, conversion and system overall efficiency.

4.6.4 Loss Breakdown

As indicated above, the power loss of the components is the critical factor for the system efficiency. Figure 4.16 shows the loss breakdown at the resonant frequency of 47 Hz. The diode D_F and the controller (specifically the MCU) are the major sources and account for 45 percent and 18 percent of the total power loss, respectively. The power loss of the diode is mostly the conduction loss, and a synchronous rectifier can be used to reduce the conduction loss at the cost of increased circuit complexity. The power consumption of the controller is 408 μW, which is a small fraction compared to the controller in [32], i.e. 5.74 mW. The power dissipation can be further reduced by setting a longer sleep time for the MCU at the cost of lower MPPT tracking speed.

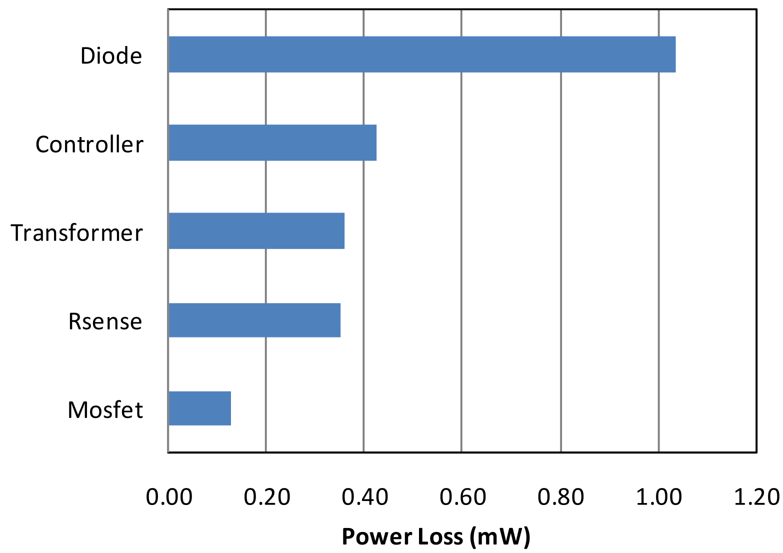

Figure 4.16 Breakdown of the power loss.

4.6.5 Comparison with Other Systems

Although a direct and fair comparison with other competing systems is difficult because of the different target power and operating environments, it may be worth comparing our system with the system reported by Lefeuvre et al. in [33]. Both systems adopt resistive matching and are self-powered, but Lefeuvre's system does not employ dynamic impedance or resistive matching. In spite of the adoption of dynamic resistive matching for our system, both systems achieve similar efficiency of about 70 percent at the same acceleration level. However, as the operating environment changes, it is expected that the efficiency of Lefeuvre's system would decrease rapidly due to the absence of dynamic impedance matching.

4.7 Summary

A low-power design of a piezoelectric energy harvesting system is presented in this Chapter. Several schemes to reduce power dissipation of the system are described, and sources of the power loss are analyzed. The DCM operation of flyback converter is chosen as for MPPT to be implemented with a single current sensor. The constant on-time modulation lowers the clock frequency of the controller by more than an order of magnitude for our system, which reduces the dynamic power dissipation of the controller. MPPT implemented in the MCU, is executed at intermittent time intervals due to a relatively slow change of the operating condition. When MPPT is not active, the MCU operates at a lower clock frequency to save power. A low power oscillator is adopted for our system to address the start-up problem which has not been considered in the open literature for other self-powered systems.

Experimental results indicate that the proposed system harvests up to 8.4 mW of power under 0.5 g base acceleration using four parallel piezoelectric cantilevers and achieves 72 percent efficiency around the resonant frequency of 47 Hz. The sources of the power loss are analyzed to improve the power efficiency, and a breakdown of measured power loss is presented. The diode and the controller (specifically the MCU) are the two major sources for the power loss and account for 63 percent of the total power loss of the system.

A synchronous rectifier can be used to reduce the diode conduction loss at the cost of increased circuit complexity. With a larger number of piezoelectric cantilevers connected or under higher base acceleration, the efficiency of the proposed system will increase since the power dissipation of the controller circuit will not scale up. Further improvement of power efficiency and development of the energy harvesting system in a monolithic IC will be presented in the next chapter. The circuit topology and low-power design schemes adopted for our system can be applied to other energy harvesting systems such as small scale wind turbines and solar panels in a straightforward manner.

Chapter 5:
Power Management IC Design

Power loss analysis for the proposed power management system shows that the conduction loss of the diode and the power dissipation of the controller (specifically the MCU) are two major sources for the power loss. Synchronous rectifiers can be used to reduce the forward voltage drop of diodes. As for the controller, the application-specific integrated circuit (ASIC) is a good alternative to general-purpose MCUs or DSPs. Therefore, in order to further improve the power efficiency, development of the energy harvesting system in a monolithic IC is pursued and presented in this chapter. The power management IC, which is developed in a 0.18-μm CMOS process, adopts a non-inverting buck-boost converter with a closed-loop control. It can accommodate a wide input voltage range under varying environmental conditions. The controller realizes dynamic tracking for maximum power point using a simple mixed-signal circuit instead of a TI MSP430 MCU. Experimental results verify the functionality of the circuit. The power consumption of the controller circuit is 16 percent of that of the MCU.

This chapter is organized as follows. Chapter 5.1 presents design of a non-inverting buck-boost converter and the mixed-signal circuit to realize MPPT. Simulation results and experimental results are given in Chapter 5.2 and 5.3, respectively.

5.1 Circuit Design

Figure 5.1 shows a block diagram of the proposed system.

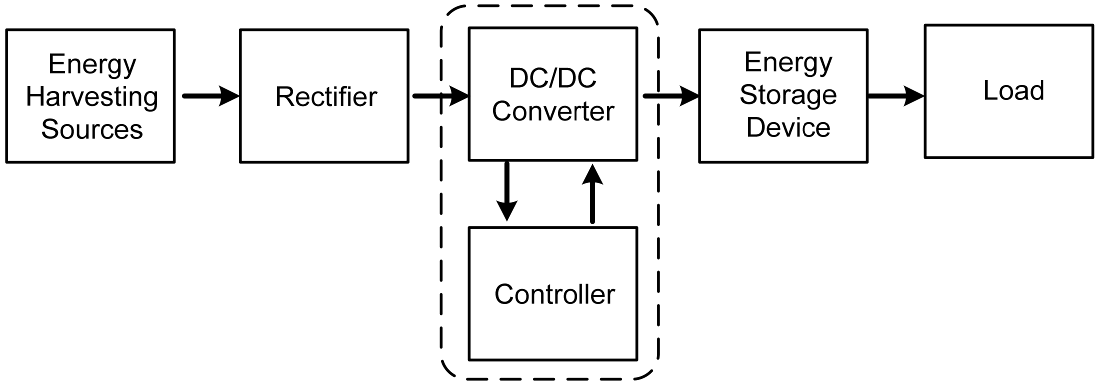

Figure 5.1 The system block diagram.

The power management circuit in the dashed frame consists of a DC-DC converter and a controller. The converter receives a rectified DC voltage from the energy harvesting source. The output of the DC-DC converter is connected to a storage device, which is a supercapacitor or battery. The controller monitors the output power and dynamically adjusts the duty cycle of the DC-DC converter to maximize the power output.

5.1.1 Non-inverting Buck-boost Converter

As discussed in the previous chapters, a DC-DC converter should be able to accommodate a wide range of the input voltage and match the impedance to maximize the power transfer. The buck-boost converter running in DCM is inherently a lossless resistor, and therefore can be used to match the source impedance of the energy harvester. A non-inverting buck-boost converter [66],[67] shown in Figure 5.2 is chosen to avoid the use of transformer, which is a popular choice for integrated circuit design.

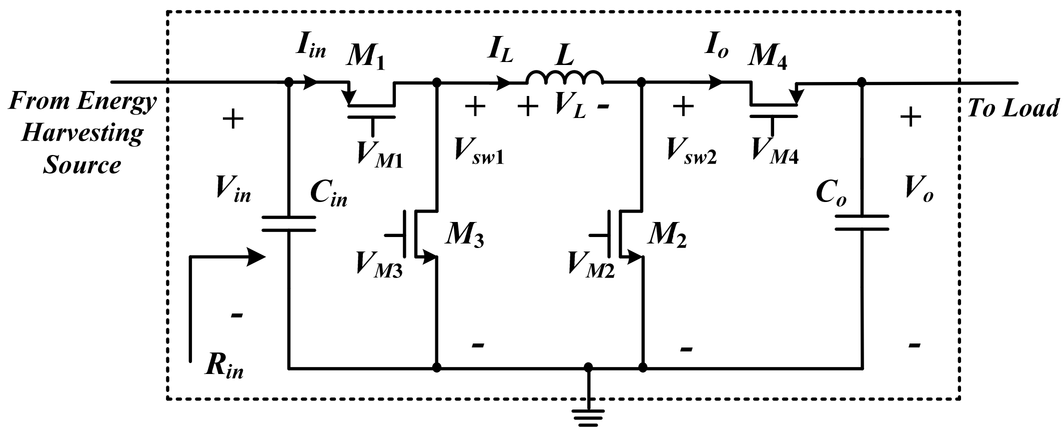

Figure 5.2 Non-inverting buck-boost converter used for integrated resistive impedance matching circuit.

The four-switch non-inverting buck-boost can operate in three different modes: buck, boost and buck-boost converters [67]. Here it is designed to operate as a buck-boost converter. The voltage and current waveforms of the converter for one switching cycle is depicted in Figure 5.3.

Switch M_1 and M_2 conduct during "on-time", while the inductor current is charged up. During "off-time", switch M_3 and M_4 are turned on, which provides a free-wheeling path for the inductor current to charge output capacitor C_o. When the inductor current drops to zero, all switches are turned off. Like a traditional buck-boost converter, the equivalent input resistance can be obtained by the same equation as in (3.18), which is not a function of the input voltage nor output voltage. Since the synchronous rectifiers substitute diodes, an extra circuit is needed to turn switch M_3 and M_4 on and off. The switching node voltage V_{sw1} is used to detect the zero-crossing current to control M_3 and M_4. As shown in Figure 5.3, when M_1 and M_2 are conducting, V_{sw1} is positive. Once M_1 and M_2 are turned off, the inductor current free-wheels through the body diodes of M_3 and M_4. V_{sw1} changes from positive to negative. The zero-crossing detection circuit detects this instance and turns on M_3 and M_4 immediately. When the inductor current drops to zero and changes the direction, V_{sw1} will become positive again. In order to realize the DCM operation, the zero-crossing detection circuit detects this instance and turns off M_3 and M_4 immediately.

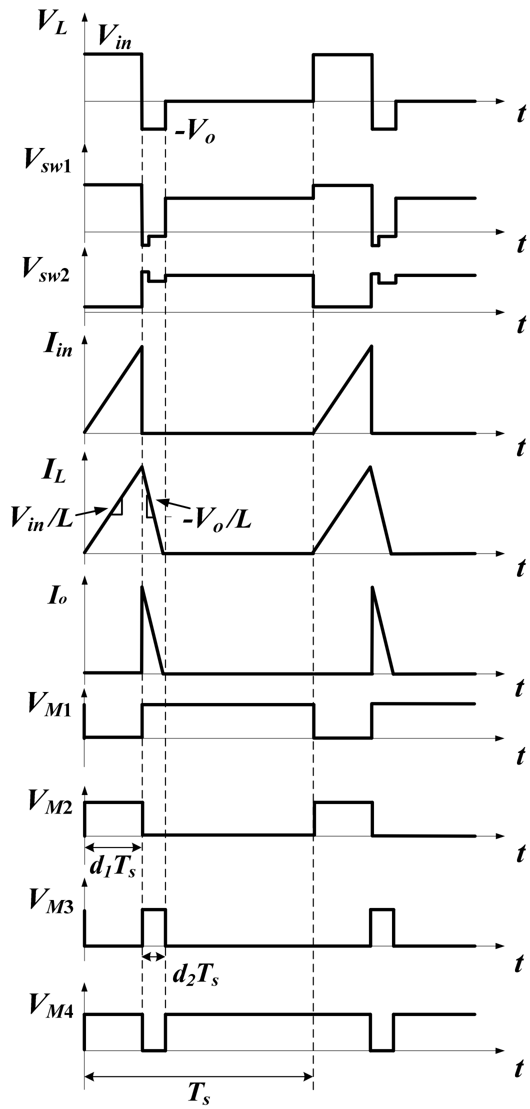

Figure 5.3 Waveforms during one switching period of the buck-boost converter.

The zero-crossing detection (ZCD) circuit is shown in Figure 5.4. When all four switches are turned off, the inductor and the output capacitance of four switches form a resonant circuit. V_{sw1} may swing back to a negative value again. To prevent false triggering of M_3 and M_4, the zero-current detecting circuit is a comparator with hysteresis by adding internal positive feedback [68]. To prevent false triggering of M_3 and M_4 during on-time, the switching of M_3 and M_4 is disabled during on-time by adding the NAND gate with one input connected to V_{M1}. The input and output characteristics of the ZCD circuit is shown in Figure 5.5.

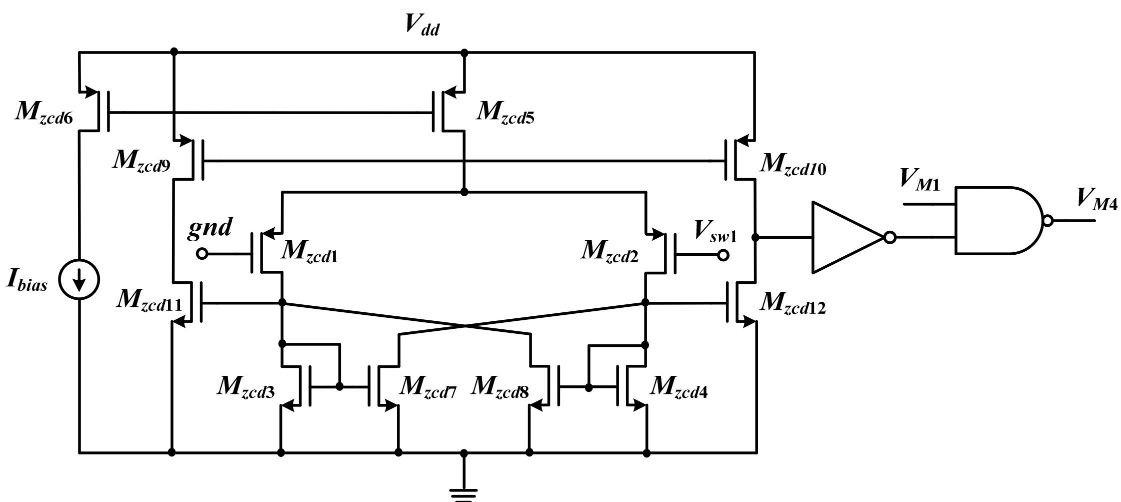

Figure 5.4 The zero-crossing detection (ZCD) circuit.

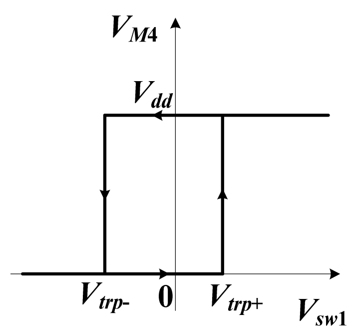

Figure 5.5 Input and output characteristics of the ZCD circuit.

According to [68], the threshold of the ZCD circuit can be designed by sizing M_{zcd3}, M_{zcd7}, M_{zcd4} and M_{zcd8} properly. When V_{sw1} increases to V_{trp+}, at the transition of M_{zcd4} turning on, the drain-to-source current of M_{zcd1} and M_{zcd2} has the relationship given in (5.1).

$$\begin{cases} i_1 + i_2 = i_5 \\ \dfrac{i_1}{i_2} = \dfrac{i_3}{i_7} = \dfrac{\left(\frac{W}{L}\right)_3}{\left(\frac{W}{L}\right)_7} \end{cases} \tag{5.1}$$

where i_k (k = 1,2, …, 8) is the current of M_{zcdk}; $(W/L)_k$ is the ratio of channel width to length of M_{zcdk}. Then the positive trip point voltage is

$$V_{trp+} = V_{GS2} - V_{GS1} = \left(V_{TH2} + \sqrt{\frac{2i_2}{\mu_p C_{ox}\left(\frac{W}{L}\right)_2}} \right) - \left(V_{TH1} + \sqrt{\frac{2i_1}{\mu_p C_{ox}\left(\frac{W}{L}\right)_1}} \right) \tag{5.2}$$

where V_{TH1} and V_{TH2} are the threshold voltage of M_{zcd1} and M_{zcd2}, μ_p is the carrier effective mobility, C_{ox} is the gate oxide capacitance per unit area. Substituting (5.1) into (5.2) leads to

$$V_{trp+} = \left(V_{TH2} + \sqrt{\frac{2i_5 \dfrac{\left(\frac{W}{L}\right)_7}{\left(\frac{W}{L}\right)_3 + \left(\frac{W}{L}\right)_7}}{\mu_p C_{ox}\left(\frac{W}{L}\right)_2}} \right) - \left(V_{TH1} + \sqrt{\frac{2i_5 \dfrac{\left(\frac{W}{L}\right)_3}{\left(\frac{W}{L}\right)_3 + \left(\frac{W}{L}\right)_7}}{\mu_p C_{ox}\left(\frac{W}{L}\right)_1}} \right) \tag{5.3}$$

Similarly, when V_{sw1} decreases to V_{trp-}, at the transition of M_{zcd3} turning on, the current of M_{zcd1} and M_{zcd2} has the relationship given in (5.4).

$$\begin{cases} i_1 + i_2 = i_5 \\ \dfrac{i_1}{i_2} = \dfrac{i_3}{i_7} = \dfrac{\left(\frac{W}{L}\right)_4}{\left(\frac{W}{L}\right)_8} \end{cases} \tag{5.4}$$

The negative trip point voltage is therefore

$$V_{trp-} = V_{GS2} - V_{GS1} = \left(V_{TH2} + \sqrt{\frac{2i_5 \frac{\left(\frac{W}{L}\right)_8}{\left(\frac{W}{L}\right)_4 + \left(\frac{W}{L}\right)_8}}{\mu_p C_{ox} \left(\frac{W}{L}\right)_2}} \right) - \left(V_{TH1} + \sqrt{\frac{2i_5 \frac{\left(\frac{W}{L}\right)_4}{\left(\frac{W}{L}\right)_4 + \left(\frac{W}{L}\right)_8}}{\mu_p C_{ox} \left(\frac{W}{L}\right)_1}} \right) \tag{5.5}$$

5.1.2 Controller

The control circuit needs to search for the optimal duty cycle where the average output power reaches the maximum. The hill-climbing algorithm can be used to achieve MPPT. In order to find out the maximum power point, the power harvested by the buck-boost converter needs to be measured. For small scale energy harvesting, the net change of the output voltage on the supercapacitor or battery during each switching period is small and therefore the power sensing can be simplified by just sensing the average output current. The proposed average output current sensing circuit is shown in Figure 5.6.

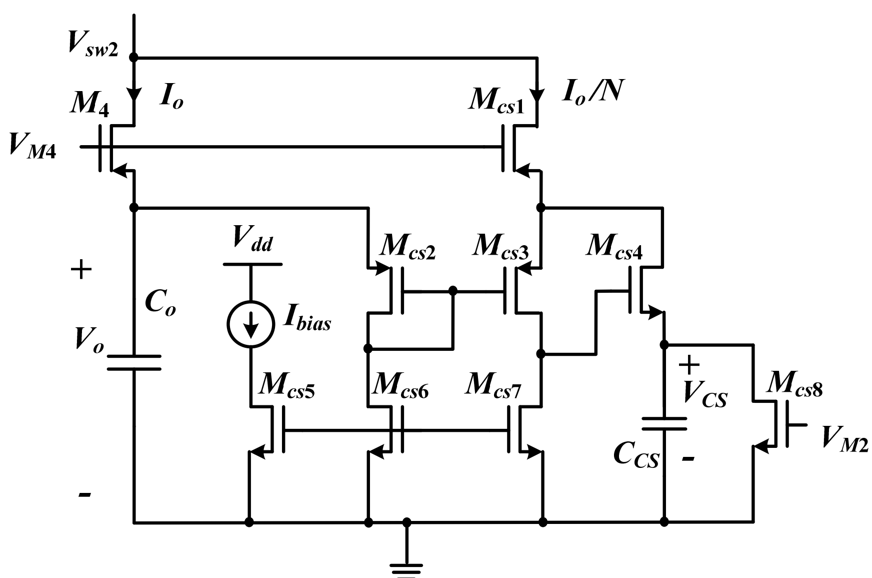

Figure 5.6 The average current sensing circuit.

To measure the average output current during each switching cycle, the voltage on sensing capacitor C_{CS} is reset during "on-time" through the bypass transistor M_{cs8}. The current through main power switch M_4 during "off-time" is mirrored to M_{cs1} and scaled down by a factor of $N = (W/L)_{M4}/(W/L)_{Mcs1}$[69],**Error! Reference source not found.**. In order to maintain the source voltage of M_4 and M_{cs1} to be the same, a small biasing current I_{bias} is mirrored to M_{cs6}, M_{cs7}, and hence M_{cs2} and M_{cs3}. Then the equal current in M_{cs2} and M_{cs3} force the source voltage of M_4 and M_{cs1} to be equal. Most of the current in M_{cs1} goes through M_{cs4} and charge C_{CS}. The voltage on capacitor C_{CS} is therefore obtained as (5.6), which is proportional to the average output current I_o.

$$V_{CS} = C_{CS} \int_o^{T_S} i_o(t)dt = C_{CS} T_S I_{o,avg} \tag{5.6}$$

The initial duty cycle is perturbed with a small increase/decrease. For each switching cycle, the average output current is sensed as an indicator of the average harvested power and compared with the one in previous switching cycle. If it increased, the duty cycle keeps increasing/decreasing; otherwise the duty cycle is decreased/increased. The hill-climbing process continues. Finally, the duty cycle will hover around the optimal operation point. The MPPT circuit is implemented as shown in Figure 5.7, based on the decision generation circuit in [71]. In each comparison cycle, the sensed average current information V_{CS} is stored on a capacitor (C_{p1} or C_{p2}) and compared with the previous value stored on another capacitor (C_{p2} or C_{p1}). At the end of each cycle, the decision of how to change the duty cycle is made and stored at the logic output V_{action} to drive a current source to increase/decrease the voltage V_C on the capacitor C_C. The control voltage V_C compares with the internal ramp to generate the PWM signal, hence the value of V_C determines the duty cycle. As a result of MPPT, the circuit operates at the optimal operating point which leads to the maximum average output current as well as output power.

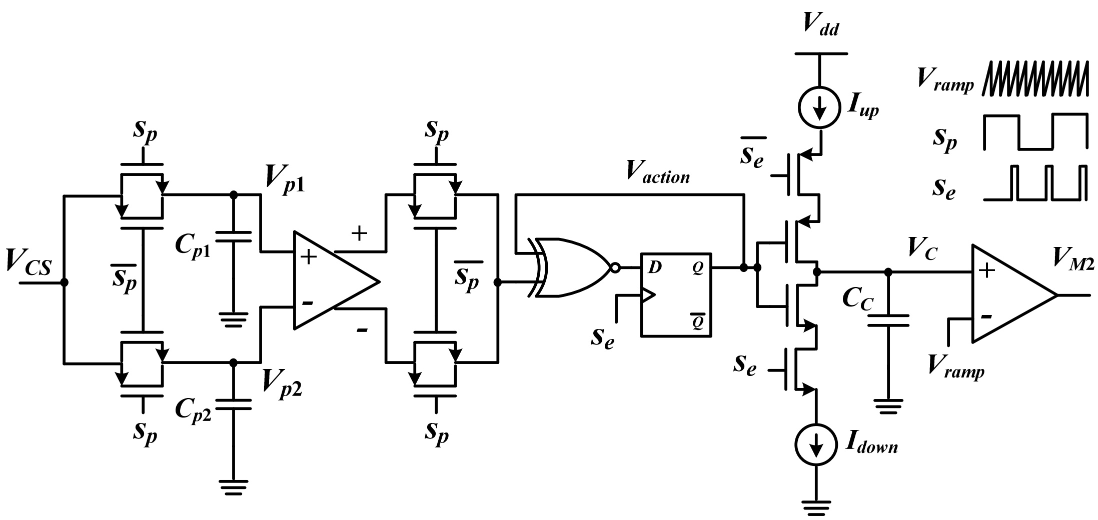

Figure 5.7 The MPPT circuit [71].

5.2 Simulation Results

The proposed power management circuit is developed in a 0.18-μm CMOS process. Figure 5.8 shows the input and output signals of the ZCD circuit. The V_{trp+} and V_{trp-} are 6.3 mV and -362.5 mV respectively. The steady state voltage and current waveforms of the buck-boost converter are shown in Figure 5.9. The ZCD circuit successfully detects the instance when body diodes conduct and turns on M_3 and M_4. When V_{sw1} changes from negative value to positive, the ZCD circuit turns off M_3 and M_4. The oscillation on V_{sw1} after that never causes false triggering of V_{M3} and V_{M4}.

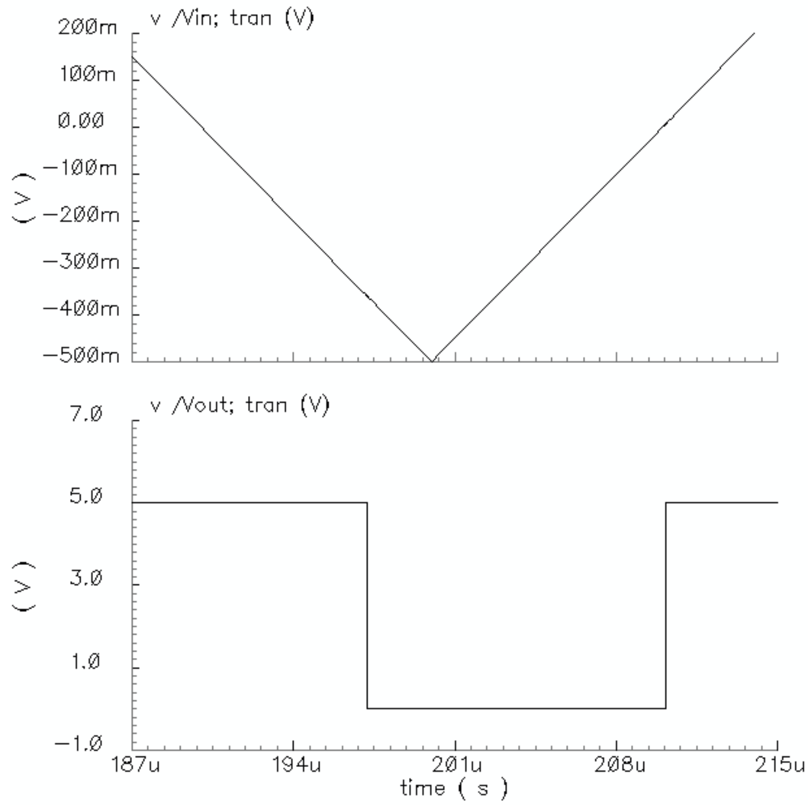

Figure 5.8 The input and output signals of the ZCD circuit.

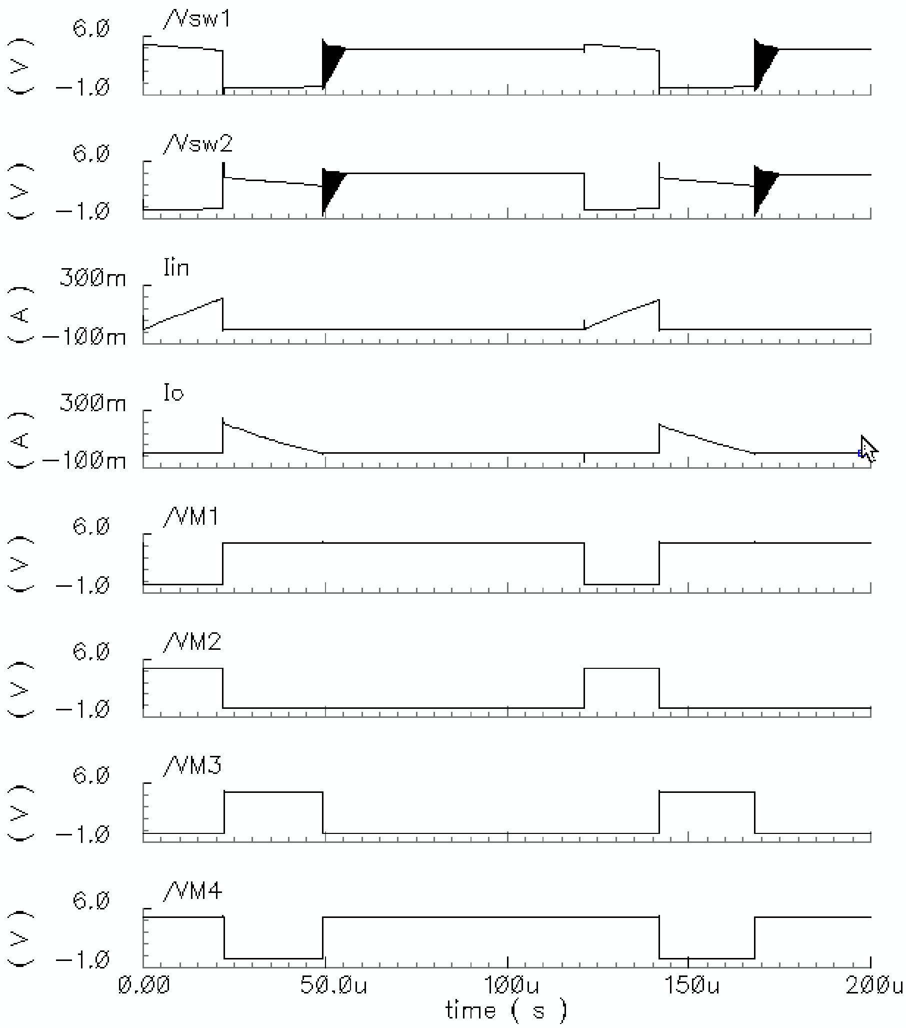

Figure 5.9 The steady state voltage and current waveforms of the buck-boost converter in simulation.

The performance of the average current sensing circuit is shown in Figure 5.10. The output current I_o is designed to be scaled down by a factor of 100 in the sensing circuit. The simulation result closely matches the designed factor. Voltage V_{CS} on sensing capacitor C_{CS} is the integration of sensing current during off-time and it is reset during on-time as designed.

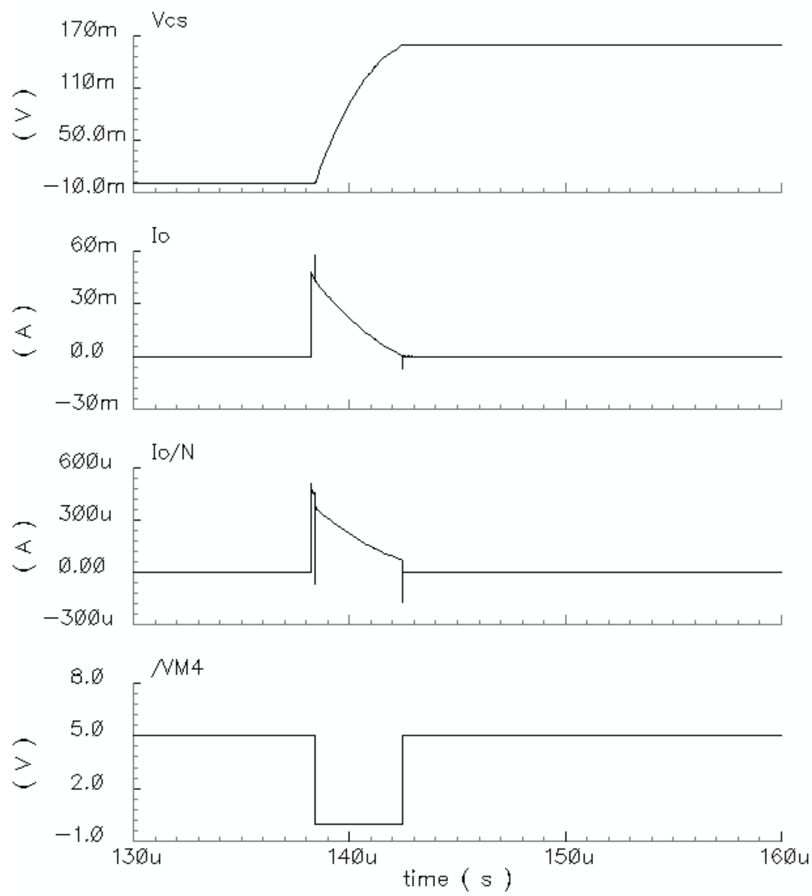

Figure 5.10 The waveforms in the average current sensing circuit.

5.3 Experimental Results

The IC layout is shown in Figure 5.11. Some pads are used for test purpose and the area of the core circuit is only 630 μm x 420 μm. Figure 5.12 is the test board.

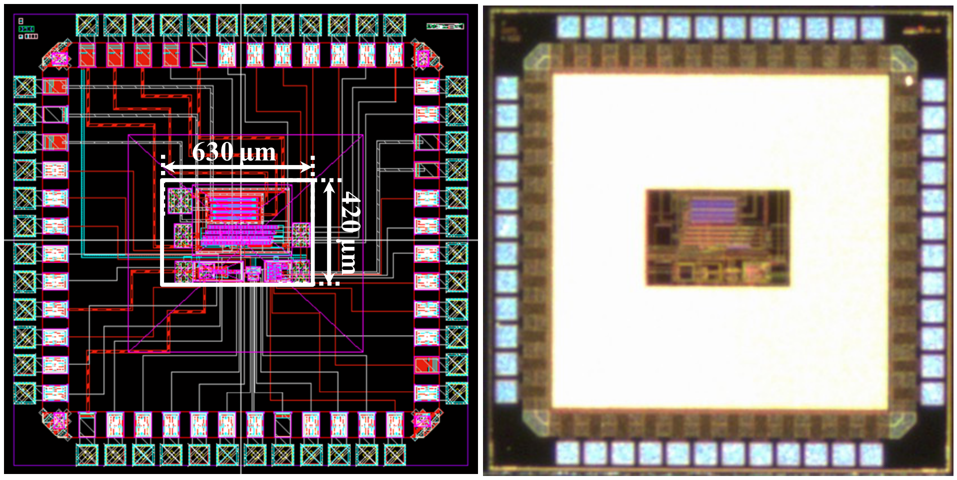

(a) (b)

Figure 5.11 The IC layout: (a) Design; (b) Die photo.

Figure 5.12 The test board.

The steady state gate driving signals and switching node voltage are recorded and shown in Figure 5.13. When V_{M2} goes from logic high to low, V_{sw1} changes from positive to negative because the body diode of M_3 and M_4 start to conduct. Then V_{M3} goes high to turn on M_3. V_{M4} is complementary of V_{M3}, which is not shown in this figure due to the limited number of input channels to the oscilloscope. When inductor current becomes negative, V_{sw1} changes from negative to positive. V_{M3} goes low to turn off M_3. Therefore, the DCM operation of the buck-boost converter is realized with synchronous rectifiers, which verifies the operation of the ZCD circuit.

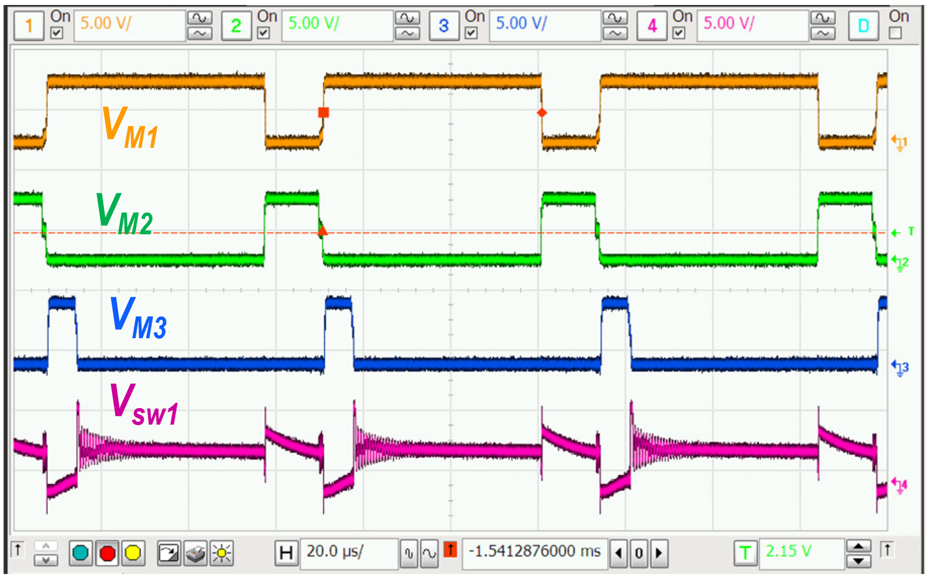

Figure 5.13 Measured steady state waveforms.

The open-loop and closed-loop waveforms of MPPT circuit are shown in Figure 5.14 and Figure 5.15, respectively. In Figure 5.14, the input signal V_{CS} to the MPPT is a triangle waveform from a function generator. As V_{CS} increases, V_{action} signal keeps at logic high, which means the searching direction for the hill-climbing algorithm doesn't change since the V_{CS} is increasing. As V_{CS} decreases, V_{action} signal bounces, which means the MPPT circuit detects the decrease of V_{CS} and tries to change searching direction all the time as designed. Therefore, the operation of the MPPT circuit is verified.

In Figure 5.15, V_{CS} is the voltage across current sensing capacitor C_{CS}. Therefore, a closed-loop is formed. After MPPT circuit is enabled, V_C voltage changes from preset 3.2 V to 2.4 V in 5 ms. The measured power output at different V_C values is listed in Table 5.1. From Table 5.1, the power output peaks when V_C is 2.3V~2.4V. Therefore, the closed-loop controller finds the optimum value where the output power is maximum, which verifies the operation of the current sensing circuit. The current of whole control circuit is measured as 0.41 mA with 3-V power supply, which is one sixth of the current of MCU circuit reported in Chapter 4.

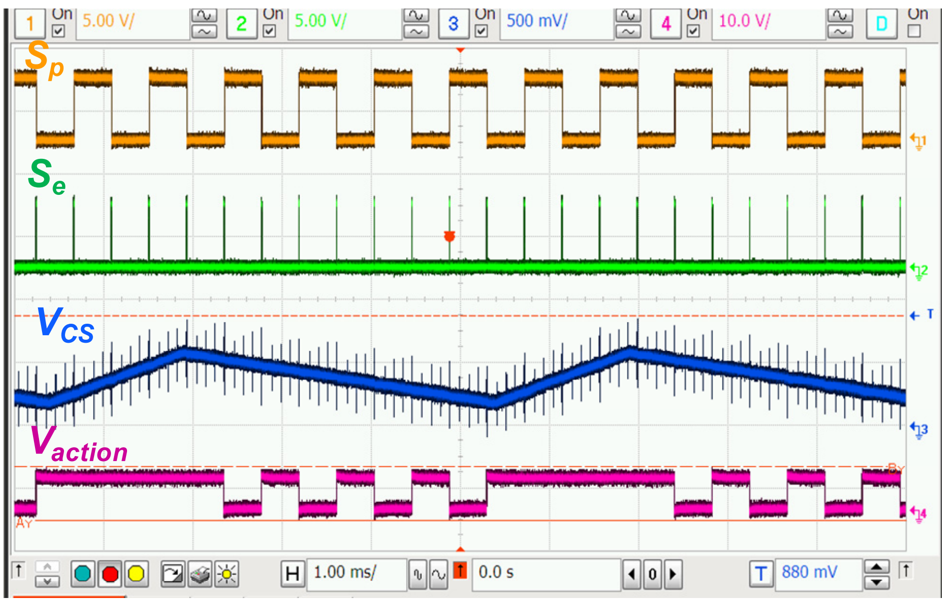

Figure 5.14 Measured waveforms of MPPT circuit at open-loop condition.

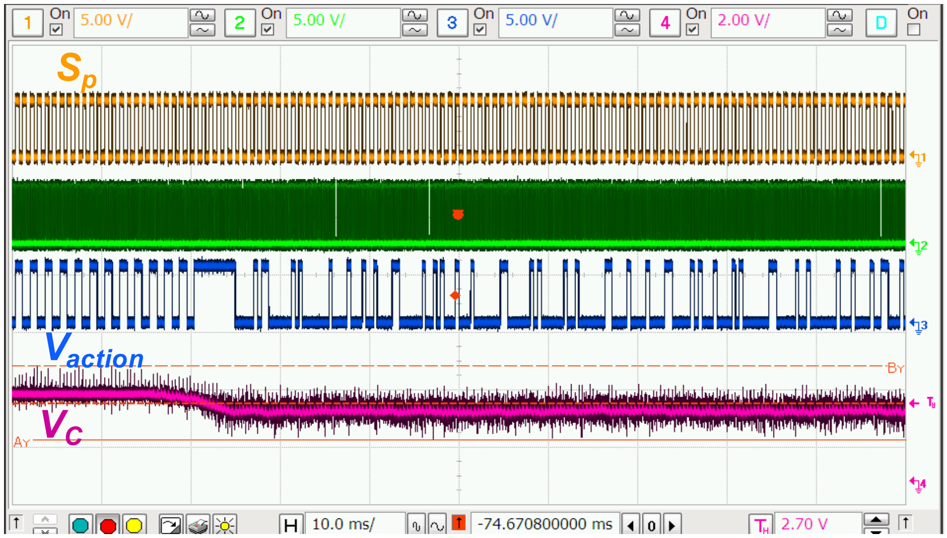

Figure 5.15 Measured waveforms of MPPT circuit at closed-loop condition.

Table 5.1 Measured power output at different V_C values.

V_C (V)	2.1	2.2	2.3	2.4	2.5	2.6	2.7	2.8	2.9	3.0	3.1	3.2
P_O (μW)	482	807	1187	1187	1030	700	666	612	545	493	458	400

5.4 Summary

A power management IC for energy harvesting is designed and implemented in this chapter. The power stage is a non-inverting buck-boost converter running in DCM mode to emulate resistive impedance for maximum power extraction. Synchronous rectifiers are used instead of diodes to reduce the conduction loss. A mixed-signal control circuit is adopted to replace the complicate and power consuming MCU. The design is fabricated in 0.18-μm CMOS process. Simulation and experimental results of the circuit verify the DCM operation of the power stage and the function of MPPT circuit. The power consumption of the controller is reduced to 1.23 mW, which is 16 percent of the power the MCU needs to implement the same MPPT function.

The efficiency of the whole power management circuit is low, around 30 percent for current version of the circuit. It is mainly due to the high channel resistance of power switches. The efficiency can be improved by increasing the size of power MOSFETs and gating the control circuit when not in use. A start-up circuit should also be considered for future version of the circuit.

Chapter 6:
Conclusions

6.1 Summary

Wide deployment of wireless sensor nodes requires new technology for power source. Advances in low power sensors and electronics design along with the low duty cycle operation of wireless sensors have reduced power requirements to sub-microwatt. Such low power dissipation opens up the possibility of powering the WSNs by harvested energy from the environment, eliminating the need for repeated maintenance for batteries. Harvesting kinetic energy using piezoelectric transducers has attracted great attention because of the relatively high power density.

In order to enable system level analysis and evaluation of the energy harvesting system, the equivalent circuit model of piezoelectric generator is studied in Chapter 3. We propose to view the circuit design problem from impedance matching perspective. By applying Norton or Thévenin theorem to the equivalent circuit model of piezoelectric cantilevers, we are able to easily calculate the maximum power output for conjugate impedance matching and resistive impedance matching and find out the optimal load. Simulation results show that resistive matching could be an acceptable compromise for conditioning circuit design when the vibration frequency is around the resonance frequency band of the piezoelectric power generator. A two-stage conditioning circuit with a rectifier and a buck-boost converter is proposed to achieve the resistive impedance matching. Experimental results for open-loop operation are presented to validate the effectiveness of the resistive impedance matching circuit.

Previous approaches for the power management circuit design for piezoelectric energy harvesting either use external power supply to power the controller circuit for DC-DC converter or adopt open-loop operation to save power consumption. Self-powered circuit with dynamic control has not been developed. In Chapter 4, we present a MCU based self-powered closed-loop energy harvesting system. Several schemes to reduce power dissipation of the system are proposed. The DCM operation of flyback converter is chosen as for MPPT to be implemented with a single current sensor. The constant on-time modulation lowers the clock frequency of the controller by more than an order of magnitude, which reduces dynamic power dissipation of the controller. MPPT implemented in the MCU, is executed at intermittent time intervals. When MPPT is not active, the MCU operates at a lower clock frequency to save power. A low power oscillator is adopted for our system to address the start-up problem which has not been considered in the open literature for other self-powered systems. Experimental results indicate that the proposed system harvests up to 8.4 mW of power under 0.5 g base acceleration using four parallel piezoelectric cantilevers and achieves 72 percent efficiency around the resonant frequency of 47 Hz. The sources of the power loss are analyzed to improve the power efficiency, and a breakdown of measured power loss is presented. The diode and the controller (specifically the MCU) are the two major sources for the power loss and account for 63 percent of the total power loss of the system.

In order to further improve the power efficiency, a power management IC for energy harvesting is implemented and presented in Chapter 5. The power stage is a non-inverting buck-boost converter running in DCM mode to emulate resistive impedance for maximum power extraction. The diodes are replaced by synchronous rectifiers to reduce the conduction loss. Instead of the use of a general-purpose MCU, a mixed-signal control circuit is tailored to realize the MPPT function. The design is fabricated in 0.18-μm CMOS process. Simulation and experimental results of the circuit verify the DCM operation of the power stage and function of the MPPT circuit. The power consumption of the controller when it is active is reduced to 1.23 mW, which is 16 percent of the power the MCU needs to implement the same MPPT function.

The circuit topology and the proposed low-power design schemes can be applied to other energy harvesting systems such as small scale wind turbines and solar panels in a straightforward manner.

6.2 Future Works

The average power consumption of the controller can be further reduced by allowing a low duty cycle operation of the control circuit when the environmental conditions change slowly. Operating the controller circuit in subthreshold region is also a possible technique to lower down the power consumption if high MPPT tracking speed is not required.

In the practical application of energy harvesting technique, it is hard for a single ambient energy source to suffice the requirement of wireless sensor nodes since the available energy varies when the environmental condition changes. A possible solution to mitigate variations of available energy is to harvest energy from multiple ambient energy sources. It will bring in new challenges to the circuit design. We need to extend the circuit operating range to accommodate multiple energy sources and optimize the circuit design from system level.

This research has pursued resistive impedance matching, which is an acceptable compromise, provided that the resonance frequency band of the harvester is tuned to the base excitation frequency. For broadband vibration energy harvesting, using synthetic inductance to realize conjugate matching is more promising. The challenge will be low-power design for the active circuit to emulate large inductance.

Appendix A – Publications

N. Kong, D. S. Ha, A. Erturk, and D. J. Inman, "Resistive impedance matching circuit for piezoelectric energy harvesting," *Journal of Intelligent Material Systems and Structures*, vol. 21, no. 13, pp. 1293-1302, September 2010.

N. Kong, T. Cochran, D. S. Ha, H. C. Lin and D. J. Inman, "A self-powered power management circuit for energy harvested by a piezoelectric cantilever," in *Proceedings of IEEE Applied Power Electronics Conference and Exposition (APEC)*, pp. 2154-2160, Feb 2010, Palm Springs, CA, USA.

D. Zhou, N. Kong, D. S. Ha, and D. J. Inman, "A Self-powered Wireless Sensor Node for Structural Health Monitoring," *SPIE International Symposium on Smart Structures and Materials & Nondestructive Evaluation and Health Monitoring*, vol. 7650, 765010 (12 pages), March 2010.

P. Gambier, S. R. Anton, N. Kong, A. Erturk and D. J. Inman, "Combined Piezoelectric, Solar and Thermal Energy Harvesting for Multifunctional Structures with Thin-film Batteries," in *Proceedings of the 21st International Conference on Adaptive Structures and Technologies*, October 2010, State College, PA, USA.

N. Kong, A. Davoudi, M. Hagen, E. Oettinger, M. Xu, D. S. Ha and F. C. Lee, "Automated system identification of digitally-controlled multiphase DC-DC converters," in *Proceedings of IEEE Applied Power Electronics Conference and Exhibition (APEC)*, pp. 259-263, Feb 2009, Washington DC, USA.

A. Davoudi, N. Kong, M. Hagen, M. Muegel and P. Chapman, "Automated tuning of nonlinear digital controllers in multi-phase DC-DC converters," in *Proceedings of IEEE Applied Power Electronics Conference and Exhibition (APEC)*, pp. 626-630, Feb 2009, Washington DC, USA.

S. R. Anton, A. Erturk, N. Kong, D. S. Ha and D. J. Inman, "Self-charging structures using piezoceramics and thin-film batteries," in *Proceedings of the ASME Conference on Smart Materials, Adaptive Structures and Intelligent Systems*, September 21-23, 2009, SMASIS2009-1368, Oxnard, CA, USA. (Best paper prize)

N. Kong, D. S. Ha, J. Li and F. C. Lee, "Off-time prediction in digital constant on-time modulation for DC-DC converters", in *Proceedings of IEEE International Symposium on Circuits and Systems (ISCAS)*, pp. 3270 – 3273, May 2008, Seattle, WA, USA.

Appendix B – Copyright Permission Letter

May 9, 2011

To whom it may concern,

I am a PhD student of Bradley Department of Electrical and Computer Engineering, Virginia Tech. I am preparing my PhD dissertation entitled "Low-power Power Management Circuit Design for Small Scale Energy Harvesting Using Piezoelectric Cantilevers".

I would appreciate permission to reproduce the following item(s) in both print and electronic editions of the dissertation, any derivative products and in publisher authorized distribution by third party distributors, aggregators and other licensees such as abstracting and indexing services. I should be grateful for nonexclusive perpetual world rights in all languages and media. Unless you indicate otherwise, I will use the complete reference given below as the credit line.

In case you do not control these rights, I would appreciate it if you could let me know to whom I should apply for permissions.

1. Figure 5, "Energy flow in piezoelectric energy harvesting systems," Junrui Liang and Wei-Hsin Liao, Smart Materials and Structures 20 (2011) 015005 (11pp).
2. Figure 3, "An improved analysis of the SSHI interface in piezoelectric energy harvesting," Y. C. Shu, I. C. Lien, and W. J. Wu, Smart Materials and Structures 16 (2007) 2253–2264.
3. Figure 6, "Revisit of series-SSHI with comparisons to other interfacing circuits in piezoelectric energy harvesting," I. C. Lien, Y. C. Shu, W. J. Wu, S. M. Shiu and H. C. Lin, Smart Materials and Structures 19 (2010) 125009 (12pp).

For your information, Institute of Physics Publishing is a not-for-profit subsidiary of the UK Institute of Physics and is a signatory to the STM guidelines on use and republication of figures/tables in science publishing.

For your convenience a copy of this letter may serve as a release form; the duplicate copy may be retained for your files.

Thank you for your prompt attention to this request.

Yours sincerely,

Na Kong

PERMISSION TO REPRODUCE AS REQUESTED IS GIVEN PROVIDED THAT:

(a) the consent of the author(s) is obtained
(b) the source of the material including author, title of article, title of journal, volume number, issue number (if relevant), page range (or first page if this is the only information available), date and publisher is acknowledged.
(c) for material being published electronically, a link back to the original article should be provided (via DOI).

IOP Publishing Ltd
Dirac House
Temple Back
BRISTOL
BS1 6BE

10/5/2011
Date

Rights & Permissions

Bibliography

[1] N. S. Hudak and G. G. Amatucci, "Small-scale energy harvesting through thermoelectric, vibration, and radiofrequency power conversion," *Journal of Applied Physics,* vol. 103, pp. 101301-1, 2008.

[2] C. O. Mathuna, T. O'Donnell, R. V. Martinez-Catala, J. Rohan, and B. O'Flynn, "Energy scavenging for long-term deployable wireless sensor networks," *Talanta,* vol. 75, pp. 613-623, 2008.

[3] J. A. Paradiso and T. Starner, "Energy scavenging for mobile and wireless electronics," *IEEE Pervasive Computing*, vol. 4, pp. 18-27, 2005.

[4] http://www.ti.com/lit/pdf/slau227.

[5] R. J. M. Vullers, R. V. Schaijk, H. J. Visser, J. Penders, and C. V. Hoof, "Energy harvesting for autonomous wireless sensor networks," *IEEE Solid-State Circuits Magazine,* vol. 2, pp. 29-38, 2010.

[6] P. Singh, S. Kaneria, V. S. Anugonda, H. M. Chen, X. Q. Wang, D. E. Reisner, and R. M. LaFollette, "Prototype silicon micropower supply for sensors," *IEEE Sensors Journal*, vol. 6, pp. 211-22, 2006.

[7] C. Alippi and C. Galperti, "An adaptive system for optimal solar energy harvesting in wireless sensor network nodes," *IEEE Transactions on Circuits and Systems I: Regular Papers*, vol. 55, pp. 1742-50, 2008.

[8] Y. K. Tan and S. K. Panda, "Optimized wind energy harvesting system using resistance emulator and active rectifier for wireless sensor nodes," *IEEE Transactions on Power Electronics,* vol. 26, pp. 38-50, 2011.

[9] S. Dwari and L. Parsa, "An efficient AC-DC step-up converter for low-voltage energy harvesting," *IEEE Transactions on Power Electronics,* vol. 25, pp. 2188-2199, 2010.

[10] S. P. Beeby, R. N. Torah, M. J. Tudor, P. Glynne-Jones, T. O'Donnell, C. R. Saha, and S. Roy, "A micro electromagnetic generator for vibration energy harvesting," *Journal of Micromechanics and Microengineering,* vol. 17, pp. 1257-1265, 2007.

[11] S. Roundy and P. K. Wright, "A piezoelectric vibration based generator for wireless electronics," *Smart Materials and Structures,* vol. 13, pp. 1131-1142, 2004.

[12] M. Lallart and D. J. Inman, "Low-cost integrable tuning-free converter for piezoelectric energy harvesting optimization," *IEEE Transactions on Power Electronics,* vol. 25, pp. 1811-19, 2010.

[13] D. Guyomar, G. Sebald, S. Pruvost, M. Lallart, A. Khodayari, and C. Richard, "Energy harvesting from ambient vibrations and heat," *Journal of Intelligent Material Systems and Structures,* vol. 20, pp. 609-24, 2009.

[14] H. Lhermet, C. Condemine, M. Plissonnier, R. Salot, P. Audebert, and M. Rosset, "Efficient power management circuit: from thermal energy harvesting to above-IC microbattery energy storage," *IEEE Journal of Solid-State Circuits,* vol. 43, pp. 246-55, 2008.

[15] J. A. Hagerty, N. D. Lopez, B. Popovic, and Z. Popovic, "Broadband Rectenna Arrays for Randomly Polarized Incident Waves," in *30th European Microwave Conference*, pp. 1-4, 2000.

[16] T. Paing, J. Shin, R. Zane, and Z. Popovic, "Resistor emulation approach to low-power RF energy harvesting," *IEEE Transactions on Power Electronics,* vol. 23, pp. 1494-501, 2008.

[17] S. Roundy, P. K. Wright, and J. Rabaey, "A study of low level vibrations as a power source for wireless sensor nodes," *Computer Communications,* vol. 26, pp. 1131-1144, 2003.

[18] S. Roundy, P.K. Wright, and J. Rabaey, *Energy Scavenging for Wireless Sensor Networks with Special Focus on Vibrations*, Kluwer Academic Press, 2003.

[19] S. Roundy, E. S. Leland, J. Baker, E. Carleton, E. Reilly, E. Lai, B. Otis, J. M. Rabaey, P. K. Wright, and V. Sundararajan, "Improving power output for vibration-based energy scavengers," *IEEE Pervasive Computing,* vol. 4, pp. 28-36, 2005.

[20] S. P. Beeby, M. J. Tudor, and N. M. White, "Energy harvesting vibration sources for microsystems applications," *Measurement Science and Technology,* vol. 17, pp. 175-95, 2006.

[21] C. B. Williams and R. B. Yates, "Analysis of a micro-electric generator for microsystems," *Sensors and Actuators, A: Physical*, vol. 52, no. 1-3, pp. 8-11, 1996.

[22] S. R. Anton and H. A. Sodano, "A review of power harvesting using piezoelectric materials (2003-2006)," *Smart Materials and Structures,* vol. 16, pp. R1-R21, 2007.

[23] S. Priya, "Advances in energy harvesting using low profile piezoelectric transducers," *Journal of Electroceramics,* vol. 19, pp. 165-182, 2007.

[24] C. Richard, D. Guyomar, D. Audigier, and G. Ching, "Semi-passive damping using continuous switching of a piezoelectric device," in *Proceedings of the SPIE - The International Society for Optical Engineering*, v 3672, p 104-11, 1998.

[25] D. Guyomar, A. Badel, E. Lefeuvre, and C. Richard, "Toward energy harvesting using active materials and conversion improvement by nonlinear processing," *IEEE Transactions on Ultrasonics, Ferroelectrics and Frequency Control,* vol. 52, pp. 584-595, 2005.

[26] A. Badel, E. Lefeuvre, L. Lebrun, C. Richard, and D. Guyomar, "Single crystals and nonlinear process for outstanding vibration-powered electrical generators," *IEEE Transactions on Ultrasonics, Ferroelectrics and Frequency Control,* vol. 53, pp. 673-684, 2006.

[27] S. Xu, K. D. T. Ngo, T. Nishida, G.-B. Chung, and A. Sharma, "Low frequency pulsed resonant converter for energy harvesting," *IEEE Transactions on Power Electronics,* vol. 22, pp. 63-68, 2007.

[28] M. Lallart and D. Guyomar, "An optimized self-powered switching circuit for non-linear energy harvesting with low voltage output," *Smart Materials and Structures,* vol. 17, 2008.

[29] J. Liang and W.-H. Liao, "An improved self-powered switching interface for piezoelectric energy harvesting," in *Proceedings of IEEE International Conference on Information and Automation,* p 945-950, 2009.

[30] Y. K. Ramadass and A. P. Chandrakasan, "An efficient piezoelectric energy harvesting interface circuit using a bias-flip rectifier and shared inductor," *IEEE Journal of Solid-State Circuits,* vol. 45, pp. 189-204, 2010.

[31] G. K. Ottman, H. F. Hofmann, A. C. Bhatt, and G. A. Lesieutre, "Adaptive piezoelectric energy harvesting circuit for wireless remote power supply," *IEEE Transactions on Power Electronics,* vol. 17, pp. 669-676, 2002.

[32] G. K. Ottman, H. F. Hofmann, and G. A. Lesieutre, "Optimized piezoelectric energy harvesting circuit using step-down converter in discontinuous conduction mode," *IEEE Transactions on Power Electronics,* vol. 18, pp. 696-703, 2003.

[33] E. Lefeuvre, D. Audigier, C. Richard, and D. Guyomar, "Buck-boost converter for sensorless power optimization of piezoelectric energy harvester," *IEEE Transactions on Power Electronics,* vol. 22, pp. 2018-25, 2007.

[34] Kasyap, A., Lim, J., Johnson, D., Horowitz, S., Nishida, T., Ngo, K., Sheplak, M. and Cattafesta, L., "Energy reclamation from a vibrating piezoceramic composite beam," in *Proceedings of 9th International Congress on Sound and Vibration*, Paper No. 271, 2002.

[35] N. Kong, D. S. Ha, A. Erturk, and D. J. Inman, "Resistive impedance matching circuit for piezoelectric energy harvesting," *Journal of Intelligent Material Systems and Structures,* vol. 21, pp. 1293-1302, 2010.

[36] A. Tabesh and L. G. Frechette, "A low-power stand-alone adaptive circuit for harvesting energy from a piezoelectric micropower generator," *IEEE Transactions on Industrial Electronics,* vol. 57, pp. 840-9, 2010.

[37] N. Kong, T. Cochran, H. Dong Sam, L. Hung-Chih, and D. J. Inman, "A self-powered power management circuit for energy harvested by a piezoelectric cantilever," in *Proceedings of IEEE Applied Power Electronics Conference and Exposition*, pp. 2154-60, 2010.

[38] D. Kwon and G. A. Rincon-Mora, "A single-inductor AC-DC piezoelectric energy-harvester/battery-charger IC converting (0.35 to 1.2 V) to (2.7 to 4.5 V)," in *IEEE International Solid-State Circuits Conference*, pp. 494-5, 2010.

[39] http://robotics.eecs.berkeley.edu/~pister/SmartDust/

[40] http://en.wikipedia.org/wiki/Sensor_node#cite_note-0

[41] B. Warneke, B. Atwood, and K. S. J. Pister, "Smart dust mote forerunners," in *14th IEEE International Conference on Micro Electro Mechanical Systems*, pp. 357-360, 2001.

[42] D. Zhou, D. S. Ha, and D. J. Inman, "Ultra low-power active wireless sensor for structural health monitoring," *International Journal of Smart Structures and Systems*, vol. 6, no. 5-6, pp. 675-687, 2010.

[43] N. G. Elvin and A. A. Elvin, "A general equivalent circuit model for piezoelectric generators," *Journal of Intelligent Material Systems and Structures,* vol. 20, pp. 3-9, 2009.

[44] A. Erturk and D. J. Inman, "A distributed parameter electromechanical model for cantilevered piezoelectric energy harvesters," *Journal of Vibration and Acoustics, Transactions of the ASME,* vol. 130, 2008.

[45] A. Erturk and D. J. Inman, "An experimentally validated bimorph cantilever model for piezoelectric energy harvesting from base excitations," *Smart Materials and Structures,* p. 025009, 2009.

[46] J. Liang and W.-H. Liao, "Energy flow in piezoelectric energy harvesting systems," *Smart Materials and Structures,* vol. 20, p. 015005, 2011.

[47] Y. C. Shu and I. C. Lien, "Analysis of power output for piezoelectric energy harvesting systems," *Smart Materials and Structures,* vol. 15, pp. 1499-512, 2006.

[48] Y. C. Shu, I. C. Lien, and W. J. Wu, "An improved analysis of the SSHI interface in piezoelectric energy harvesting," *Smart Materials and Structures,* vol. 16, pp. 2253-64, 2007.

[49] P. Rakers, L. Connell, T. Collins, and D. Russell, "Secure contactless smartcard ASIC with DPA protection," *IEEE Journal of Solid-State Circuits,* vol. 36, pp. 559-565, 2001.

[50] J. Colomer-Farrarons, P. Miribel-Catala, A. Saiz-Vela, M. Puig-Vidal, and J. Samitier, "Power-conditioning circuitry for a self-powered system based on micro PZT generators in a 0.13-μm low-voltage low-power technology," *IEEE Transactions on Industrial Electronics,* vol. 55, pp. 3249-3257, 2008.

[51] Y. H. Lam, K. Wing-Hung, and T. Chi-Ying, "Integrated low-loss CMOS active rectifier for wirelessly powered devices," *IEEE Transactions on Circuits and Systems II: Analog and Digital Signal Processing,* vol. 53, pp. 1378-82, 2006.

[52] T. T. Le, J. Han, A. Von Jouanne, K. Mayaram, and T. S. Fiez, "Piezoelectric micro-power generation interface circuits," *IEEE Journal of Solid-State Circuits,* vol. 41, pp. 1411-1419, 2006.

[53] W. Erickson and D. Maksimovic, *Fundamentals of Power Electronics*, Norwell, MA: Kluwer, 2001.

[54] C. Richard, D. Guyomar, D. Audigier, and H. Bassaler, "Enhanced semi-passive damping using continuous switching of a piezoelectric device on an inductor," in *Proceedings of the SPIE - The International Society for Optical Engineering*, v 3989, pp. 288-99, 2000.

[55] A. Badel, D. Guyomar, E. Lefeuvre, and C. Richard, "Efficiency enhancement of a piezoelectric energy harvesting device in pulsed operation by synchronous charge inversion," *Journal of Intelligent Material Systems and Structures,* vol. 16, pp. 889-901, 2005.

[56] E. Lefeuvre, A. Badel, C. Richard, and D. Guyomar, "Piezoelectric energy harvesting device optimization by synchronous electric charge extraction," *Journal of Intelligent Material Systems and Structures,* vol. 16, pp. 865-876, 2005.

[57] M. Lallart, E. Lefeuvre, C. Richard, and D. Guyomar, "Self-powered circuit for broadband, multimodal piezoelectric vibration control," *Sensors and Actuators, A: Physical,* vol. 143, pp. 377-382, 2008.

[58] E. Lefeuvre, A. Badel, C. Richard, L. Petit, and D. Guyomar, "A comparison between several vibration-powered piezoelectric generators for standalone systems," *Sensors and Actuators A (Physical),* vol. 126, pp. 405-16, 2006.

[59] D. Guyomar, G. Sebald, S. Pruvost, M. Lallart, A. Khodayari, and C. Richard, "Energy harvesting from ambient vibrations and heat," *Journal of Intelligent Material Systems and Structures,* vol. 20, pp. 609-24, 2009.

[60] I. C. Lien, Y. C. Shu, W. J. Wu, S. M. Shiu, and H. C. Lin, "Revisit of series-SSHI with comparisons to other interfacing circuits in piezoelectric energy harvesting," *Smart Materials and Structures,* vol. 19, 2010.

[61] H.W. Jackson, *Introduction to Electronic Circuits*, Prentice-Hall, 1959.

[62] D. Zhu, M. J. Tudor, and S. P. Beeby, "Strategies for increasing the operating frequency range of vibration energy harvesters: a review," *Measurement Science and Technology,* vol. 21, p. 022001 (29 pp.), 2010.

[63] J. Li, Y. Qiu, Y. Sun, B. Huang, M. Xu, D. S. Ha, F. C. Lee, "High resolution digital duty cycle modulation schemes for voltage regulators," in *Proceedings of IEEE Applied Power Electronics Conference and Exposition*, pp.871-876, 2007.

[64] T. Esram and P. L. Chapman, "Comparison of photovoltaic array maximum power point tracking techniques," *IEEE Transactions on Energy Conversion,* vol. 22, pp. 439-449, 2007.

[65] N. Femia, G. Petrone, G. Spagnuolo, and M. Vitelli, "Optimization of perturb and observe maximum power point tracking method," *IEEE Transactions on Power Electronics*, vol. 20, pp. 963-973, 2005.

[66] S. Biranchinath, and G. A. Rincon-Mora, “A low voltage, dynamic, noninverting, synchronous buck-boost converter for portable applications,” *IEEE Transactions on Power Electronics*, vol. 19, no. 2, pp.443-452, 2004.

[67] M. Gaboriault and A. Notman, “A high efficiency, noninverting, buck-boost DC-DC converter,” in *Proceedings of the IEEE Applied Power Electronics Conference and Exposition*, pp. 1411-1415, 2004.

[68] P. E. Allen and D. R. Holberg, *CMOS Analog Circuit Design*, Oxford, NY, Oxford: University Press, 2002.

[69] D. Ma, W. H. Ki, C. Y. Tsui, and P. K. T. Mok, "A 1.8V single-inductor dual-output switching converter for power reduction techniques," in *IEEE Symposium on VLSI Circuits, Digest of Technical Papers*, Kyoto, Japan, pp. 137-140, 2001.

[70] H. Y. H. Lam, W.-H. Ki, and D. Ma, "Loop gain analysis and development of high-speed high-accuracy current sensors for switching converters," in *Proceedings of IEEE International Symposium on Circuits and Systems*, vol. 5, pp. V-828-V-831, 2004.

[71] H. Shao, C.-Y. Tsui, and W.-H. Ki, "The design of a micro power management system for applications using photovoltaic cells with the maximum output power control," *IEEE Transactions on Very Large Scale Integration (VLSI) Systems,* vol. 17, pp. 1138-1142, 2009.